Testing Statistical Isotropy With Large-Scale Structure

by

Cameron M. Gibelyou

A dissertation submitted in partial fulfillment
of the requirements for the degree of
Doctor of Philosophy
(Physics)
in The University of Michigan
2012

Doctoral Committee:

Assistant Professor Dragan Huterer, Chair
Professor Timothy McKay
Associate Professor Aaron Pierce
Assistant Professor Jeff McMahon
Research Scientist Philip Hughes

"And amid all the splendours of the World, its vast halls and spaces, and its wheeling fires, Ilúvatar chose a place for their habitation in the Deeps of Time and in the midst of the innumerable stars. And this habitation might seem a little thing to those who consider only the majesty of the Ainur, and not their terrible sharpness; as who should take a whole field of Arda for the foundation of a pillar and so raise it until the cone of its summit were more bitter than a needle; or who consider only the immeasurable vastness of the World, which still the Ainur are shaping, and not the minute precision to which they shape all things therein."

– J.R.R. Tolkien, *The Silmarillion*

To Nicole, without whom none of this would have happened

ACKNOWLEDGEMENTS

For help with the set of research projects that have gone into my thesis, thanks to Lucas Macri, Tom Jarrett, Dominik Schwarz, Weikang Zheng, Sudeep Das, Michael Hudson, Jim Condon, Chris Hirata, and Jerry Fishman, all of whom were very helpful at different points along the way. Thanks to the members of my committee: Tim McKay, Aaron Pierce, Jeff McMahon, Philip Hughes, and especially Dragan Huterer, who has been an absolutely amazing advisor for the past five years.

This publication makes use of data products from the Two Micron All Sky Survey, which is a joint project of the University of Massachusetts and the Infrared Processing and Analysis Center/California Institute of Technology, funded by the National Aeronautics and Space Administration and the National Science Foundation.

I was supported by grants from the NSF and NASA in the course of this work.

TABLE OF CONTENTS

LIST OF FIGURES

Figure

LIST OF TABLES

Table

LIST OF APPENDICES

Appendix

CHAPTER I

Introduction

Cosmology is the study of the physical universe on its largest scales in space and time. As a physical science that explores, both observationally and theoretically, the properties of the universe at scales much larger than that of individual galaxies, the field is actually quite young; the existence of galaxies outside the Milky Way was only demonstrated conclusively in the 1920s. But ever since then, it has become increasingly clear that the observable universe is unimaginably vast, and includes on the order of a hundred billion galaxies.

In addition to the ordinary luminous matter that we see when we observe the distant universe, the universe appears to contain components that remain comparatively poorly understood. Observations of the rotation curves of galaxies, gravitational lensing by clusters of galaxies, and the growth of structure in the universe all lend a great deal of support to the notion that most of the matter in the universe is non-baryonic "dark matter" which neither emits light nor interacts electromagnetically in any way. Other observations, including the acceleration of the universe and the inference of the universe's total mass-energy budget from the cosmic microwave background, show that an even larger portion of the universe's energy exists in the form of "dark energy," which exerts an antigravity-like influence at the very largest

scales of the universe, pushing distant galaxies apart at ever-increasing rates. While the identity and precise nature of dark-matter particles remains elusive, and no singularly compelling model of dark energy has been advanced, the presence of dark matter and dark energy is inferred from their influences on the baryonic/luminous matter that we can see and observe. In this way, the existence of dark matter and dark energy is well-established even without compelling models to explain precisely what they are.

The proportions of ordinary matter, dark matter, and dark energy are also well-established: roughly 70-75 percent of the universe's mass-energy is in the form of dark energy, 20-25 percent takes the form of dark matter, and 4-5 percent corresponds to baryonic matter. Various independent probes of the relative "abundances" of dark energy, dark matter, and ordinary matter all arrive at nearly the same proportions, an encouraging sign that our understanding of the non-electromagnetic universe is on the right basic track. An array of observations have thus led to the emergence of something like a "standard model" of the universe, the ΛCDM model, which stands for dark energy (Λ indicating Einstein's cosmological constant, a major candidate for the identity of the dark energy) plus cold dark matter, the components that dominate the mass-energy of the universe.

As far as the luminous matter is concerned, our knowledge of the distribution of galaxies and other tracers of the large-scale structure of matter in the universe is constantly growing. Major observational projects such as the Sloan Digital Sky Survey (SDSS) and the upcoming Dark Energy Survey (DES) and Large Synoptic Survey Telescope (LSST) map increasingly wide portions of the sky to increasing depths, giving the astronomical community a better and better map of the universe at its largest scales.

As we look further out into the universe, we peer further back in time, due to the fact that the speed of light is finite and hence light takes billions of years to reach us from the most distant galaxies we can see. Peering even further back in time than the most distant galaxies, we see the most distant (in both space and time) light in the universe: the cosmic microwave background, which we see as coming from the surface of last scattering near the "edge" (not a literal physical edge) of the observable universe. Many observational projects, including the COsmic Background Explorer (COBE), the Wilkinson Microwave Anisotropy Probe (WMAP), and the Planck satellite (which is currently collecting data), have made and are making highly detailed observations of the CMB, and thereby mapping out the structure of the universe at its largest scales at a very early time, roughly 380,000 years after the Big Bang.

At that 380,000-year mark, the first atoms formed, removing free electrons from the universe and thereby setting photons (which we now detect as the CMB) free to travel unimpeded through the universe (instead of scattering off the free electrons, as before the 380,000-year mark). To understand the evolution of the universe before that time, we cannot rely on direct observation of light from the early universe, since the CMB is the oldest light we observe. However, based on the fact that we have observed the universe to be expanding for almost the entirety of the last 13.7 billion years, going back to less than a million years after the Big Bang, we can extrapolate and "predict" that the universe has been expanding for the entirety of its existence. Such an assumption has consequences for the physics of the universe; for example, the entire universe should have been the right temperature for several minutes in the immediate aftermath of the Big Bang to sustain fusion. Well-constrained theoretical predictions for the abundances of isotopes of hydrogen, helium, and lithium

can be made, and observed abundances agree with predictions – an impressive and highly nontrivial match between theory and observation, given that predictions for abundances of different isotopes range over many orders of magnitude. Big Bang nucleosynthesis, along with the observed expansion of the universe and the existence and detailed properties of the cosmic microwave background, are considered the "three pillars" of the Big Bang, the three most important lines of evidence in support of the almost universally accepted model for the evolution of the universe.

A great deal of research effort in the past 30 years has been put toward understanding the very first tiny fraction of a second after the birth of the universe. Cosmological inflation is a paradigm that explains several outstanding problems with the Hot Big Bang model (most notably the flatness problem and the horizon problem) and also has at least one major observational success to its name: inflation, at least in its simplest realizations, predicts a nearly scale-invariant power spectrum, which accords very well with observations in recent years.

Through powerful unifying ideas like inflation, the frontiers of cosmology now regularly involve exploring connections between the very small and the very large, especially in the setting of the early universe where the physics of subatomic particles can have consequences for extremely large scales in the present universe. More generally, cosmology can be seen in part as a testbed for ideas about fundamental physics: constraints derived from observations of the cosmic microwave background and the large-scale structure of the universe (referring primarily to the distribution of matter, both dark and luminous, in the universe) can tell us something about fundamental physics.

One example of this involves the cosmological principle. The cosmological principle, an assumption that cosmologists have built their theoretical models around for

a very long time, holds that on its largest scales (hundreds of Mpc), the universe is both the same from point to point (homogeneity) and the same from one direction to another (isotropy). While the universe is not identically the same from one point or direction to another, even on the largest scales, we speak in terms of statistical averages when articulating the universe's homogeneity and isotropy.

The cosmological principle, which functioned as a simplifying assumption before it had strong theoretical or observational justification, is also a natural prediction of the simplest models of inflation. Observations do bear out that the cosmological principle is a reasonable approximation for most purposes. However, the cosmological principle still exists as a sort of hybrid of assumption, theoretical prediction, and loosely constrained observational result. Few rigorous observational tests have been applied to test homogeneity and isotropy; my thesis attempts to address this. Accordingly, I present work I have done toward performing tests of the statistical isotropy of the universe using large-scale structure. The goal of this work is, fundamentally, to bring statistical isotropy more fully out of the realm of assumption and into the realm of observation.

While I have worked on multiple projects that do not fit neatly under this heading, this thesis will focus only on work strongly connected with these questions of isotropy, in the interest of telling a coherent story rather than haphazardly smashing together largely unrelated work. More specifically, I will discuss work I have done in collaboration with Dragan Huterer on the presence of dipole components in the distribution of various tracers of large-scale structure (galaxies observed in the infrared and radio, as well as gamma-ray bursts) on the sky. This work puts statistical isotropy, and more specific predictions of ΛCDM theory, to the test. Observational results which are used to test theoretical predictions come from an array of cosmological probes

with (typically) quite different sources of systematic error. The control of systematic errors, and the understanding of which systematic errors affect which surveys, is a major theme of this work, and a large portion of the work involved in performing this research involved understanding systematic errors in detail. The other major component of the work involved coding up all the formalism and rigorously checking to make sure that the behavior of the estimator we used to detect dipole signals was as expected.

1.1 Dissertation outline

In Chapter 2 of this thesis, I lay out the theoretical foundations of work on "dipoles in the sky." The usual terminology for describing dipoles present in large-scale structure tends to be somewhat confusing, and so I will attempt to describe as precisely as possible which dipole-related quantities are relevant for this analysis.

In Chapter 3, I outline the formalism used throughout the thesis for detecting dipole patterns in a distribution of objects observed on the celestial sphere. I also demonstrate how this formalism naturally accounts for real or proposed systematic errors.

In Chapter 4, I provide several comparisons of theoretical predictions and observational results for dipole patterns present in Two Micron All Sky Survey (2MASS) extragalactic sources as well as the 2MASS Redshift Survey (2MRS), a survey of redshifts of a small subset of the 2MASS extragalactic sources.

In Chapter 5, I provide similar theory vs. observation comparisons for the Compton Gamma Ray Observatory (CGRO) BATSE catalog, which observed over 1600 gamma-ray bursts, and the NRAO VLA Sky Survey (NVSS) catalog of extragalactic sources observed in radio.

Chapter 6 summarizes the previous four chapters. Appendix A presents detailed tables related to results presented earlier in the thesis. Appendices B and C demonstrate relatively minor but still notable features of the formalism and algorithms I have used to produce these results.

CHAPTER II

Statistical Isotropy and Dipoles in the Sky

In this chapter, I provide a detailed introduction to the theoretical concepts and predictions that are put to the test in this thesis.

2.1 The Importance of Statistical Isotropy

The cosmological principle holds that the universe is homogeneous and isotropic on its largest observable scales. While the cosmological principle is a crucial ingredient in obtaining many important results in quantitative cosmology, there is no fundamental reason why our universe *must* obey it. The most general aim of this research has been to directly test the cosmological principle using data from recent astrophysical observations.

In a time when cosmology has become ever more precise and data-driven, it makes a great deal of sense to put the cosmological principle to the observational test. This has been done already only to a limited extent, and many avenues for testing the cosmological principle remain to be pursued. It is particularly worthwhile to test statistical isotropy, which, in addition to being a consequence of the cosmological principle, is a generic prediction of inflationary models of the early universe. Any observed violations of statistical isotropy could have far-reaching implications for our understanding of the universe's earliest moments, and violations of isotropy would

also invalidate basic assumptions that serve as prerequisites to typical methods of data analysis in observational cosmology.

To define statistical isotropy, consider a fluctuating field on the sky $T(\hat{\mathbf{n}})$ (the same arguments will apply for any field, including the cosmic microwave background (CMB) temperature field, the galaxy density field, etc.). The field is statistically isotropic if the two-point correlation function depends *only* on the separation between points:

$$\langle T(\hat{\mathbf{n}})T(\hat{\mathbf{n}}')\rangle = C(\hat{\mathbf{n}}\cdot\hat{\mathbf{n}}') \tag{2.1}$$

while in the case where statistical isotropy is violated, the right-hand side would read $C(\hat{\mathbf{n}},\hat{\mathbf{n}}')$.

Alternatively, we could expand the field in spherical harmonics $T(\hat{\mathbf{n}}) \equiv \sum_{\ell=0}^{\infty} T_\ell \equiv \sum_{\ell=0}^{\infty}\sum_{m=-\ell}^{\ell} a_{\ell m}Y_{\ell m}$, where the $a_{\ell m}$ are the coefficients of the expansion. If statistical isotropy is assumed, the angular power spectrum C_ℓ may be defined via $\langle a^*_{\ell m}a_{\ell' m'}\rangle = C_\ell\delta_{\ell\ell'}\delta_{mm'}$, where C_ℓ does not depend on the rotational degrees of freedom m. Hence, it is meaningful to calculate C_ℓ by averaging over the $(2\ell+1)$ (on a full sky) "samples" corresponding to the $(2\ell+1)$ values of m for each ℓ. However, without the assumption of statistical isotropy, we have in general

$$\langle a^*_{\ell m}a_{\ell' m'}\rangle = \tilde{C}_{\ell m\ell' m'}, \tag{2.2}$$

which is much more difficult to measure than C_ℓ since we get only one sample of $\tilde{C}_{\ell m\ell' m'}$ for each (ℓ, m, ℓ', m') in our universe. This is a big reason why statistical isotropy is such a crucial assumption in cosmology: it is much easier to work with C_ℓ than the much more complicated quantity above.

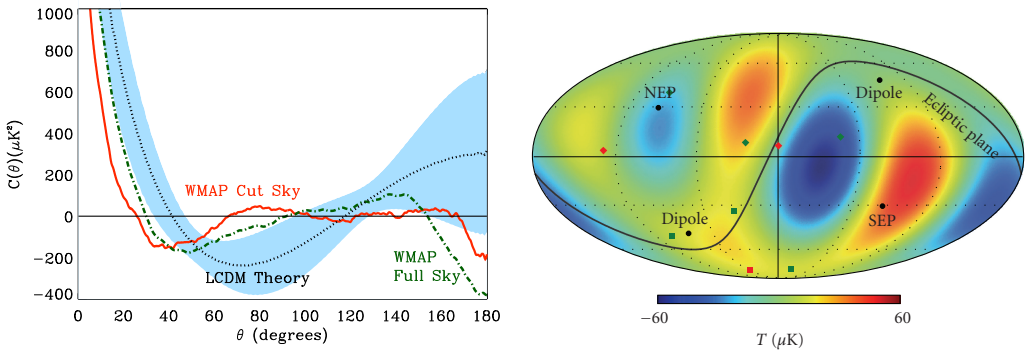

Figure 2.1: Anomalies in measurements of the cosmic microwave background. *Left:* Low power at large angles in the CMB. Measurements of the angular correlation function of the CMB on the cut sky (Galactic plane and other known sources of non-CMB microwave emission removed, which arguably gives the most reliable results) are very close to zero at angular scales above 60 degrees. This is unlikely in the standard ΛCDM model at the 0.03 percent level (Copi et al. (2009)). Figure adapted from Sarkar et al. (2011). *Right:* A combined map of the quadrupole and octopole of the cosmic microwave background temperature fluctuations. The WMAP-measured quadrupole and octopole are strongly aligned with one another, to an extent unexpected in ΛCDM (Copi et al. (2007)). In addition, the ecliptic plane neatly divides a large cold spot from a large hot spot in this map, an effect that is representative of several anomalies in which it appears the geometry and motion of the Solar System are correlated with (putatively cosmological) features of the CMB.

2.1.1 Point of Departure: Large-Scale Structure as Probe of CMB Anomalies

While measurements of the angular power spectrum of the CMB by the Wilkinson Microwave Anisotropy Probe (WMAP) experiment have provided strong support for the inflationary Hot Big Bang model and allowed for unprecedentedly precise determination of cosmological parameters, these successes have come along with various unexpected "anomalies" in the data. The literature on these anomalies is vast, and there has been much debate over whether some – or even all – of the anomalies are mere relics of the selection of *a posteriori* statistics and other unconvincingly arbitrary uses of the huge WMAP dataset (Bennett et al. (2011); Efstathiou et al. (2010); Pontzen and Peiris (2010); Aurich and Lustig (2010)).

For example, one anomaly that has received a great deal of attention involves the low power in the CMB at large angular scales. The angular correlation function of

the CMB, defined via

$$C(\theta) \equiv \left\langle \frac{\Delta T}{T}(\hat{n}) \frac{\Delta T}{T}(\hat{n}') \right\rangle_{\hat{n}\cdot\hat{n}'=\cos\theta}, \tag{2.3}$$

is unusually close to zero at angles $\theta \gtrsim 60^\circ$ (see Fig. 2.1). One way of quantifying how low $C(\theta)$ is at large angular scales uses the $S_{1/2}$ statistic, defined originally by the WMAP team (Bennett et al. (2003)) as

$$S_{1/2} \equiv \int_{-1}^{1/2} [C(\theta)]^2 \, d(\cos\theta). \tag{2.4}$$

WMAP measurements produce an $S_{1/2}$ statistic low enough to be unlikely in the standard ΛCDM model at the 0.03 percent level (Copi et al. (2009)). While it could be – and has been – argued that this choice of statistic is *a posteriori* (e.g., Efstathiou et al. (2010)), given (for example) the somewhat arbitrary cutoff at $\cos\theta = 1/2$ and the choice to square $C(\theta)$ in the integral rather than using an absolute value or a different even power, there is still good reason to suspect (e.g., Copi et al. (2007, 2009)) that WMAP measurements of the large-angle $C(\theta)$ disagree with ΛCDM. In particular, large-angle power was low in COBE (where this effect was first noted), lower in the initial WMAP results, and still lower in WMAP years 3-7. The fact that the signal has become more prominent with better and better data can be regarded as the signature of a genuine physical effect.

My own previous research has attempted to circumvent discussions of *a posteriori* statistics and focus on the question of whether other probes of large-scale correlations in our universe might used to cross-check and possibly validate CMB measurements. That is, if observations of the universe's large-scale structure could effectively probe the scales corresponding to $\theta > 60^\circ$ in the CMB, such observations could provide a new window on large-scale correlations that would rely on verifying predictions made in advance of data collections rather than *a posteriori* inferences after the fact.

In collaborations with Dragan Huterer and Wenjuan Fang of the University of Michigan, and Andrew Hearin and Andrew Zentner of the University of Pittsburgh, I have modeled primordial curvature power spectra $\Delta^2_R(k)$ with a roughly horizon-scale cutoff in power that would give rise to a CMB with suppressed power at large scales, and examined how much suppression would be necessary for the effect to be detectable in a future redshift survey (Gibelyou et al. (2010)) or galaxy imaging survey (Hearin et al. (2011)). In general, there is a tradeoff: as the scale of the cutoff in power becomes smaller and smaller (so that there is more and more suppression), $S_{1/2}$ likewise becomes smaller and (up to a point) in closer agreement with the WMAP-measured value. It also becomes easier and easier to rule out or detect suppression with large-scale-structure observations. But too much suppression (that is, suppression on much-smaller-than-horizon scales) leads to disagreement with the measured angular power spectrum C_ℓ of the CMB. For the details of these tensions and the relative likelihood of detecting large-scale suppression using galaxy surveys, see Gibelyou et al. (2010) and Hearin et al. (2011).

The idea of using large-scale-structure observations to (partially) independently test anomalous results in CMB measurements has, in general, not been heavily exploited. This is in part because the common assumption is that the CMB is always best for detecting any pattern on very large scales, and most of the anomalies involve such scales – low multipoles, or large angles in WMAP measurements. While it is true that the CMB, originating at redshift $z \sim 1100$ as it does, is the *best* probe of the largest scales in the universe, it is simply not the case that the CMB is the *only* viable probe of such scales. Also, large-scale-structure measurements add a third dimension that is absent in CMB observations.

This is where my previous research links up with the research in this thesis, which

concerns the question of statistical isotropy. There are already tantalizing hints of violations of statistical isotropy in CMB data; in fact, several observed anomalies, especially those indicating correlations between patterns in the CMB of (apparently) cosmological origin (e.g., the quadrupole and octopole) and the geometry and motion of the Solar System (see Fig. 2.1), can be understood as indications that statistical isotropy fails to hold. In addition, the southern ecliptic hemisphere has significantly more power than the northern ecliptic hemisphere on scales of about 3 degrees and larger (multipoles $\lesssim 60$) (Hoftuft et al. (2009)). This so-called "hemispherical power anomaly" is a dipole modulation (see the beginning of Chapter 3 for precise discussion of what this entails mathematically) of CMB power (direction in Galactic coordinates is $(l, b) = (224^\circ, -22^\circ)$) that is completely distinct from the measured CMB dipole C_1 (which is due to our motion with respect to the CMB rest frame), and is yet another possible indication of breaking of statistical isotropy in the CMB. (However, see Hanson and Lewis (2009) for the updated result that the significance of the hemispherical power anomaly decreases when smaller scales are taken into account: previous analyses had been done for $\ell \lesssim 60$; when analysis is extended out to $\ell \sim 500$, the effect becomes less than 3σ-anomalous. The fact that greater resolution reduces the significance of the signal calls into question the authenticity of the signal as a genuine cosmological effect.) Finally, the low power at large angles in $C(\theta)$ may itself be an indication that statistical isotropy is violated: it seems that a conspiracy of low-ℓ multipoles in the angular power spectrum C_ℓ is responsible for creating the suppressed $C(\theta)$ (Copi et al. (2009)), and correlations between different multipoles could be the result of a lack of statistical isotropy.

I take these considerations as general motivation for the work performed in the rest of this thesis, which will analyze the specific issue of dipole patterns in various

surveys being used as probes of the statistical isotropy of the universe.

2.2 Types of Dipoles: Specific Theoretical Considerations

It is completely expected that a dipole will be present in any survey of objects that trace large-scale structure. Both of the following effects contribute to the dipole: (a) there are local anisotropies since the universe is not homogeneous and isotropic except on its very largest scales, and (b) the Earth has a total motion relative to the large-scale-structure rest frame that is the sum of several vector contributions (Earth moves around the Sun, the Sun moves around the center of the Milky Way, the Milky Way moves with respect to the Local Group barycenter, and the Local Group barycenter moves with respect to the structure around it and, ultimately, the large-scale-structure rest frame). That motion produces dipole anisotropy due to two effects, the Doppler effect and relativistic aberration of angles (Itoh et al. (2010); see Sec. 2.2.3 for mathematical details). The Doppler effect is relevant because it changes how magnitude varies with frequency, and since LSS surveys invariably operate within limited frequency ranges, the Doppler effect may shift certain objects into or out of a magnitude-limited sample. Since frequencies will increase in the direction of motion and decrease in the opposite direction, this produces a small dipole in the number of objects detected. Meanwhile, relativistic aberration causes the measured positions of galaxies to be displaced toward our direction of motion. This effect is on the order of $v/c \sim 10^{-3}$, relevant for our purposes.

We expect that as we go from smaller to larger survey volumes, the measured value of the dipole amplitude should converge to that of the CMB dipole. This is because with larger survey volumes, we average over more and more structure, and the universe approaches homogeneity and isotropy. Any dipole left over should be

due only to our motion, a kinematic dipole (with amplitude on the order of 10^{-3}) just as in the CMB. There are several reasons why the dipole might not converge to that of the CMB. One is that the rest frame of the CMB is not the same as the rest frame of the LSS: novel horizon-scale physics (explored below) could induce a relative velocity between the CMB and LSS, so that galaxies would have a nonzero average streaming velocity with respect to the CMB rest frame. There is also the possibility that there is genuinely more mass (and therefore more galaxies/objects that trace the mass distribution) in one direction, corresponding to modulation of primordial curvature perturbations due to the physics of inflation. Scenarios in this vein, exploring the possibility that isocurvature perturbations produce such an effect (with an eye to explaining the CMB hemispherical power anomaly) have been advanced by Erickcek et al. (2009) and Erickcek et al. (2008b). Careful measurement of dipoles in various surveys, such as those we perform here, help zone in on these possibilities, which correspond to a violation of statistical isotropy.

The rest of this section will flesh out the details of the discussion in the preceding two paragraphs.

2.2.1 Flux-weighted dipole vs. 2D-Projected Dipole

One very commonly computed type of dipole is not, strictly speaking, a dipole at all, but is worth explaining in detail here because it is so frequently referred to as a dipole, and is strongly related to quantities that are genuine dipoles. This "dipole" is the flux-weighted dipole, where instead of calculating a (genuine) dipole based only on the two-dimensional projected positions of objects on the sky, some radial information is preserved by weighting each object by the flux we receive from it.

The flux-weighted dipole, as typically computed, is a measure of the acceleration due to gravity on the Local Group. In linear theory, the peculiar velocity $\mathbf{v(r)}$ at

position $\mathbf{r}$ is proportional to the peculiar acceleration vector $\mathbf{g(r)}$ induced by the matter distribution around position $\mathbf{r}$ (Erdogdu et al. (2006), Bilicki et al. (2011)):

$$\mathbf{v}(\mathbf{r}) = \frac{H_0 f(\Omega_M)}{4\pi G\bar{\rho}}\,\mathbf{g}(\mathbf{r}) = \frac{2f(\Omega_M)}{3H_0\Omega_M}\,\mathbf{g}(\mathbf{r})\ . \tag{2.5}$$

Here, $H_0 = 100\,h$ km/s/Mpc is the Hubble constant, Ω_M is the matter density divided by the critical density, and $f(\Omega_M) \equiv \left(\frac{d\ln D}{d\ln z}\right)|_{z=0}$ (where D is the growth factor). In the ΛCDM model, the factor $f(\Omega_M) \approx \Omega_M^{0.55}$ and is only weakly dependent on the cosmological constant (Lahav et al. (1991)). The acceleration vector itself is given by

$$\mathbf{g}(\mathbf{r}) = G\bar{\rho}\int \delta_M(\mathbf{r}')\,\frac{\mathbf{r}'-\mathbf{r}}{|\mathbf{r}'-\mathbf{r}|^3}\,d^3\mathbf{r}'\ , \tag{2.6}$$

where $\delta_M(\mathbf{r}) = \left[\rho_M(\mathbf{r}) - \bar{\rho}\right]/\bar{\rho}$ is the density contrast of the mass perturbations at the point $\mathbf{r}$.

Of course, we do not directly observe the mass distribution, but rather objects (usually galaxies) that trace the mass distribution. Assuming constant linear bias (which is expected to be a good approximation at large scales and for fixed galaxy type), $\delta_g = b\,\delta_M$, and using the fact that for a spherical survey $\int \frac{\mathbf{r}'-\mathbf{r}}{|\mathbf{r}'-\mathbf{r}|^3}\,d^3\mathbf{r}' = 0$, the peculiar acceleration becomes

$$\mathbf{g}(\mathbf{r}) = \frac{G}{b}\int \rho_g(\mathbf{r}')\,\frac{\mathbf{r}'-\mathbf{r}}{|\mathbf{r}'-\mathbf{r}|^3}\,d^3\mathbf{r}'\ . \tag{2.7}$$

Following Bilicki, Chodorowsky, and Jarrett, we create the parameter $\beta \equiv f(\Omega_M)/b$, in which case we can write

$$\mathbf{v} \propto \beta\,\mathbf{g}\ , \tag{2.8}$$

which demonstrates a result we will make use of in this thesis, despite the fact that it does not concern flux-weighted dipoles specifically: namely, *in linear theory, peculiar*

velocity is directly proportional to peculiar acceleration, and in particular, the peculiar velocity of the Local Group (the motion that makes the dominant contribution to the CMB kinematic dipole) is directly proportional to the acceleration due to gravity of the Local Group induced by all the matter in the universe, especially the local (on the order of 10^2 Mpc/h and closer) large-scale structure.

Note that in addition to observing galaxies rather than mass itself, we do not even observe a continuous galaxy density field, but rather discrete objects. Treating galaxies as point sources, $\rho_g(\mathbf{r}) = \sum_i M_i \, \delta_D(\mathbf{r} - \mathbf{r}_i)$, where δ_D is the Dirac delta function and M_i and $\mathbf{r}_i$ are the mass and the position of the i-th galaxy, the acceleration due to gravity of the local group becomes

$$\mathbf{g} = \frac{G}{b} \sum_i M_i \frac{\hat{\mathbf{r}}_i}{r_i^2}. \tag{2.9}$$

where the origin of the coordinate system is implicitly at the barycenter of the Local Group.

To see why a flux-weighted dipole is of interest, we put the above into a form that is useful for actual observational data. Noting that masses of individual galaxies are not typically known well, but that luminosities are easier to measure, we can write

$$\mathbf{g} = \frac{4\pi G}{b} \sum_i \frac{M_i}{L_i} \frac{L_i}{4\pi r_i^2} \hat{\mathbf{r}}_i = \frac{4\pi G}{b} \sum_i \frac{M_i}{L_i} S_i \hat{\mathbf{r}}_i \ , \tag{2.10}$$

where the i-th galaxy has an intrinsic luminosity L_i and a total flux received of $S_i = L_i / 4\pi r_i^2$. Hence if we have a sense of how the mass-to-light ratio behaves in a given band for a given survey, it becomes possible to estimate the acceleration of the Local Group from two-dimensional data plus photometry. If we finally assume (and this is of course a large assumption, though a very commonly made one) that the mass-to-light ratio is the same for all objects in the survey, $\Upsilon = \langle M/L \rangle$, we finally

obtain

$$\mathbf{g} = \frac{4\,\pi\,G\,\Upsilon}{b} \sum_i S_i \hat{\mathbf{r}}_i \ . \tag{2.11}$$

In words, the flux-weighted dipole takes the position vectors of the objects in a survey, weights according to their fluxes (viewed as a proxy for mass), and adds them together. See Bilicki, Chodorowsky, and Jarrett for some details and caveats to working with this formulation, but the outline above captures the basic reason why the flux-weighted dipole is a quantity of interest: by keeping radial information on objects in a survey by means of tracking their apparent magnitudes, it is possible to obtain a measure of the direction and strength of the acceleration of the Local Group due to the Newtonian gravitational attraction from objects in the survey. Both gravity and flux go as $1/r^2$, so light flux can be used as a proxy for gravitational force of attraction in the limit of constant M/L. The flux-weighted dipole from 2MASS is in the direction $(l, b) = (264.5°, 43.5°) \pm (2.0°, 4.0°)$ (Maller et al. (2003); note the rather serious discrepancy between the published result and the arXiv version); the flux-weighted dipole from 2MRS is in the direction $(l, b) = (251°, 38°)$ (Erdogdu et al. (2006)) in the Local Group frame, or $(245°, 39°)$ in the CMB frame.

2.2.2 2D-Projected Dipole: Local-Structure Dipole

For the rest of this section, and for almost the entirety of the rest of this thesis, I focus on what I term the 2D-projected dipole, which is the quantity that is usually indicated by the isolated use of the word "dipole." This quantity relies on objects at any given redshift being projected on the celestial sphere (hence "2D-projected") with no weighting scheme.

For a survey with very large (hundreds of Mpc- to Gpc-scale) volume, the universe is at least close to homogeneous and isotropic on the scales relevant for the survey.

We naturally expect that any dipole signal in such a large-volume survey will be strongly suppressed. However, on much smaller scales, where the universe is not at all homogeneous and isotropic, dipole signals should naturally emerge in any survey of objects that trace large-scale structure at all, and certainly in any galaxy survey. To take a particularly simple example, there is a large dipole in the galaxy distribution if we survey only objects within the Local Group.

But even if a survey encompasses structure on scales of tens of Mpc, we fully expect that given the non-uniformity of nearby structure, there should be a dipole component in the pattern of galaxies observed on the sky. This dipole component will be strongest for the smallest surveys, and should die away monotonically (at least in statistical average) for larger and larger surveys. The effect turns out to be on the order of 10^{-1} for scales of tens to a couple hundred of Mpc, meaning that the fluctuations (contributing to the dipole) in the number of galaxies, as a function of position on the sky, are on the order of 1/10 the size of the mean number of galaxies across the sky.

The precise way in which the angular power spectrum C_ℓ varies depending on survey depth in redshift is depicted in Chapter 3, Fig. 3.2. The formalism used to create these predictions is also explained in Chapter 3. In the figure, all multipoles out to $\ell = 1000$ are plotted, but attention should be focused on the dipole, $\ell = 1$. Note that as the maximum redshift of the survey increases, the amplitude of the local-structure dipole (expressed as C_1) is expected to drop over several orders of magnitude.

2.2.3 2D-Projected Dipole: Kinematic Dipole

A dipole pattern may also arise due to motion of the Earth with respect to the astrophysical objects or structure being measured. This is what produces the dipole

in the cosmic microwave background, and it also contributes to the total dipole in a measurement of the large-scale structure.

Kinematic Dipole in the CMB

Probably the best-known dipole in all of cosmology is the dipole measured in the CMB temperature distribution. This dipole, which has an amplitude on the order of 10^{-3} times the amplitude of the CMB monopole, arises due to the motion of the Solar System with respect to the CMB rest frame. This motion is the vector sum of several different motions, summarized in the table below.

Table 2.1: Motions that give rise to a kinematic dipole in the CMB and large-scale structure.

Motion	Approximate Speed (km/s)	Direction
Earth around Sun	~ 30 km/s	annually varying
Sun wrt Local Group	~ 306 km/s	$(l, b) = (99, -4) \pm (5, 4)$
Local Group wrt CMB	~ 622 km/s	$(l, b) = (272, 28)$
Overall CMB kinematic dipole	~ 370 km/s	$(l, b) = (264.4, 48.4) \pm (0.3, 0.5)$

Values of the kinematic dipole in the CMB are cited with the contribution from the Earth's motion around the Sun subtracted out, so that the dipole is due only to the Sun's velocity with respect to the CMB (Kogut et al. (1993)). The value of the Local Group's peculiar velocity with respect to the CMB is from Maller et al. (2003) and was computed using the value of the Sun's velocity with respect to the Local Group in Courteau and van den Bergh (1999). (When the velocity of the Local Group with respect to the CMB rest frame is inferred from the measurement of the CMB dipole, the direction becomes $(l, b) = (276, 30) \pm (3, 3)$. (Kogut et al. (1993))) The peculiar velocity predicted from linear-theory ΛCDM is ~ 470 km/s. Note that the speed of the Sun with respect to the CMB rest frame would be considerably greater if not for the fact that the Sun's velocity vector with respect to the Local Group points in a direction nearly opposite that of the Local Group's velocity vector

with respect to the CMB. Also note that the dominant contribution to the Sun's motion with respect to the Local Group is the Sun's motion around the center of the Galaxy, which has speed ~ 220 km/s, and is composed of the Sun's motion with respect to the Local Standard of Rest and the LSR's motion with respect to the Galactic Center (Itoh et al. (2010) and Courteau and van den Bergh (1999)). The value of, and error bars on, the CMB velocity dipole are taken from Kogut et al. (1993).

Kinematic Dipole in LSS

The kinematic dipole in the CMB, which is due to the Sun's motion with respect to the CMB rest frame, is observed as a Doppler shifting of the CMB photons. The effect that gives rise to a kinematic dipole in the large-scale structure is not quite as direct. Rather, it includes contributions both from the Doppler effect and relativistic aberration. We first address aberration, following the formalism of Burles and Rappaport (2006), who derive equations for aberration with the ultimate goal of showing that aberration of the CMB temperature might be detectable statistically by Planck, looking at shifts of CMB peaks. While this is not our goal, the formalism still holds.

We define a spherical-coordinate system with the z-axis in the direction of motion. If we take the "unprimed" frame to be the CMB frame, and the "primed" frame to be the frame of the Solar System barycenter, then the azimuthal angle ϕ is unchanged between frames: $\phi = \phi'$. However, the polar angle θ is affected as follows:

$$\sin\theta = \frac{\sin\theta'}{\gamma(1 - \beta\cos\theta')} \tag{2.12}$$

where β is the relative velocity of the Solar System with respect to the CMB, $\gamma = (1-\beta^2)^{-1/2}$ as usual, and $\theta = 0$ corresponds to the direction of forward motion.

With the assumption that β is small, which is a good assumption given that CMB observations show it to be on the order of 10^{-3}, expansion in a Taylor series gives

$$\sin\theta = \sin\theta'(1 + \beta\cos\theta'). \tag{2.13}$$

Finally, we take the arcsin of both sides and expand the arcsin function assuming small β to obtain

$$\theta = \theta' + \beta\sin\theta'. \tag{2.14}$$

We are ultimately interested in calculating how areas (and volumes) on the celestial sphere are stretched or compressed, and hence want the quantity $d\Omega/d\Omega'$. With that in mind, we compute

$$\frac{d\theta}{d\theta'} = 1 + \beta\cos\theta' \tag{2.15}$$

$$\frac{\sin\theta d\phi}{\sin\theta' d\phi'} = 1 + \beta\cos\theta' \ . \tag{2.16}$$

and find in the end that $d\Omega/d\Omega' = (1 + \beta\cos\theta')^2$. Hence areas and volumes on the sky, proportional to $\sin(\theta)d\theta d\phi$, change as $(1 + \beta\cos\theta')^2 \approx 1 + 2\beta\cos\theta'$.

Itoh et al. (2010) provide a more complete derivation of this, including both the Doppler effect (which changes frequencies and hence measured magnitudes since we never measure bolometric magnitudes) and relativistic aberration, and derive the following expression for the observed angular number density of galaxies $n(\theta)$ given the limiting magnitude $m_{\rm lim}$:

$$n(\theta, m < m_{\rm lim}) = \bar{n}(m < m_{\rm lim})\left[1 + 2\tilde{\beta}\cos\alpha\right] \tag{2.17}$$

where

$$\tilde{\beta} = [1 + 1.25x(1 - p)]\beta. \tag{2.18}$$

Here the intrinsic flux density of a galaxy is assumed to be a power law $S_{\rm rest}(\nu) \propto \nu^p$, and the intrinsic number counts of galaxies $\bar{n}$ is

$$\bar{n}(m < m_{\rm lim}) \propto 10^{x m_{\rm lim}} \tag{2.19}$$

where x is a numerical coefficient of order unity. The angle α is the angle between the angular direction θ and the angular direction of the Earth's peculiar velocity $\mathbf{v}$ on the celestial sphere, the same as θ', but with more convenient notation. The factor of 2 in $2\tilde{\beta}$ above comes from the same source as the square in $(1 + \beta \cos\theta')^2$ earlier. The correction for $\tilde{\beta}$ in Eq. (2.18) is the contribution of the Doppler effect to the overall kinematic dipole in observations of LSS.

2.2.4 2D-Projected Dipole: Intrinsic Dipole

In the CMB, the intrinsic dipole corresponding to adiabatic perturbations is zero (Erickcek et al. (2009)). Isocurvature perturbations can induce an intrinsic dipole, though we expect that any such intrinsic dipole will be swamped by the 10^{-3} kinematic dipole due to the velocity of the Solar System with respect to the CMB rest frame. When we switch over from talking about the CMB to talking about large-scale structure, we expect that there may also be an intrinsic dipole in the LSS. Given a scale-invariant power spectrum, all modes coming into the horizon at the present time have the same amplitude, and so there is no reason to expect the LSS intrinsic dipole to have an amplitude lower than any corresponding intrinsic dipole in the CMB. Below, we explore possible reasons why an intrinsic dipole might be higher-amplitude, competing with or even (conceivably) dominating the LSS kinematic dipole.

Erickcek et al. (2009) propose a scenario in which the curvaton (particle mediating a scalar field that may generate fluctuations during inflation without actually driving

inflation) has a large-scale spatial gradient, which in turn causes variation in the amplitude of the primordial curvature perturbations, modulating Δ_R across the sky. Hirata (2009) shows how this modulation due to isocurvature perturbations would transfer to the CMB and large-scale structure, in the latter case causing a dipolar variation in the abundance of massive haloes (and objects that occupy them). This inflationary scenario is one scenario that invokes the physics of the early universe to explain why there might be an intrinsic dipole in the large-scale structure above and beyond what we naturally expect to be present from typical scale-invariant fluctuations/adiabatic perturbations laid down in the simplest inflationary scenarios. While the simplest curvaton-gradient model has been ruled out by Hirata's analysis of constraints on the dipole in SDSS quasars (Hirata (2009)), and corresponding constraints on dipolar modulation of the primordial power spectrum,[1] similar but more complicated scenarios are still possible.

Note that Hirata's constraints on the primordial dipole amplitude using SDSS quasars are on the order of 2×10^{-2}, which corresponds to constraints on the amplitude of the dipole in the quasars themselves roughly an order of magnitude higher. Hence current constraints on this particular intrinsic-dipole scenario are not down to the level associated with the kinematic dipole, though this was not a problem in Hirata's analysis since that analysis looked specifically for a dipole effect that would accompany the primordial conditions needed to explain the CMB hemispherical power anomaly given the curvaton-gradient model, and that would have required a 10^{-1} dipole.

Another possibility for generating an intrinsic dipole is that the CMB rest frame is not the same as the large-scale-structure rest frame. One idea for how such an

[1] According to Hirata, any smooth gradient in the amplitude of the primordial curvature perturbations is no more than 2.7 percent per present-day horizon radius (99 percent confidence); cf. the 11 percent variation required in the Erickcek et al. model needed for consistency with the CMB hemispherical power anomaly.

effect might arise is the Grishchuk-Zel'dovich effect (Grishchuk and Zeldovich (1978); Erickcek et al. (2008a); see also Gunn (1988)); as Turner (1991) explains, if inflation lasts only a little longer than necessary to solve the flatness and horizon problems, scales that were superhorizon-sized at the onset of inflation – these scales cannot be affected by events during or later than the inflationary epoch, and thus contain imprints of the pre-inflationary universe – may not be much larger than our present horizon, and thus may have some effect in the current universe. In particular, he proposes that large density fluctuations with wavelengths slightly larger than the Hubble radius (modes that are "just barely" superhorizon-sized) may exist, and would appear to us as a density gradient in a particular direction. Such a density gradient could produce a "tilted universe": a universe in which all the matter within the Hubble volume gains a peculiar velocity due to the greater gravitational attraction from one "side" of the universe than the opposite. The effect is equivalent to saying that the rest frame of the CMB is not the same as the rest frame of large-scale structure: from the rest frame of the CMB, all matter would have a nonzero average streaming velocity. This would produce an intrinsic dipole due to relativistic aberration and the Doppler effect (or, equivalently, it would produce an additional kinematic dipole on top of that expected from analysis of the CMB) (Itoh et al. (2010)).

The Grishchuk-Zel'dovich effect would also produce an (additional) intrinsic dipole due to the simple fact of the superhorizon-scale density perturbation. As another example of physical mechanisms that would produce an intrinsic dipole, Gordon et al. (2005) examine a scenario in which there are spatial perturbations in the density of dark energy from a quintessence field: that is, a late-time effect produces horizon-scale fluctuations. More generally, Gordon et al. examine a class of models in which the full fundamental theory is homogeneous and statistically isotropic, but statisti-

cal isotropy is broken from a given observer's position because of superhorizon-scale perturbations that appear as a gradient in density across the sky on the largest observable scales. Any theory that generates such a variation in density would give rise to what I have termed an intrinsic large-scale-structure dipole, and the appearance of the breaking of statistical isotropy. These density variations could, at least theoretically (depending on the scenario, and the observational constraints that would apply to a given scenario), exist on essentially any order of magnitude in $\delta\rho/\rho$.

There is some reason to take the idea of a tilted universe seriously. Kashlinsky et al. (2008) investigate the bulk motion of galaxies in the universe out ~ 300 Mpc$/h$ and find, somewhat controversially (see, e.g., Keisler (2009)), that there is a coherent bulk flow in their sample. The evidence they develop for this claim comes from attempting to detect the kinetic Sunyaev-Zel'dovich effect by computing the dipole of the CMB temperature field evaluated at the positions of galaxy clusters. This dipole, evaluated as it is in a small number of pixels, does not receive appreciable contributions from our own motion (i.e., from the CMB kinematic dipole due to the Sun's motion with respect to the CMB rest frame), but does receive contributions from instrument noise, the thermal SZ effect, the *intrinsic* CMB dipole, and foreground components. However, contributions other than the kinematic SZ effect are, they argue, accounted for in their analysis, with the thermal SZ effect in particular canceling out/integrating down when averaged over a large number of clusters. Their conclusion is that the dipole in CMB temperature evaluated at cluster positions is due to the kinetic SZ effect due to the bulk flow of the cluster sample. If this effect is authentic, then it fits well with the tilted-universe scenario: the bulk motion is detectable in large-scale structure but does not generate a primordial dipole CMB component.

2.2.5 Types of Dipoles: Review

The following table visually classifies the types of dipoles outlined above, and summarizes some of the work that has been done observationally investigating the presence of such dipoles using various cosmological observations.

Table 2.2: Review of types of dipoles and where they are profiled in this chapter.

	local-structure dipole	kinematic dipole	intrinsic dipole
flux-weighted dipole	Sec. 2.2.1	N/A	N/A
2D-projected dipole	Sec. 2.2.2	Sec. 2.2.3	Sec. 2.2.4

In summary, when we observe some tracer of large-scale structure (galaxies, quasars, gamma-ray bursts, etc.), we may observe a dipole in counts. If the dipole we are observing is what I have called the 2D-projected dipole – that is, a dipole in surface density of the object – then contributions to that dipole may come from (1) the local-structure dipole, (2) the kinematic dipole (which is due to the Doppler effect and relativistic aberration), and (3) an intrinsic LSS dipole. There are a couple observations to make about these effects:

- In the limit of very high redshift, the local-structure dipole is expected to go to zero amplitude, the kinematic dipole is expected to go to amplitude $\sim v/c \sim 10^{-3}$ and align with the direction of the CMB dipole, and the intrinsic dipole could take on a wide variety of values depending on certain theoretical considerations.

- For structures/galaxies at relatively small redshifts, the local-structure dipole amplitude >> the kinematic dipole amplitude. However, even though the kinematic dipole is swamped by the local-structure dipole, we expect that these two dipoles should point in somewhere close to the same direction. While no particular level of agreement is guaranteed, the fact remains that local structure is

what accelerates us in the direction that the kinematic dipole points. This is why, in linear theory, the velocity of the Local Group is proportional to its acceleration due to gravity. However, since the 2D-projected dipole takes no radial information into account, it is not a true measure of gravitational attraction or acceleration, but only a partially reliable proxy.

2.3 Looking for Dipoles in Large-Scale-Structure Surveys

The search for dipoles in objects that (in some way) trace the large-scale structure of the universe can be performed using data from several completed surveys. One example is the Two-Micron All-Sky Survey (2MASS) (Skrutskie et al. (2006)), which completed its near-infrared observations in 2001. 2MASS has more than 99 percent sky coverage and includes both a point-source catalogue and an extended-source catalogue; the 1.6 million extended sources are of interest here since nearly all of them are extragalactic (and those which are not can be easily removed by getting rid of known artifacts and using judicious color cuts to take care of the rest). The survey's completeness is nearly uniform outside the Galactic plane for magnitudes below 13.5 in the K_s band. The survey's sky coverage and completeness make it an excellent choice for the sort of work explored in this thesis, since they reduce the amount of work necessary to get rid of instrumental artifacts in searching for violations of statistical isotropy.

The 2MASS Redshift Survey (2MRS) (Huchra et al. (2011)) also provides an excellent opportunity to perform tests of dipole patterns in objects of known redshift. The 2MRS team has assigned redshifts to over 40,000 2MASS extended sources, nearly all of which are within the range $0 < z < 0.1$, covering 91 percent of the sky (the Galactic plane is masked). Previous tests have worked with the flux-weighted dipole

in 2MRS (Erdogdu et al. (2006)), but have not explored the various contributions to the 2D-projected dipole.

Gamma-ray bursts (GRBs) from the Burst and Transient Source Experiment (BATSE; part of the Compton Gamma-Ray Observatory; Paciesas et al. (1999)) catalog also serve as a useful testing ground for dipolar modulation. The number of GRBs in BATSE, while only on the order of 10^3 and hence much smaller than the number of galaxies in 2MASS, is still substantial enough to provide useful constraints on the dipole. While Tegmark et al. (1995) have already produced the power spectrum of an earlier version of the BATSE catalogue, the more robust technique for determining the dipole using only real-space quantities, outlined in the next chapter, serves as a useful update to previous results, determines the direction as well as the magnitude of the dipole, and answers the question of whether the GRB distribution has been measured sufficiently well to distinguish it as a tracer of large-scale structure.

Finally, the NRAO VLA Sky Survey (NVSS) (Condon et al. (1998)) contains nearly 1.8 million extragalactic sources, observed in the radio portion of the spectrum. Our techniques contextualize and update the work of Blake and Wall (2002), who modeled the contributions of many of the most distant sources in NVSS to the dipole, and compared the result with the CMB dipole.

Accounting for systematics is necessary in each of these surveys. In all cases, one must deal with contamination from the Galactic plane. The GRB maps are arguably the most systematics-free of all the datasets we analyze. Confusion with sources within our Galaxy, such as soft gamma repeaters (SGRs), is extremely unlikely, though the positions of GRBs are not typically well-localized. In part because the detection threshold and energy range of the CGRO satellite were altered several times

during the mission, however, we cut out some sources and also check for variation of the dipole results with Galactic latitude, in this survey as in the others. If a determination of the amplitude of the dipole is consistent no matter how much of the Galactic plane is excised from the distribution of objects (performing isolatitude cuts of varying sizes is the consistency test we perform), this is an indication that confusion with Galactic sources (which would of course be concentrated near the Galactic plane) is minimal and, for our purposes, negligible.

In the case of the 2MASS/2MRS results, it will be necessary not only to account for possible star-galaxy confusion near the Galactic plane, and also address the issue of varying sky coverage, but also to explicitly account for extinction. The extinction maps of Schlegel et al. (1998), which give the distribution of dust along lines of sight in our sky, will be useful for these purposes. The pattern of extinction in these maps can be marginalized over and thus prevented from interfering with determinations of dipole amplitude and direction. Similarly, the 408 MHz map of Galactic radio emission in Haslam et al. (1981) and Haslam et al. (1982) can be used as a template in the case of NVSS, where the danger is not extinction but rather confusion between extragalactic sources and radio emission within our own Galaxy.

In short, the rest of this thesis will explore how to use different surveys with different systematics to compare theoretical predictions with observational results in dipole patterns observed in different classes of objects observed on our sky. We select surveys with very wide sky coverage, ideally almost full-sky coverage, because for a fixed depth, the number of modes available scales as the fraction of the sky covered, $f_{\rm sky}$. This is useful especially for beating down cosmic variance in theoretical predictions, which as we will see, is the dominant source of uncertainty in our comparisons of observations with theory (observational results tend to be much more

tightly constrained than theoretical predictions, since we are working at very low ℓ). Previous research on dipoles in similar surveys will be profiled as different types of surveys are brought up.

CHAPTER III

Formalism for Detection of Dipoles and Tests of the Dipole Estimator

This chapter outlines the formalism that will be used to search for dipoles in actual data from extragalactic sources in radio, infrared, and gamma rays.

3.1 Formalism for Detecting Dipoles

Some forays have already been made into tests of statistical isotropy, and dipoles in particular, using measurements of large-scale structure. Many estimators for the dipole have been employed, some of which do better jobs than others at naturally incorporating sky cuts, allowing for systematic effects to be accounted for, etc. The estimator used by Hirata (2009) in testing the WMAP hemispherical power anomaly (referenced in the previous chapter) using quasars detected by the Sloan Digital Sky Survey is an ideal estimator for determining the amplitude and direction of a dipole in counts of objects (not just quasars) on the sky under conditions of cut skies and in the presence of systematics.

Consider a dipolar modulation on the sky with some amplitude A in a (unit) direction $\hat{\mathbf{d}}$. We may write the observed density field N of the objects in question as a function of direction $\hat{\mathbf{n}}$ as

$$N(\hat{\mathbf{n}}) = [1 + A(\hat{\mathbf{d}} \cdot \hat{\mathbf{n}})]\bar{N} + \epsilon(\hat{\mathbf{n}}) \tag{3.1}$$

where $\bar{N}$ is the intrinsic statistically isotropic field and ϵ combines random and instrumental noise. If we momentarily drop the ϵ term, we find

$$N - \bar{N} = A\bar{N}(\hat{\mathbf{d}} \cdot \hat{\mathbf{n}}) \rightarrow \frac{\delta N}{\bar{N}} = A(\hat{\mathbf{d}} \cdot \hat{\mathbf{n}}). \tag{3.2}$$

Reinstating a term corresponding to systematic errors, the fluctuations in density as a function of direction can be written as the sum of contributions from a dipole, fluctuations due to systematics, and a mean offset (Hirata (2009)):

$$\frac{\delta N}{\bar{N}}(\hat{\mathbf{n}}) = A\hat{\mathbf{d}} \cdot \hat{\mathbf{n}} + \sum_i k_i t_i(\hat{\mathbf{n}}) + C. \tag{3.3}$$

Here $t_i(\hat{\mathbf{n}})$ are possible systematics templates in the sky map (such as an extinction map), the coefficients k_i give the amplitudes of the contributions of these systematics to the observed density field, and the presence of the monopole term, C, allows us to account for covariance between the monopole and other estimated parameters, especially covariance between the monopole and any systematic templates.

It is then straightforward to write down the best linear unbiased estimator of the combination ($\mathbf{d}$, k_i, C) with corresponding errors. The procedure is as follows: First, we rewrite the above equation as

$$\frac{\delta N}{\bar{N}}(\hat{\mathbf{n}}) = \mathbf{x} \cdot \mathbf{T}(\hat{\mathbf{n}}) \tag{3.4}$$

where $\mathbf{x} = (d_x, d_y, d_z, k_1, ..., k_N, C)$, $\mathbf{T}(\hat{\mathbf{n}}) = (n_x, n_y, n_z, t_1(\hat{n}), ..., t_N(\hat{n}), 1)$, and $n_x^2 + n_y^2 + n_z^2 = 1$.

The best linear unbiased estimator of $\mathbf{x}$ is

$$\hat{\mathbf{x}} = F^{-1} g \tag{3.5}$$

where

$$g_i = \int T_i(\hat{\mathbf{n}}) \delta N^{\Omega}(\hat{\mathbf{n}}) d^2\hat{\mathbf{n}}. \tag{3.6}$$

and

$$F_{ij} = \bar{N}^{\Omega} \int T_i(\hat{\mathbf{n}}) T_j(\hat{\mathbf{n}}) d^2\hat{\mathbf{n}}. \tag{3.7}$$

where $N^{\Omega} \equiv dN/d\Omega$ is the number of galaxies per steradian. To actually compute these quantities with discretized data, it is convenient to work with a data map and a random map, the latter of which is simply a set of randomly chosen directions/points $\hat{\mathbf{n}}_R$ on the unit sphere:

$$g_i = \sum_D T_i(\hat{\mathbf{n}}_D) - \frac{N_D}{N_R} \sum_R T_i(\hat{\mathbf{n}}_R) \tag{3.8}$$

$$F_{ij} = \frac{N_D}{N_R} \sum_R T_i(\hat{\mathbf{n}}_R) T_j(\hat{\mathbf{n}}_R) \tag{3.9}$$

where N_D and N_R represent galaxy counts rather than the number of galaxies per steradian as in the continuous case.

Note that the component of g corresponding to the monopole term in Equation (3.3), which we will refer to as g_C, must be zero, even if the sky is cut. This can be seen in the analytic formula for g by noting that we are integrating fluctuations relative to the mean, where the mean is determined from whatever portion of the sky is being integrated over. In the formulation where we discretize the celestial sphere, $g_C = N_D - (N_D/N_R)(N_R) = 0$; g_C represents the monopole of the fluctuations from the mean on the cut sky, which must be zero. Hence, the only way the monopole term C in Equation (3.3) can be nonzero is by picking up on the covariances between variables.

We prove that the estimator is unbiased, using the continuous formalism. Combining Eq. (3.2) and Eq. (3.6) in the continuous case,

$$g = A\bar{N}^{\Omega} \int \hat{\mathbf{n}}(\hat{\mathbf{n}} \cdot \hat{\mathbf{d}}) d^2\hat{\mathbf{n}}. \tag{3.10}$$

The vector g contains information about whatever dipole signal there may be. Specializing to the case where the dipole is in the z-direction,

$$\langle g_x \rangle = A\,\bar{N}^{\Omega} \int n_x(\cos\theta)\sin\theta d\theta d\phi = A\,\bar{N}^{\Omega} \int \sin\theta\cos\phi\cos\theta\sin\theta d\theta d\phi = 0 \tag{3.11}$$

where we have used the fact that the dipole is in the z-direction to replace $\hat{n}\cdot\hat{d}$ with $\cos\theta$. By similar calculation $g_y = 0$ and

$$\langle g_z \rangle = (4\pi/3)A\bar{N}^{\Omega} = A\,\frac{\bar{N}}{3}. \tag{3.12}$$

More generally, $g_z = (\bar{N}/3)A\,|\hat{d}|_z$, where $|\hat{d}|_z$ is the z-component of the unit vector of the dipole modulation.

The Fisher matrix is

$$\begin{aligned} F_{ij} &= \bar{N}^{\Omega} \int n_i n_j d^2\hat{\mathbf{n}} \\ &= \bar{N}^{\Omega} \int (\sin\theta\cos\phi, \sin\theta\sin\phi, \cos\theta)(\sin\theta\cos\phi, \sin\theta\sin\phi, \cos\theta)\sin\theta d\theta d\phi \\ &= (4\pi/3)\bar{N}^{\Omega}\mathbb{I} \\ &= \frac{\bar{N}}{3}\mathbb{I} \end{aligned}$$

where $\mathbb{I}$ is the identity matrix.

So

$$\langle \hat{x} \rangle = F^{-1}\langle g \rangle = \frac{3}{\bar{N}}(\mathbb{I})\frac{A\bar{N}}{3}\begin{pmatrix} |\hat{d}|_x \\ |\hat{d}|_y \\ |\hat{d}|_z \end{pmatrix} = \begin{pmatrix} d_x \\ d_y \\ d_z \end{pmatrix} \tag{3.13}$$

so that the estimator is, as expected, unbiased.

To show explicitly how we calculate the Fisher matrix F_{ij} in the discrete formalism, we take F_{zz} as an example:

$$F_{zz} = \frac{N_D}{N_R}\sum_{i=1}^{N_R} n_{z_i} n_{z_i} = \frac{N_D}{N_R}\sum_{i=1}^{N_R} z_i^2 = \left(\frac{N_D}{N_R}\right)(N_R)\left\langle z^2 \right\rangle = N_D\left\langle z^2 \right\rangle \tag{3.14}$$

where we have used z to designate the z-coordinate of the vector pointing to the center of the pixel in which count i is found. Since $\langle z^2 \rangle = 1/3$ over the entire sphere, we have $F_{zz} = N_D/3$ (for the entire celestial sphere) in the limit of sufficiently large number of counts in the random map to have suppressed Poisson noise.

The matrix F_{ij} is the Fisher matrix, and hence the covariance matrix is $\mathrm{Cov}(\hat{\mathbf{x}}) = F^{-1}$. By the Cramer-Rao inequality, the best-case marginalized errors on parameters $p_i = \{d_x, d_y, d_z, k_1, ..., k_N, C\}$ are

$$\sigma_{\mathrm{marg},i} = \sqrt{(F^{-1}_{ii})}; \tag{3.15}$$

inverting F automatically mixes all the elements together and takes into account how they covary. Meanwhile, the best-case unmarginalized errors are

$$\sigma_{\mathrm{unmarg},i} = 1/\sqrt{F_{ii}}. \tag{3.16}$$

Note that the errors on our estimates of the dipole are based on the shape of the sky cut, the input systematic templates, and the number of data points N_D.

As a side note, the correlation between parameters p_i and p_j is

$$\rho_{ij} = \frac{F^{-1}_{ij}}{\sqrt{(F^{-1}_{ii} F^{-1}_{jj})}}. \tag{3.17}$$

This formalism is useful, and an improvement upon previously used dipole-finding techniques, for several reasons. First, the real-space estimator employed here is arguably more convenient to implement than multipole-space estimators employed in previous analyses (e.g., Frith et al. (2005a), Blake and Wall (2002), Baleisis et al. (1998), etc.). Many analyses use pseudo-C_ℓ to deal with sky cuts, while sky cuts are very straightforward to deal with in this formalism (see Sec. 3.2 for further details). Finally, estimating the coefficients k_i allows one to very naturally incorporate any systematics templates one suspects might be relevant and ensure that they do not

interfere with estimation of the dipole. This form of component separation allows one to isolate the different contributions to the observed fluctuations in counts, and separate those contributions into actual dipole plus systematic effects. Any pattern put into this formalism as a systematic template will be marginalized over in the determination of dipole amplitude and direction $A\hat{\mathbf{d}}$.

Note that in all this formalism, we never combine the components of the dipole; we just acquire the components of the dipole (d_x, d_y, d_z), and the associated errors $(\sigma_x, \sigma_y, \sigma_z)$. Combining the components by squaring, summing, and taking the square root of the sum would create a biased estimator of the dipole amplitude A. Instead, once we have the magnitude and direction of the best-fit dipole $\mathbf{d_{best}} \equiv A\hat{\mathbf{d}}$, we can construct a marginalized likelihood function for the amplitude A (again following Hirata):

$$\mathcal{L}(A) \propto \int \exp\left[-\frac{1}{2}(A\hat{\mathbf{n}} - \mathbf{d_{best}})\mathrm{Cov}^{-1}(A\hat{\mathbf{n}} - \mathbf{d_{best}})\right] d^2\hat{\mathbf{n}} \tag{3.18}$$

where $d^2\hat{\mathbf{n}}$ indicates integration over all possible directions on the sphere. In this equation, for a given amplitude A, we take the best-fit dipole $\mathbf{d_{best}}$ as a given, and then compare each direction $\hat{\mathbf{n}}$ (with the given amplitude) with the best-fit dipole. The likelihood function is a Gaussian in A for fixed direction $\hat{\mathbf{n}}$, by construction, but may not be Gaussian when marginalized over direction. That marginalization occurs in the equation above when we integrate over all $\hat{\mathbf{n}}$, giving us the likelihood of a particular amplitude A marginalized over all directions, given the best-fit dipole $\mathbf{d_{best}}$ "selected" by the data. Posterior analysis will then show where 95 percent of the weight lies.

Given that we ultimately work discretely, with a celestial sphere that is pixellized using HEALPix routines (Górski et al. (2005)), the likelihood turns into a sum over

pixels:

$$\mathcal{L}(A) \propto \sum \exp\left[-\frac{1}{2}(A\hat{\mathbf{n}} - \mathbf{d_{best}})\mathrm{Cov}^{-1}(A\hat{\mathbf{n}} - \mathbf{d_{best}})\right] \Delta Area \tag{3.19}$$

The factor $\Delta Area$ will come out of the summation since all pixel areas are equal in HEALPix and all that matters is the ratio of likelihoods rather than the absolute values of likelihoods, so we literally sum over all the pixels in order to get the marginalized $\mathcal{L}(A)$. We drop the prefactor on the likelihood that includes covariance since the covariance does not depend on parameters.

Finding the likelihood distribution as a function of direction, $\mathcal{L}(\hat{\mathbf{n}})$, follows from an exactly analogous procedure, but we sum over all possible amplitudes associated with a given pixel rather than over all possible pixels associated with a given amplitude.

3.1.1 Converting From Dipole Amplitude A to Angular Power Spectrum C_1

Here we show that there is a simple relationship between the angular power spectrum dipole C_1, familiar from several areas of cosmology, and the amplitude A of the dipole computed above. Without loss of generality, we assume that the dipole points in the positive z direction and write the fluctuation in counts in two ways:

$$\frac{\delta N}{N}(\hat{\mathbf{n}}) = A\hat{\mathbf{n}} \cdot \hat{\mathbf{d}} = A\cos\theta = a_{10}Y_{10}(\hat{n}) \tag{3.20}$$

where $Y_{10} = \sqrt{3/(4\pi)}\cos(\theta)$. Therefore,

$$a_{10} = \sqrt{\frac{4\pi}{3}}A. \tag{3.21}$$

The power spectrum C_1 contribution is then given by

$$C_1 \equiv \frac{\sum_{m=-1}^{1}|a_{1m}|^2}{2\cdot 1 + 1} = \frac{a_{10}^2}{3} \tag{3.22}$$

and thus

$$C_1 = \frac{4\pi}{9}A^2. \tag{3.23}$$

For the purposes of order-of-magnitude calculations, the rule of the thumb is $C_1 \sim A^2$.

3.2 Commentary on the Formalism

This formalism has several noteworthy features:

- It allows very naturally for arbitrary sky cuts: all that is necessary is to remove pixels (which is NOT the same as setting these pixels equal to zero) from both the data map and the random map when performing the dipole analysis. When the sky is cut, the dipole becomes coupled to other multipoles, and the errors on the detection of d_x, d_y, and d_z derived from the Fisher matrix correspondingly increase to account for this.

- It allows for straightforward incorporation of arbitrary pixellization. The scale of the pixellization should not matter, because Poisson noise is on the scale of the pixellization, which is much smaller than the scale of the dipole, and Poisson noise in larger pixels means a smaller effect (goes as $1/\sqrt{N}$), so the Poisson noise cancels out. However, different pixellization schemes can affect the size, shape, and nature of a mask if there is any sky cut, and when discrepancies appear between dipole results using different pixellization schemes, it is virtually always traceable to this.

- It allows for the possibility of $A > 1$. This may seem counterintuitive since it implies negative counts in some pixels. However, even though it is true that counts cannot go negative in real data, it is still possible for a *model* in which some pixels have negative counts to be the best fit to the data.

One simple sanity check that we perform: If a pure-dipole map is created with the dipole pointing in the z-direction, and this map is used as a template $t(\hat{\mathbf{n}})$, the effect is that the detection of the dipole in the z-direction, d_z, gives an unreliable number, while the error bar in the z-direction, σ_z, blows up to a much larger number

than d_z, so that $(S/N)_z = d_z/\sigma_z << 1$. Also, the correlation ρ_{zk} between d_z and the template coefficient k becomes 1.0. The same pattern holds if we replace the z-direction with the x- or y-direction. A dipole template in a given direction takes out any component of the dipole detection in that direction.

Another note when applying this formalism: In order to do a realistic comparison of theory with observation, we must take bias into account. The formalism presented above can only detect dipoles in the distribution of galaxies or other astrophysical objects that serve as (presumably biased) tracers of large-scale structure, not in the underlying matter (dark plus baryonic) distribution itself. Therefore, when we compare observations with theory, we will always apply a bias correction to the theoretical prediction before comparing with observations.

See Appendix B for other simple test cases/sanity checks in which this formalism is applied to maps with a pure dipole and a pure monopole.

3.3 Systematics Templates

Figure 3.1 shows the systematics templates $t_i(\hat{\mathbf{n}})$ that we use in order to ensure that systematic effects do not mimic the effect of an actual dipole on the objects we are observing. The templates are the extinction map of Schlegel et al. (1998) and the map of Galactic synchrotron radiation of Haslam et al. (1981) and Haslam et al. (1982).

The Haslam et al. map is a 408 MHz radio continuum map of the entire sky that combines data from four different surveys and is dominated by synchrotron emission. Information about foreground emission is important when dealing with a radio survey such as NVSS, and we can apply this map as a systematic template since NVSS could plausibly pick up non-extragalactic signal from this emission.

The SFD map is an intensity map of the sky at 100 microns, a reprocessed composite of the COBE/DIRBE and IRAS/ISSA maps, that presents emission dominated by the same dust that causes extinction at many wavelengths – most notably in the optical. The resolution is on the order of a few arcminutes, and so the SFD map can in general be used to reliably derive extinction due to dust, assuming a standard reddening law. This works best away from the plane of the Galaxy, since within the Galactic plane dust conditions tend to fluctuate much more strongly on small scales than they do away from the Galactic plane (with the possibility of multiple dust temperature distributions, variable grain sizes, etc.). However, since we work almost exclusively well away from the Galactic equator, we do not expect this to be an issue. We apply the template to 2MASS and 2MRS in particular, since we expect that dust extinction is a particularly worrisome potential source of non-extragalactic signal or other corruption of the results of these surveys.

Both the Haslam and SFD maps are nearly parity-even in Galactic coordinates, as the Galaxy is itself nearly parity-even, so when the sky is symmetrically cut (as it typically is in the test cases of Appendix B as well as the real data from 2MASS and 2MRS in chapter 4), extinction is not likely to contribute to, or diminish, a dipole-like (parity-odd) signal, at least not in the z-direction. However, we still include it as a much-needed precaution against a known source of systematic error.

3.4 Theoretical Predictions

The angular power spectrum of density fluctuations of halos is usually expressed within the Limber approximation, where the contribution of modes parallel to the line of sight is ignored. In this approximation, the angular power spectrum is given

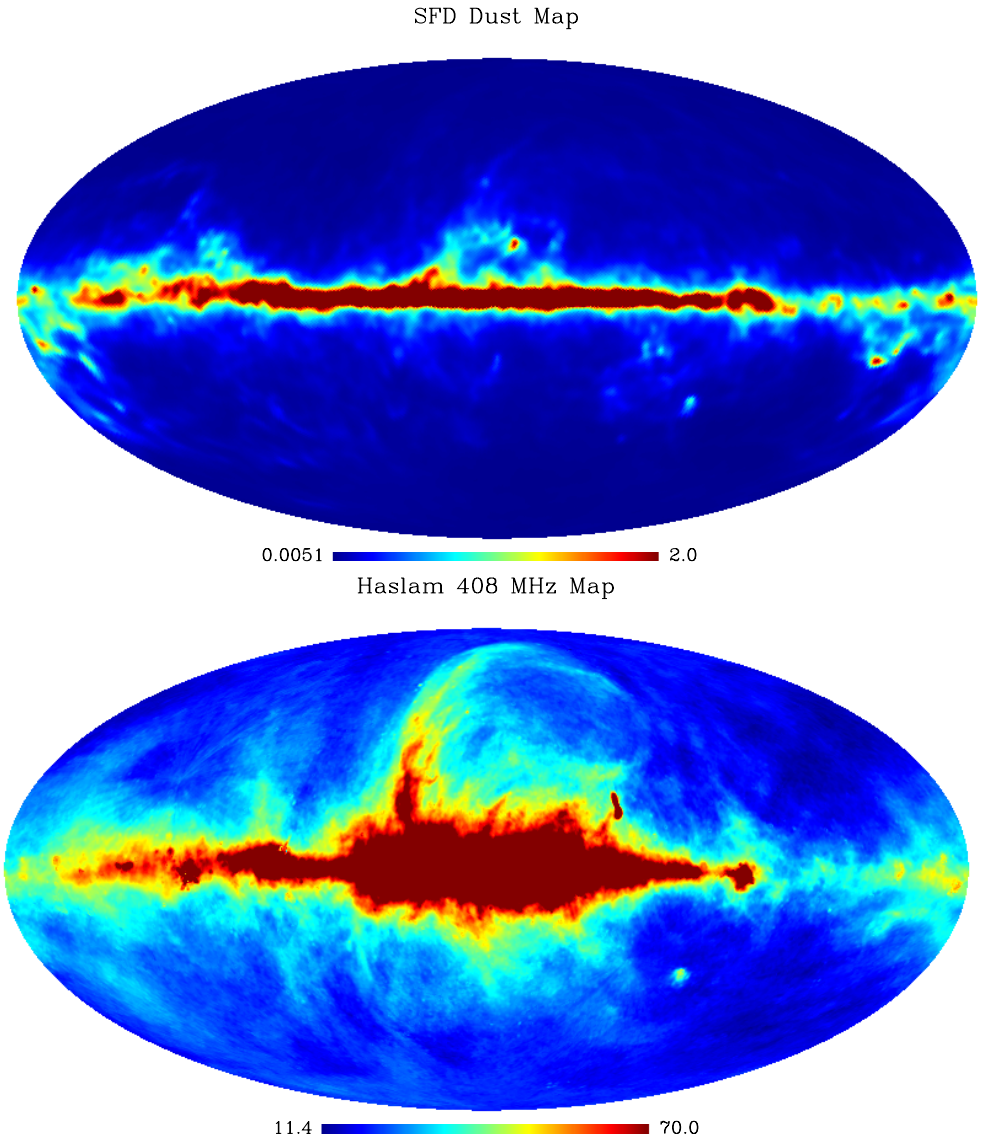

Figure 3.1: *Top:* The 100-micron intensity map of Schlegel et al. (1998), HEALPix resolution NSIDE=128. The map is used to derive the extinction due to dust in the Galaxy. *Bottom:* The 408 MHz map of Haslam et al. (1981)/Haslam et al. (1982), HEALPix resolution NSIDE=512. The map, dominated by synchrotron emission, is a useful template when working with a radio survey such as NVSS. (Note that in each case, the dynamic range of the map has been restricted so that the structure of the map, especially the structure at high Galactic latitudes, can be seen clearly. The Galactic Bulge is of course brighter at both 100 microns and 408 MHz than other Galactic longitudes.)

by

$$C_\ell = \frac{2\pi^2}{\ell^3} \int_0^\infty dz \, \frac{W^2(z)}{r(z)^2 H(z)} \Delta^2 \left(k = \frac{\ell}{r(z)}, z \right), \tag{3.24}$$

where $\Delta^2(k) \equiv k^3 P(k)/(2\pi^2)$ is the dimensionless power spectrum, $r(z)$ is the comoving distance, and $H(z)$ is the Hubble parameter. The weight $W(z)$ is given by

$$W(z) = \frac{b(z)N(z)}{\int_{z_{\rm min}}^{z_{\rm max}} N(z) dz}, \tag{3.25}$$

where $z_{\rm min}$ and $z_{\rm max}$ are the lower and upper end of the redshift range, and $N(z)$ is the radial distribution of galaxies.[1] We adopt the tabulated values, or else functional form, of $N(z)$ directly from the respective surveys that we study.

However, we are interested in the dipole $\ell = 1$ where the Limber approximation is not accurate anymore (it is accurate at $\ell \gtrsim 10$); see Fig. 3.2. Therefore, we adopt the exact expression for the power spectrum; using notation from (e.g.) Hearin et al. (2011), this is

$$C_\ell = 4\pi \int_0^\infty d\ln k \, \Delta^2 (k, z=0) \, I^2(k) \tag{3.26}$$

$$I(k) \equiv \int_0^\infty dz \, W(z) D(z) \, j_\ell(k\chi(z)) \tag{3.27}$$

where $\chi(r)$ is the radial distance, and $\chi(z) = r(z)$ in a flat universe, the case that we consider. Here $D(z)$ is the linear growth function of density fluctuations, so that $\delta(z) = D(z)\delta(0)$, where $D(0) = 1$. Note that, over the shallow range for 2MASS we can assume that $b(z)$ is constant, and factor it outside of Eqs. (3.26) and (3.27), but over the much deeper range for NVSS the bias may vary with redshift, and we adopt the expression for $W(z)$ from Ho et al. (2008) that implicitly integrates bias and number density as per Eq. (3.25). This is explained in detail in Chapter 5.

[1] Note that a sometimes-used alternative definition of $n(z)$ refers to the spatial density of galaxies, and contains additional volume factors; e.g. Hu and Jain (2004). Note also that our $W(z)$ is equivalent to the quantity $f(z)$ from Ho et al. (2008).

To produce the fiducial theoretical predictions, we consider the standard cosmological model with the following parameter values: matter density relative to critical $\Omega_M = 0.25$, equation of state parameter $w = -1$, spectral index $n = 0.96$, and amplitude of the matter power spectrum $\ln A$ where $A = 2.3 \times 10^{-9}$ (corresponding to $\sigma_8 = 0.8$) defined at scale $k = 0.002$ Mpc^{-1}. The power spectrum $\Delta^2(k, z) \equiv k^3 P(k)/(2\pi^2)$ is calculated using the transfer function output by CAMB. We do not vary the values of cosmological parameters, since they are measured to sufficient accuracy that any shifts in predicted dipole amplitude that could occur due to realistic changes in cosmological parameters are tiny in comparison with cosmic variance given the finite sky coverage and relative shallowness of the surveys we employ (as we have explicitly verified).

The power spectra are shown in Fig. 3.2. Note the substantial, order-unity, difference between the exact and approximate (Limber) expressions at $\ell = 1$. Clearly, the exact expression requires solving the double integral while the Limber approximation involves only a single integral, but we only need evaluate the power spectrum once (for each survey) at $\ell = 1$, so this does not present a difficulty.

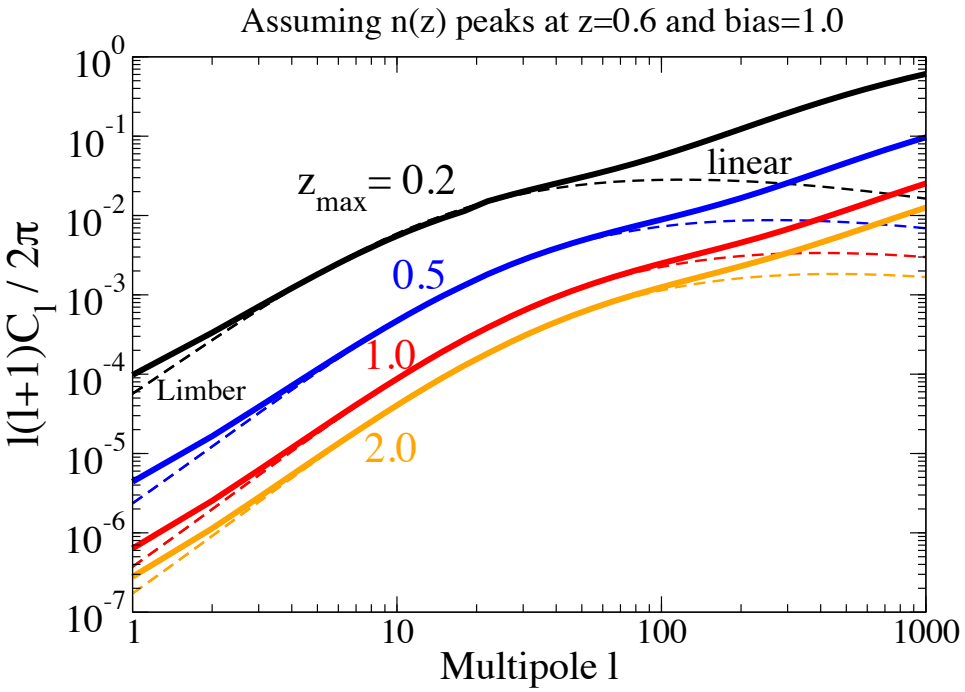

Figure 3.2: A plot of the angular power spectrum C_ℓ predicted for a galaxy survey with a peak in the galaxy redshift distribution at $z = 0.6$ and the given maximum depth $z_{\rm max}$. We focus attention on the dipole, $\ell = 1$: for these purposes, this plot gives C_1/π, equal to $\frac{4}{9}A^2$, so that A is just 3/2 times the square root of whatever is plotted in this graph for C_1. For this particular redshift distribution, the local-structure dipole becomes subdominant to the kinematic dipole for around $z_{\rm max} \sim 1.0$. For higher $z_{\rm max}$, we should get convergence to the kinematic dipole plus any intrinsic dipole that might be present. The peak in the radial profile of galaxies at $z \sim 0.6$ corresponds roughly to parameters for the Dark Energy Survey (DES). Bias $b = 1.0$ is assumed throughout. The dotted curves correspond to the power spectrum within the Limber approximation (low ℓ) and assuming linearity (high ℓ); the solid curves correspond to the more accurate set of assumptions where the Limber approximation is relaxed and nonlinearity is taken into account.

CHAPTER IV

Dipoles in the 2-Micron All-Sky Survey (2MASS) and the 2MASS Redshift Survey

4.1 Previous Results

The Two Micron All Sky Survey (2MASS), which imaged 99.998 percent of the celestial sphere (Skrutskie et al. (2006)), provides an excellent starting point in testing for dipoles in tracers of large-scale structure. This survey includes two main catalogs, the point-source catalog (PSC) and extended-source catalog (XSC). The latter is of interest here, since it includes roughly 1.6 million sources, nearly all of which are extragalactic.

2MASS used two 1.3-m equatorial Cassegrain telescopes, one in the Northern Hemisphere and one in the Southern Hemisphere (Mt. Hopkins, Arizona; Cerro Tololo, Chile), to observe in the J, H, and K_s bands, corresponding to wavelengths of 1.25, 1.65, and 2.16 μm, respectively. The XSC contains sources that are extended with respect to the instantaneous point-spread function (Skrutskie et al. (2006)), including galaxies and Galactic nebulae. The S/N=10 sensitivity limits are met by sources as bright or brighter than 15.0, 14.3, and 13.5 mag in the J, H, and K_s bands, respectively, and (very importantly for our dipole-related considerations) exhibit a mean color difference of less than 0.01 mag between hemispheres, meaning that the photometry is highly uniform between hemispheres. The reliability (corre-

sponding to the ratio of the number of genuine extended sources to the total number of sources, spurious or genuinely extended, in the dataset) of the XSC is greater than 99 percent for Galactic latitude $|b| > 20°$. Some extended sources in the catalog are not extragalactic, though these can be easily removed with the right color cuts (as detailed later in this chapter).

A small subset of the 1.6 million extended sources in the 2MASS XSC were assigned redshifts in the 2MASS Redshift Survey (2MRS), a catalog which includes position and redshift information for over 40,000 galaxies present in the original 2MASS sample. In this chapter, we apply the dipole-detecting formalism outlined in Chapter 3 to the entire 2MRS catalog, as well as to appropriate subsets of the 2MASS XSC sources.

Erdogdu et al. (2006) and Maller et al. (2003) have calculated the flux-weighted dipoles (see Sec. 2.2.1) for 2MRS (a 23,000-galaxy subset thereof, actually, with $K_s < 11.25$ – a preliminary version of the catalog) and 2MASS, respectively. This stands in a longer tradition of attempting to calculate flux-weighted dipoles from near-infrared surveys, since near-infrared light closely traces the mass distribution of large-scale structure. For instance, Rowan-Robinson et al. (2000) calculate a flux-weighted dipole from the IRAS PSCz Redshift Survey, which had redshifts for over 15,000 IRAS galaxies (at 60 μm; cf. the wavelengths of 2MASS, over an order of magnitude shorter). The IRAS PSCz ($z_{\max} \sim 0.1$), 2MRS ($z_{\max} \sim 0.1$), and 2MASS XSC ($\bar{z} > 0.07$) studies all find tolerably small discrepancies between the direction of the flux-weighted dipole (and thus the acceleration of the Local Group) and the CMB velocity dipole that partially results from that acceleration (velocity of the Local Group being proportional to acceleration of the Local Group in linear theory). (As noted before, the motion of the Sun with respect to the Local Group also

contributes to the kinematic dipole, but the direction is nearly opposite the direction of the Local Group's motion with respect to the CMB rest frame, and hence changes the magnitude of the velocity vector but does not substantially change its direction.)

The number-weighted dipole of Erdogdu et al. (2006) comes closer than the flux-weighted dipole to mimicking the quantity that we calculate here, but the number-weighted dipole, like the closely related flux-weighted dipole, is another quantity that seeks to measure the acceleration of the Local Group due to surrounding large-scale structure, but instead of using flux as a proxy for mass as in the flux-weighted dipole, the number density of galaxies in a given direction on the sky is assumed to serve as a good proxy for mass. Our goals and aims, as well as the precise quantity we calculate, are different: We seek to measure not an acceleration, but rather the simple 2D-projected dipole, which in the case of the relatively nearby survey 2MASS (and 2MRS, as a subset of 2MASS), is dominated completely by the contributions from the local-structure dipole (see Sec. 2.2.2).

The entire power spectrum of 2MASS has been calculated by Frith, Outram, and Shanks, which means that at least one measure of the 2D-projected dipole that we explore here has already been obtained. We compare our results to this previous result later in this chapter. However, we do not regard our result as a simple replication of the previous result (and, in fact, we note substantial disagreement): we compute not just the amplitude of the dipole, but also its direction; we use an estimator specifically designed to be the best unbiased estimator for the dipole; and we place the 2MASS dipole into a larger context of exploring the various contributions to dipoles, and testing observational results against theoretical predictions, in a wide variety of surveys.

4.2 Dipole in 2MRS

We begin with the 2MASS Redshift Survey, the densest all-sky redshift survey to date (Erdogdu et al. (2006)). The 2MRS team (Huchra et al. (2011)) measured redshifts of 43,533 bright ($K_s < 11.75$) sources with $E(B-V) \leq 1$ mag and $|b| \geq 5°$ (for $30° \leq l \leq 330°$; $|b| \geq 8°$ otherwise). Sources were carefully screened to ensure that all were genuinely extragalactic sources and do not have compromised photometry. As explained below, we err on the conservative side and make a symmetric cut at $|b| < 8°$ for all Galactic longitudes l, which eliminates roughly 1700 of the galaxies in the survey.

The results for the dipole amplitude in this survey are strongly expected to agree with theoretical predictions. Given the relatively small volumes surveyed (and the fact that we are dealing with the very large-scale $\ell = 1$ mode), cosmic variance is very large, and so a discrepancy between theory and observation would require highly anomalous observations. We find, even with relatively cursory checks, that there are no serious discrepancies between theory and observation for 2MRS. Nevertheless, in the coming sections, we profile the various tests performed on the data, and the results for both dipole direction and amplitude, in the interests of presenting results for this survey as something of a model (in addition to being an important test in its own right): this is a dataset with well-controlled systematics and very little chance of giving anomalous results, where we can test out several different types of systematic checks, to gain intuition for what results should look like when we perform similar tests on surveys at higher redshifts and/or with less well-understood systematics.

This survey is essentially ready to be analyzed "straight out of the box," meaning that major systematic errors have already been addressed (especially Galactic

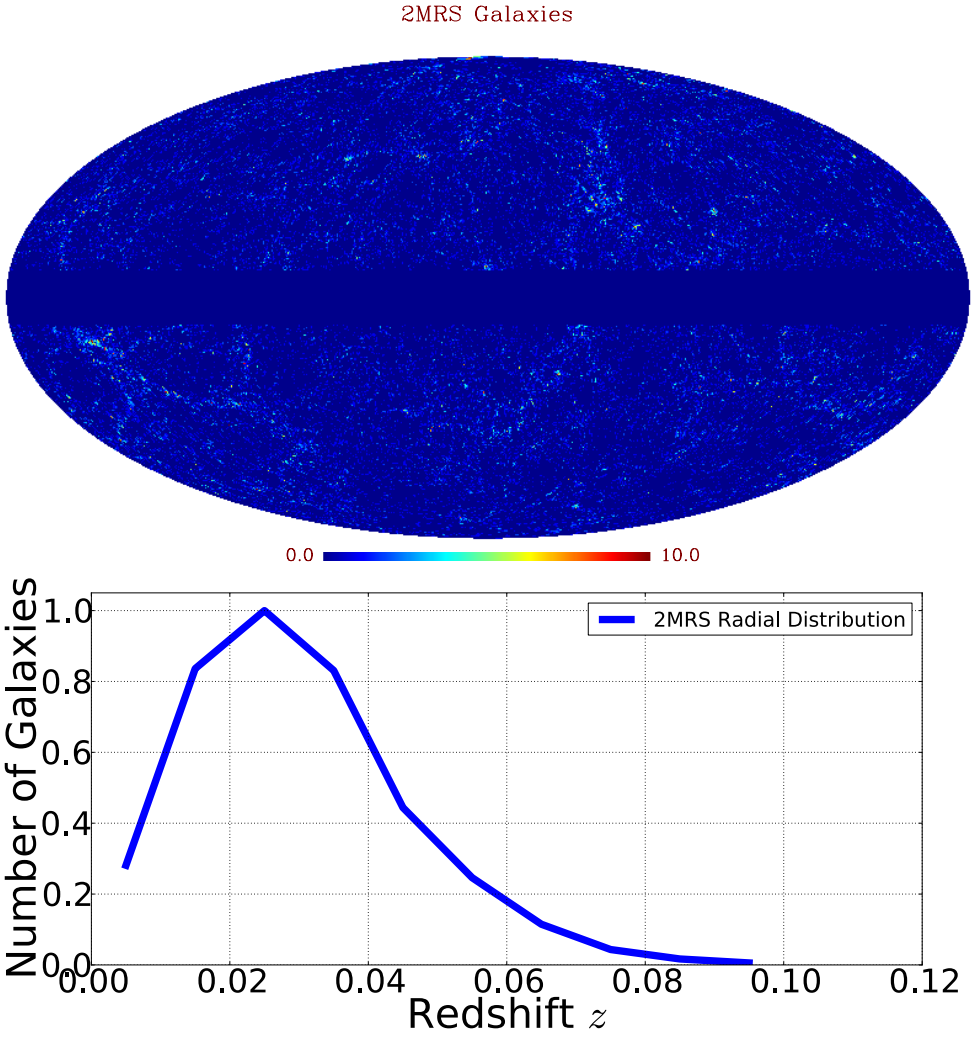

Figure 4.1: *Top:* All sources in the 2MASS Redshift Survey that escape the $|b| < 8°$ cut. The mean redshift in the survey is approximately $\bar{z} = 0.028$. Even by eye, it is clear that the dipole due to local structure has not died away at these scales. In particular, the supergalactic plane is still fairly clearly visible in the data (see, e.g., Maller et al. (2003)). (Note that the dynamic range of this plot has been limited so that structures outside the supergalactic plane are also visible.) *Bottom:* A rough plot of the radial distribution of 2MRS galaxies. The data are put in redshift bins [0, 0.01), [0.01, 0.02), ..., [0.09, 0.10), where the plot shows the number of galaxies in each bin as a function of bin center.

extinction), and we already have a sample of extragalactic sources with uniform sky coverage outside the Galactic plane. (The latter is important since a lack of uniform completeness across the sky could, if not properly accounted for, mimic the effect of a dipole.) More careful attention must be paid to these matters in the 2MASS sample as a whole, and in other surveys, but 2MRS requires only that we cut out pixels (in both the data map and the random map to which it is compared; see Chapter 3) within 8 degrees of the Galactic equator, $|b| < 8°$. This is trickier than it may at first seem, given that pixels whose *centers* are above 8 degrees, and thus escape a straightforward cut of pixels with centers below 8 degrees, still may have area below 8 degrees, especially if the pixelization is coarse, as in the cases of HEALPix (Górski et al. (2005)) NSIDE=8 or 16.[1] We adopt NSIDE=128 for the rest of this thesis, except where otherwise noted, and also cut conservatively so that pixels with any area at all with $|b| < 8°$ are cut.

4.2.1 Observational Constraints on Dipole Amplitude as a Function of Redshift

Therefore, with $|b| < 8°$ excised from the map (see Fig. 4.1), we can apply the formalism outlined in Chapter 3 directly to different subsets of the survey. We pixelize the data using HEALPix, meaning that we take the Galactic (or, in the case of the 2MASS and NVSS surveys that we analyze later in this thesis, equatorial) coordinates given in survey data and assign the given galaxy to the pixel corresponding to those coordinates. Fig. 4.2 gives the likelihood of the dipole amplitude, $\mathcal{L}(A)$, for different subsets of the entire survey, reaching out to $z_{\max} = 0.02, 0.04, 0.06, 0.08,$ and 0.10 (where the last value in that list represents the entire survey except for 25 sources at an assortment of higher redshifts).

[1] HEALPix, short for Hierarchical Equal Area isoLatitude Pixelization, is a software package for pixelizing the 2-sphere. Each pixel covers the same surface area as every other pixel, and pixel centers occur on a discrete number of rings of constant latitude. The NSIDE parameter controls the resolution of the pixelization, with the total number of pixels being equal to 12*NSIDE^2.

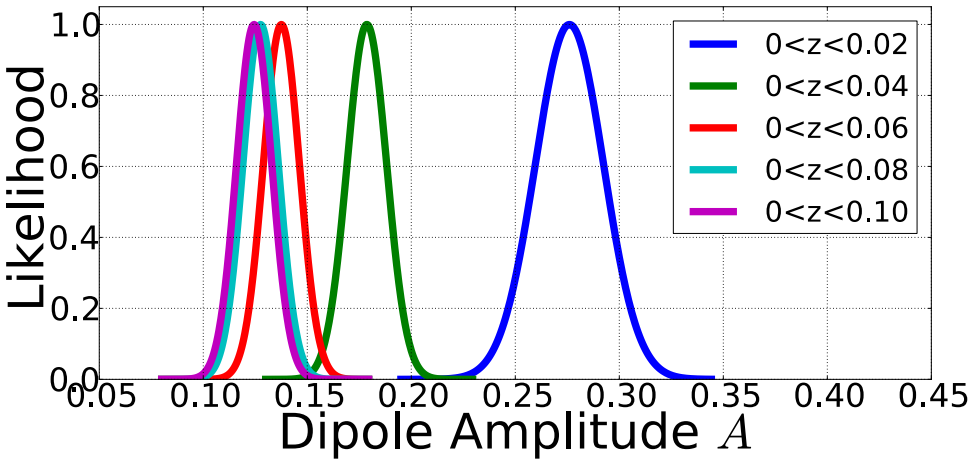

Figure 4.2: Likelihood curves for different maximum redshifts in 2MRS. Any galaxies with $|b| < 8°$ are removed from the sample, regardless of Galactic longitude l. Compare Fig. 4.5; the plot above shows how the observed dipole amplitude $A_{\rm peak}$ is found (by finding the location of the peak in likelihood) and how the corresponding measurement error bars are determined (by calculating the 68 percent confidence intervals on these likelihood curves).

Note that the behavior is as expected in several regards:

- The dipole amplitude A starts off larger and grows smaller as we go out further in redshift.
- A converges to a certain value. This should happen simply because we run out of sources as we go to higher and higher redshift (e.g., 41,446 sources are at $z < 0.06$; the total number of sources with $z < 0.10$ is 43,506.)
- Because the redshifts in this sample are relatively low in cosmological terms, going out only to $z \sim 0.10$, we expect that the dipole amplitude should remain on the order of 10^{-1}, and it does.

Although 2MRS should be relatively systematic-free, we proceed to perform straightforward tests for two types of systematic effects: Galactic extinction as characterized by the maps of Schlegel et al. (1998), and star-galaxy confusion or other systematics that vary as a function of Galactic latitude b.

4.2.2 Comparison of Dipole Parameters With and Without Extinction Template

As discussed in Chapter 3, if we wish to take Galactic extinction into account, the formalism we are employing to find dipole amplitudes and directions allows for very straightforward incorporation of the SFD maps as a systematic template. The 2MRS maps are already extinction-corrected, so this is much more of a sanity check than anything else.

The results are best presented in the form of a direct comparison, in the following table. The first column gives the Galactic latitude b of the cut; the second column identifies any systematic template present; the third gives the HEALPix NSIDE parameter; the fourth gives the number of sources that were still available after the cut was made; the fifth gives the dipole amplitude with highest likelihood; the sixth and seventh give l and b of the best-fit dipole; and the eighth and ninth give the 68 and 95 percent confidence intervals on the amplitude of the dipole. The confidence intervals are calculated by taking the likelihood distributions for the amplitude, such as those pictured in the previous plot, and adding values of A to the confidence interval until 68 (95) percent of the area under the $\mathcal{L}(A)$ curve is filled in. Entries in this table take into account the entire 2MRS sample, 43,506 galaxies (before the symmetric cut in Galactic latitude) with $0.00 < z < 0.10$.

Table 4.1: Comparison of dipole parameters with SFD template vs. without SFD template, for 2MRS.

$\lvert b\rvert \geq$	Systematics	NSIDE	N	A_{peak}	l	b	68 percent CI	95 percent CI
8.0	none	128	41834	0.1245	228.0	38.7	0.116 - 0.1325	0.108 - 0.141
8.0	SFD Dust	128	41834	0.1185	222.3	38.3	0.11 - 0.1265	0.102 - 0.135

The results change only slightly when the SFD template is added, and not in a way that is at all statistically significant, given that the 68 percent confidence intervals for dipole amplitude overlap. The fact that the dipole amplitude drops

slightly with addition of the template is an indication that a very small (and non-significant) amount of the dipole power in the 2MRS map can be attributed to the pattern set up by the distribution of dust in our Galaxy.

4.2.3 Dipole Parameters as a Function of Sky Cut

With the SFD extinction template in place, and again using the entire 2MRS sample out to $z = 0.10$, we may also vary the location where the cut in Galactic latitude is placed. Verifying that the placement of the cut (as long as it is kept at least as aggressive as the $|b| < 8^\circ$ cut) does not affect the results beyond widening our error bars serves as a check for any source of systematic error that varies as a function of Galactic latitude. Most notably, any star-galaxy confusion that might creep into the survey (very unlikely in the case of this particular survey) would vary strongly as a function of Galactic latitude, with the density of stars dropping precipitously as one moves away from the Galactic equator, and so this test serves to verify that star-galaxy confusion is not a major contributor to the detection of a dipole. It also helps to guard against the possibility that variations in sky coverage (see Sec. 4.2.8) affect the dipole signal. (Sky coverage is better at higher Galactic latitudes, since extended sources cannot be observed very close to very bright stars – less than 2 percent of the area of a typical high-latitude sky is masked by stars, as noted by Erdogdu et al. (2006).)

Note that as the sky cut becomes more and more aggressive, we expect the error bars on the observed value of A to become wider (simply because we have less data and therefore looser constraints), but we expect the best-fit/peak-likelihood value of A itself to remain consistent with values found given less aggressive sky cuts. If A shifts in such a way that more aggressive sky cuts yield amplitudes inconsistent with amplitudes from maps with less aggressive sky cuts, this is a fairly good indication

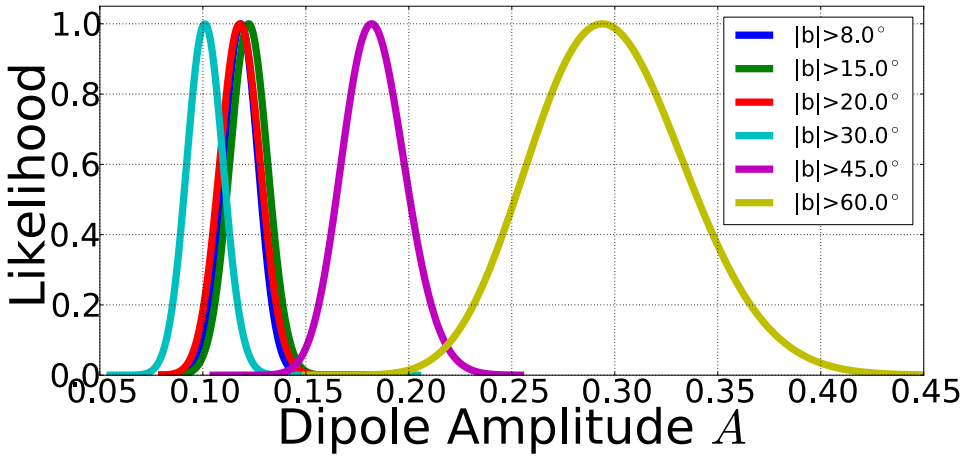

Figure 4.3: How the likelihood curves shift as we cut more and more aggressively. This is for the entire 2MRS survey out to $z_{\max} = 0.10$. Note that for the plot of theoretical and observed values of the dipole amplitude A as a function of $z_{\max}$ (see Fig. 4.5) with $f_{\rm sky} = 0.10$, the cosmic-variance band goes up to approximately $A = 0.60$, so there is nothing anomalous about having a larger value for A with very aggressive sky cuts.

that star-galaxy confusion or another systematic effect that varies with Galactic latitude is at play. Note that going out to higher redshift tends to give smaller values for A, but this is not because the *volume* is greater (otherwise, we would get larger values for A in making more aggressive angular cuts) – rather, it is because larger radial scales mean that the universe is closer to having approached homogeneity and isotropy. In other words, the angular dimensions (and thus angular cuts) are not what determine the amplitude of the dipole. However, for very aggressive cuts, we are left with far less data than we are with minimal cuts, and this means that (a) the "measurement error" on the observation becomes greater, and, even more importantly, (b) the cosmic variance associated with the theoretical prediction becomes much greater. Due to (b) in particular, a much wider range of peak-likelihood values for the amplitude becomes consistent with theory, and with the observed values from less aggressive cuts, as we cut the sky more aggressively.

Results for different sky cuts are found in Fig. 4.3. The results are all consistent

with one another given that cosmic variance comes into play. See also Table A.1 for detailed comparison of the different sky cuts.

Note that even without taking the larger cosmic variances into account, the measurements for the smaller cuts ($|b| < 30^\circ$ and below) are all consistent with one another: even the slightly anomalous $|b| < 30^\circ$ cut has a 68 percent confidence interval that very nearly overlaps with the 68 percent confidence interval for the $|b| < 8^\circ$ and $|b| < 15^\circ$ cuts. The only two of the four smallest cuts that stand in any significant tension with one another are $|b| < 15^\circ$ and $|b| < 30^\circ$, where the peak amplitude associated with the $|b| < 15^\circ$ cut lies outside the 95 percent confidence interval for the $|b| < 30^\circ$ cut, but we still have substantial overlap of 95 percent confidence intervals here, and in any case, cosmic variance has increased in the $|b| < 30^\circ$ cut to the point where it must be taken into account. The same is true for the apparent inconsistencies associated with $|b| < 45^\circ$ and $|b| < 60^\circ$: when we take cosmic variance into account, it becomes clear that there is a much wider range of acceptable values for $A_{\rm peak}$ when the sky is aggressively cut than is immediately apparent from the above table. See Fig. 4.4 for a visual representation of this, and see next section for more details about comparisons of theory with observations.

4.2.4 Dipole Amplitude, Theory vs. Observation, as a Function of Redshift

Now that we have established basic consistency among dipole determinations with different sky cuts (with the proviso that the most aggressive cuts are reconciled within cosmic-variance limits, as explained further in this section), we go back to the least restrictive cut, at $|b| < 8^\circ$, and keep the SFD template in place. We proceed to compare theory and observation in dipole amplitude as a function of redshift in 2MRS.

In calculating theoretical values, it is important to note (again; this was also noted

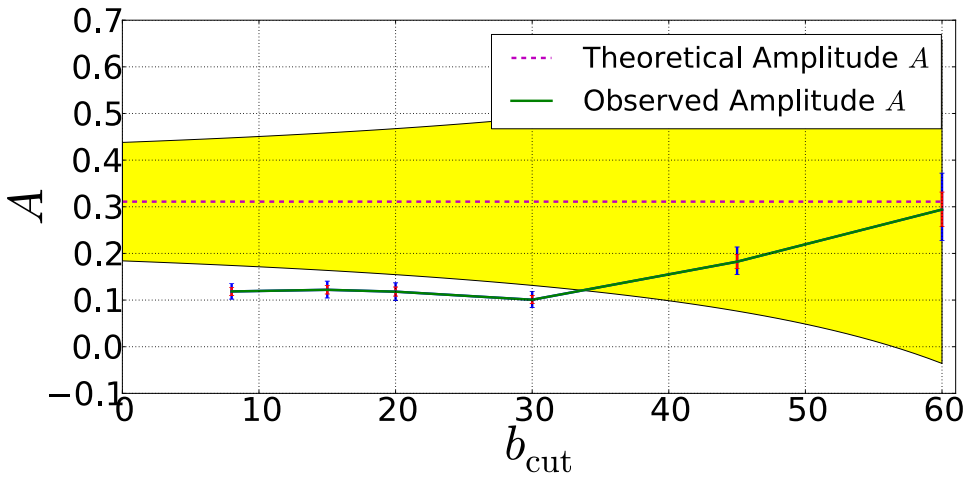

Figure 4.4: Results for the dipole amplitude as a function of cut in Galactic latitude b. Here $b_{\rm cut}$ indicates that $|b| < b_{\rm cut}$ was cut out of the map. Notice the very wide cosmic-variance band (yellow shaded region) around the theoretically predicted value for the dipole amplitude, and the consistency of all observed values within cosmic-variance limits. The small error bars indicate measurement errors: red represents a 68 percent confidence interval; blue represents a 95 percent confidence interval. These errors are tiny in comparison with cosmic variance.

in Chapter 3) that bias must be included in theoretical predictions in order for these predictions to be directly comparable to observational results. Frith et al. (2005a), in a paper on the power spectrum of 2MASS, find the bias in the 2MASS K_s band to be 1.39 ± 0.12, employing a technique that uses constraints on the galaxy power-spectrum normalization as well as previous constraints on σ_8. We therefore adopt 1.4 as the value of the bias for both 2MRS and 2MASS in general. The qualitative conclusions of the rest of this chapter do not depend strongly on the precise value adopted for the bias. (Note that, for constant bias b, dipole amplitude $A \propto b$.)

There are cosmic-variance errors on all theoretical predictions:

$$\delta C_\ell = \sqrt{\frac{2}{(2\ell+1)f_{\rm sky}}} C_\ell. \tag{4.1}$$

We can relate C_ℓ to the amplitude A via

$$C_1 = \frac{4\pi}{9} A^2 \tag{4.2}$$

and so doing error propagation to get the cosmic-variance error on the amplitude,

we have

$$\delta A = \frac{1}{2}\sqrt{\frac{2}{3f_{\rm sky}}}A. \tag{4.3}$$

This allows us to plot cosmic-variance uncertainties in both C_1 and A. The basic result of doing so is shown in Fig. 4.5. Note that the errors on the observations are very small in comparison with cosmic variance. Therefore, for the rest of this section, we consider measurement errors negligible and focus only on how observational results compare with theory within the bounds of cosmic variance.

The dipole amplitude, both theory and measurement, decreases as redshift increases, exactly as it should given our previous arguments that averaging over more structure at larger distances yields lower values of the dipole. Whether the amplitude is expressed as A or as C_1, the observational results are consistently lower than the theoretical expectations. If these measurements for different $z_{\rm max}$ were all independent, there would be a highly significant inconsistency between theory and observation, but the measured values are highly correlated since samples with higher $z_{\rm max}$ contain all samples with lower $z_{\rm max}$.

More specifically, correlations between a bin i going out to $z_{\rm max,1}$ and another bin j going out to $z_{\rm max,2}$ are calculated as

$$\mathrm{Cov}\left[C_{ii}, C_{jj}\right] = \frac{2}{2l+1}C_{ij}^2, \tag{4.4}$$

where C_{ij} is proportional to $[W_i(z)W_j(z)]$ ($W(z)$ is the weight function for each population) and similarly for C_{ii} and C_{jj}. Then the correlation coefficient is

$$\rho = \mathrm{Cov}(C_{ii}, C_{jj})/\sqrt{\mathrm{Cov}(C_{ii}, C_{ii})\mathrm{Cov}(C_{jj}, C_{jj})} = C_{ij}^2/(C_{ii}C_{jj}) \tag{4.5}$$

Correlations between 2MRS samples range from 0.422 (between the full ($0.00 < z < 0.10$) sample and the smallest ($0.00 < z < 0.01$) sample), to 0.805 (between the

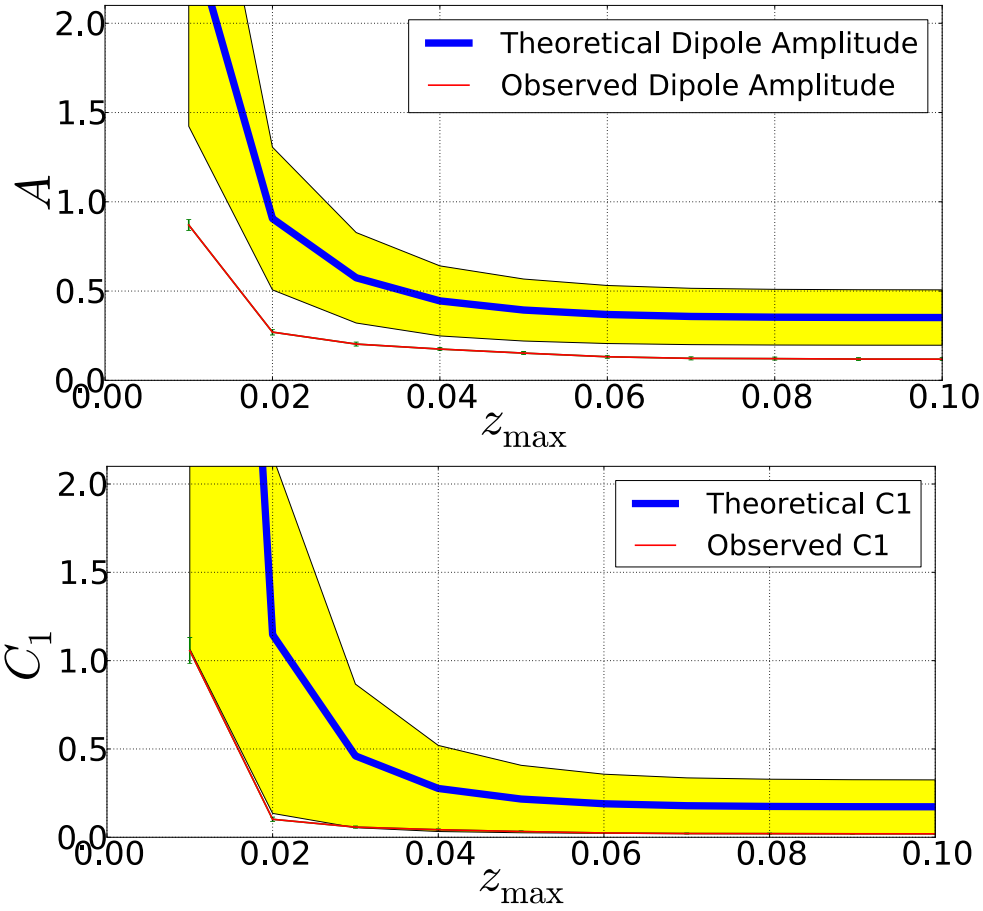

Figure 4.5: *Top:* Comparison of observations with theory for the dipole amplitude, as a function of how much of the 2MRS sample is included ($0.00 < z < z_{\max}$). All observed values are found including the SFD template, and with a cut at $|b| < 8°$. For the purposes of calculating theoretical predictions, we take $f_{\rm sky} = 0.8568$. (This value is calculated by noting that we have removed all pixels with any area at all below the $|b| < 8°$ cut.) *Bottom:* The same results, only with the dipole power C_1 rather than dipole amplitude A. See Chapter 3 for details of the procedure to convert between A and C_1.

full sample and the second-smallest ($0.00 < z < 0.02$) sample), to well over 0.99 for many combinations of samples. (This is also the reason why all bins have similar significance as compared with one another.) Therefore, rather than being a 10-sigma inconsistency between theory and observation, Fig. 4.5 represents only slightly more than a 1-sigma discrepancy. The next section will find the precise "discrepancy" rigorously.

4.2.5 Stricter Comparison of Theory and Observation for Dipole Amplitude

Given a Gaussian field on the celestial sphere with observed angular power spectrum $C_\ell^{\rm obs}$, the power is χ^2-distributed, and the likelihood of a given theoretical value $C_\ell^{\rm th}$ is

$$\ln P(C_\ell^{\rm th}|C_\ell^{\rm obs}) = \sum_{\ell=0}^{\infty} \frac{2\ell+1}{2}\left[-\frac{C_\ell^{\rm obs}}{C_\ell^{\rm th}} + \ln\frac{C_\ell^{\rm obs}}{C_\ell^{\rm th}}\right] - \ln C_\ell^{\rm obs}. \tag{4.6}$$

(see, for example, Chu et al. (2005)).[2] Here the observed quantity $C_\ell^{\rm obs}$ is treated as a realization of the theoretical value $C_\ell^{\rm th}$. For $\ell = 1$, this simplifies to

$$\ln P(C_1^{\rm th}|C_1^{\rm obs}) = \frac{3}{2}\left[-\frac{C_1^{\rm obs}}{C_1^{\rm th}} + \ln\frac{C_1^{\rm obs}}{C_1^{\rm th}}\right] - \ln C_1^{\rm obs} \tag{4.7}$$

Again, we treat this as a likelihood, so that P is a function of the theoretical model $C_1^{\rm th}$, with the observed quantity held fixed. Then, as usual, we can plot the likelihood of a parameter value (in this case, theoretical $C_1^{\rm th}$) and see where our "actual" theoretical $C_1^{\rm th}$ falls with respect to that distribution. In each redshift bin, we could generate a different likelihood distribution based on the observation, and then compare to the actual $C_1^{\rm th}$ in each case. However, because of the very high correlations between redshift samples, we gain very little by doing tomography in this way, and

[2] This expression can be derived by noting that the random variable $Y = (2\ell+1)\frac{C_\ell^{\rm obs}}{C_\ell^{\rm th}}$ is χ^2-distributed with $2\ell+1$ degrees of freedom. Inserting this expression for Y into the general expression for a χ^2 distribution, and then using the fact that $P(Y)dY = P(C_\ell)dC_\ell$, it is relatively straightforward to show that the proportionality for $P(C_\ell)$ given in Chu et al. (2005) holds, and from there the expression for the log-likelihood given above immediately follows.

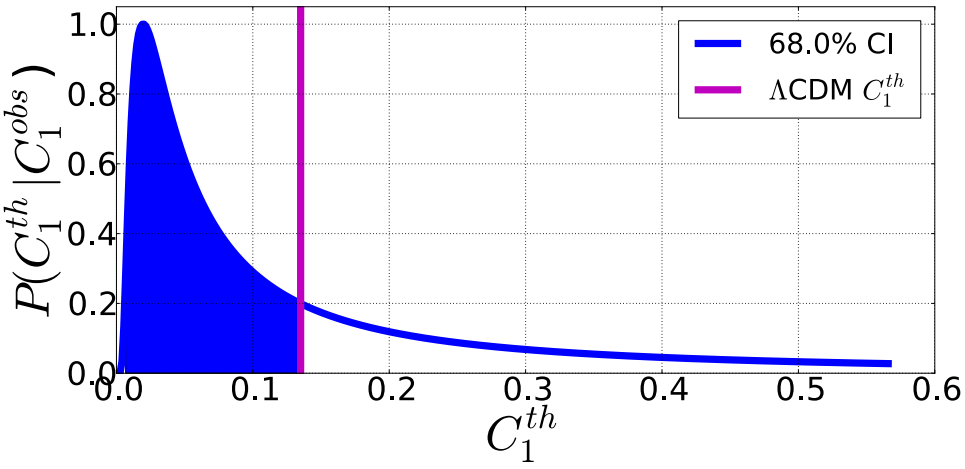

Figure 4.6: Posterior probability of theoretical C_1 given observed C_1 as a function of the theoretical value, for the full sample of 2MRS galaxies. The observed C_1 determines the likelihood distribution for $C_1^{\rm th}$, and we can then compare the ΛCDM value (vertical magenta line) for $C_1^{\rm th}$ to that distribution. The ΛCDM value is not an outlier in the theoretical distribution, and hence we say that theory matches observation here.

so we only perform this analysis on the full 2MRS sample, $0.00 < z < 0.10$. The results are shown in Fig. 4.6.

Whether we calculate a simple signal/noise ratio to compute the significance of $C_1^{\rm th}$ results given $C_1^{\rm obs}$, as in Fig. 4.5, or whether we use the more sophisticated (and correct) comparison of Fig. 4.6, the qualitative conclusion is the same: the ΛCDM prediction matches observations within appropriate cosmic-variance limits. Note that the reason why these two strategies do not match up quantitatively is that the signal/noise strategy assumes cosmic variance is symmetric, while using the $P(C_1^{\rm th}|C_1^{\rm obs})$ distribution takes into account the asymmetry of cosmic variance, particularly at the very low ℓ at which we are working. This is also why significances in C_1 and A do not match up with one another exactly.

4.2.6 Observational Constraints on Dipole Direction as a Function of Redshift and Sky Cut

Up to this point, we have been focusing on the dipole amplitude and comparing theoretical and observed amplitudes. The direction of the dipole, however, is also a quantity of considerable interest.

As discussed in Chapter 2, there are three major types of dipoles that could contribute to any detected dipole in objects that trace large-scale structure: the local-structure dipole, the kinematic dipole, and the intrinsic dipole. At the scales probed by 2MRS, we expect the local-structure dipole to completely dominate other contributions, since it is on the order of 10^{-1} while the kinematic dipole falls two orders of magnitude below this and the intrinsic dipole may very well fall even further below that. Therefore, there is no reason to expect that the direction of the 2MRS dipole should align with the direction of the CMB dipole, as we would expect it to do if the kinematic dipole were dominant at these scales.

That said, it should not be at all surprising if the 2MRS local-structure dipole points somewhere near the CMB kinematic dipole. The reason for this has to do with what generates the motion that gives rise to the kinematic dipole. As discussed in Chapter 2, the total velocity of the Sun with respect to the Local Group is directed along almost the same line as the velocity of the Local Group with respect to the CMB rest frame, but in the opposite direction. So the direction of the Sun's total motion with respect to the CMB rest frame is essentially the same as the direction of the Local Group's motion with respect to the CMB rest frame, but the speed is lower than that of the Local Group since the contribution of the Sun's motion with respect to the Local Group gets subtracted off. The Local Group moves in a certain direction with respect to the CMB rest frame because of the gravitational pull of structure in

the relatively nearby universe. The acceleration due to gravity of the Local Group, as determined via flux-weighted dipole measurements, is directed less than 10° away on the sky from the direction of the velocity of the Local Group (Maller et al. (2003)). Therefore, insofar as the local-structure dipole gives information about the clustering of local structure and the direction of the acceleration due to gravity of the Local Group, it is expected that it should point in at least the same general direction as the CMB kinematic dipole, which is generated in part by the velocity of the Local Group induced by its acceleration due to gravity. Since the local-structure dipole is a 2D-projected quantity rather than one that preserves radial information, it is not a perfect indicator of where gravitational pulls on the Local Group are coming from. But we do expect the direction of the local-structure dipole to feel some influence from the direction of the CMB kinematic dipole.

The observational results for the direction of the dipole are displayed in Fig. 4.7. The results align with the qualitative expectations detailed above. It turns out that the 2MRS dipole direction is indeed not consistent with the direction of the CMB kinematic dipole, but still within the same basic region of sky.

Note that the constraints on the dipole direction are actually tighter for the very small $0.00 < z < 0.01$ sample than for the full sample of 2MRS galaxies, despite the fact that the number of sources is an order of magnitude smaller. This is not anomalous since the higher-redshift sources actually decrease the prominence of the dipole in local structure, producing a result with roughly half the total signal/noise as in the case where we take the $z_{\max} = 0.01$ subsample.

The best-fit direction for the 2MRS dipole is $(l, b) = (228.0°, 38.7°)$. Erdogdu et al. (2006) find that the 2MRS number-weighted dipole (the quantity they analyze that is "closest" to our dipole) is at $(l, b) = (218°, 33°)$ in the CMB frame, in close

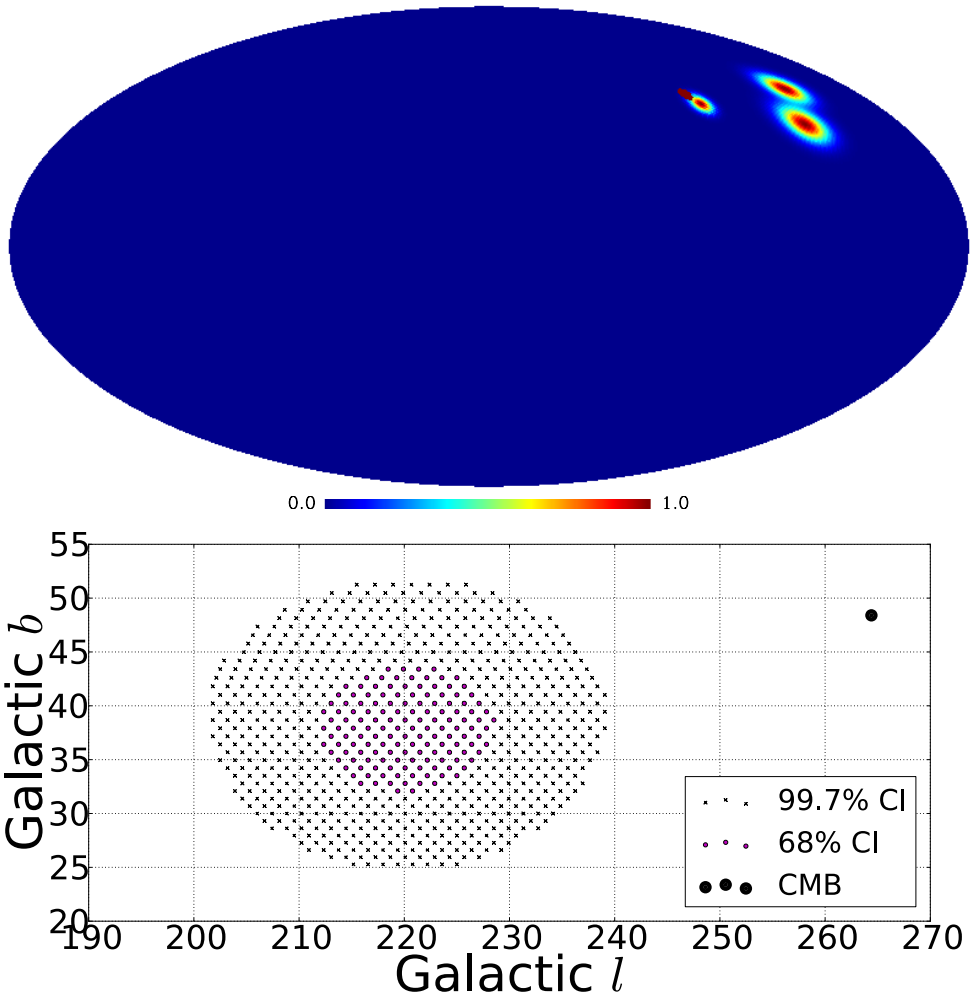

Figure 4.7: *Top:* Likelihood as a function of direction, marginalizing over amplitude. This plot shows the likelihood constraints on the dipole for 2MRS redshift shells $0.00 < z < 0.01$ (leftmost multicolored oval), $0.00 < z < 0.03$ (uppermost multicolored oval), and $0.00 < z < 0.10$ (rightmost multicolored oval), all with NSIDE=128 and a cut for $|b| < 8°$, with the SFD dust systematic template incorporated. The color scale represents normalized likelihood as a function of direction. The single-colored disc that overlaps with one of the multicolored likelihood ovals represents the direction of the CMB kinematic dipole, with error bars exaggerated to a circle of 2 degrees in order to make the position clearly visible on the map. *Bottom:* Confidence intervals for the direction of the dipole in the full 2MRS survey (using NSIDE=64), with the position of the CMB dipole shown. Agreement was not expected, but it is reassuring that the 2MRS projected dipole does lie in the same general region of sky as the CMB dipole.

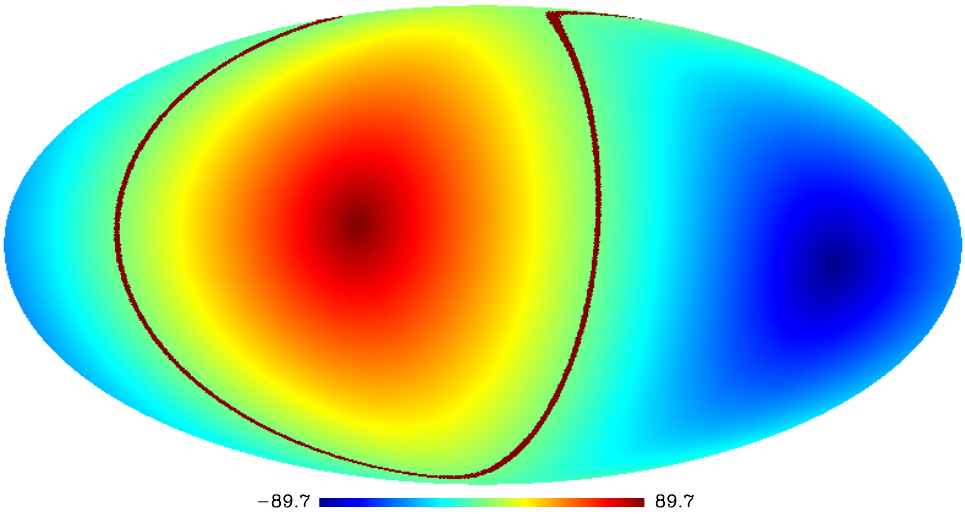

Figure 4.8: This map, a projection in Galactic coordinates, shows supergalactic latitude SGB in its color-coding. The dark red strip corresponds to the region within 1 degree of the supergalactic equator.

agreement with our results.

4.2.7 Cutting the Supergalactic Plane

As a final check, we wish to know how much of the dipole signal in 2MRS is coming from the vicinity of the supergalactic plane (SGP), a planar structure in the local galaxy distribution (Lahav et al. (2000)). We therefore progressively excise more and more of the SGP and see how much the amplitude of the dipole dies away. We compare this to the effect of excising *similar areas* from the vicinity of the supergalactic poles. We expect that there should be more sources near the supergalactic plane, and that the dipole should die away much more quickly when the supergalactic plane is excised than when similar areas around the supergalactic poles are excised. Supergalactic coordinates SGB and SGL are defined in analogy to Galactic b and l, where SGL is the azimuthal coordinate, and SGB=0 corresponds to the middle of the supergalactic plane, so we care only about making cuts in SGB.

This check will become more important as we proceed to perform our analysis on

surveys that probe much larger radial distances than does 2MRS, as the structure associated with the supergalactic plane will only contribute to the dipole on relatively nearby scales, and the effect should diminish as we probe to larger and larger redshifts.

In table form, we find the results in Table A.2 when we use the usual $|b| < 8°$ Galactic cut and also include a cut around the supergalactic plane (first part of the table, with |SGB| $\geq$ in the first column) or a cut around the supergalactic poles (second part of the table, with |SGB| $<$ in the first column). The second column, $f_{\rm sky}$, gives the fraction of the sky that remains when we perform the given cut.

Abstracting the key results, we now directly compare cuts around the supergalactic plane with cuts of similar area around the supergalactic poles. We calculate $f_{\rm sources}$, the fraction of the total number N of sources that remain when we perform the given cut. The cuts in SGB (less than 2.0, 5.0, 10.0, 20.0; greater than 74.82, 65.90, 55.73, 41.15) were chosen so that equal areas around the plane and around the poles would be cut if there were no cut in Galactic b (as in our tests on the BATSE catalog; see Chapter 5). Since there is a cut in Galactic latitude here, $f_{\rm sky}$ does not match up exactly between the cuts around the supergalactic plane and poles, but the values are still close, and in any case they are normalized in the $f_{\rm sources}/f_{\rm sky}$ calculation; we employ the same cuts for all surveys tested in this thesis.

Table 4.2: Key patterns in cutting in supergalactic coordinates, for 2MRS.

|SGB| $\geq$	$f_{\rm sky}$	N	$f_{\rm sources}$	$\frac{f_{\rm sources}}{f_{\rm sky}}$	$A_{\rm peak}$	|SGB| $<$	$f_{\rm sky}$	N	$f_{\rm sources}$	$\frac{f_{\rm sources}}{f_{\rm sky}}$	$A_{\rm peak}$
0.0	0.86	41834	1.00	1.17	0.12						
2.0	0.82	39964	0.96	1.16	0.11	74.82	0.84	41234	0.99	1.17	0.12
5.0	0.78	37124	0.89	1.14	0.11	65.90	0.81	39867	0.95	1.18	0.12
10.0	0.70	32673	0.78	1.11	0.10	55.73	0.74	36882	0.88	1.20	0.12
20.0	0.55	24799	0.59	1.08	0.08	41.15	0.59	30321	0.72	1.22	0.14

Note the following, referring to Table 4.2:

- The fraction of sources associated with the supergalactic plane is greater than the fraction of sources associated with the supergalactic poles for every $f_{\rm sky}$. This is our first indication that a greater-than-random portion of the dipole signal comes from the vicinity of the supergalactic plane.

- The ratio $f_{\rm sources}/f_{\rm sky}$, which gives a measure of how overdense the uncut portion of the sky is, dwindles steadily as we cut more and more of the SGP, but increases as we cut more and more area around the supergalactic poles. Therefore, as expected, there are more sources near the supergalactic plane than near the supergalactic poles, and this is true essentially regardless of how much of the area around the plane/poles is cut.

- The dipole amplitude steadily dies away as we cut more and more of the area around the supergalactic plane, but it does not do so as we cut equivalent area around the supergalactic poles. This is another indication that the dipole signal comes preferentially from the vicinity of the SGP.

- The dipole amplitude actually becomes higher when we remove most of the sky that is more than 20 degrees away from the supergalactic plane (the cut which removes all but $|\mathrm{SGB}| < 41.15°$). This makes sense given that we have removed much of the structure that smooths out the dipole and left only the structure near the supergalactic plane that contributes strongly to the dipole.

In general, we conclude that more of the dipole signal comes from the area of the supergalactic plane than from the vicinity of the supergalactic poles. This serves as a good check that the source of the dipole signal in the relatively local structure surveyed by 2MRS is generally where we expect it to be. When we perform analyses of higher-redshift objects in Chapter 5, the supergalactic plane should not "show up"

as it has here.

4.2.8 2MRS: Conclusion

We conclude our analysis of the dipole signal in 2MRS by pointing out that all results are consonant with theoretical expectations. This comes as no surprise given that 2MRS was the most well-controlled and well-understood of the surveys we analyze here, and was being treated exhaustively as something of a model for our other analyses.

It should also be noted that we have verified that the results above do not change appreciably when corrections are made for the 2MASS coverage map (see Sec. 4.3).

We now proceed to apply our dipole analysis to the full 2MASS dataset.

4.3 Dipole in 2MASS

We now analyze the full 2MASS survey in a manner similar to how we analyzed the very well-characterized 2MRS subsample. The challenges associated with analyzing 2MASS as a whole are greater, in part because the full sample of 2MASS galaxies (1.6 million extended sources) does not have uniform completeness across the entire sampled sky. To remove this problem, we must make judicious cuts based on the photometry.

As shown in Fig. 4.9, the biggest issue in connection with survey completeness is that the selection function has a sharp discontinuity for galaxies with K_s-band magnitude greater than roughly 13.5. We therefore cut out all these sources, roughly 2/3 of the sample, at the outset, and consider only that portion of the survey with nearly uniform completeness over the entire sky (with the exception of the Galactic plane), that is, sources with $K_s < 13.5$.

Second, we excise the Galactic plane as we did for 2MRS, but must make a more

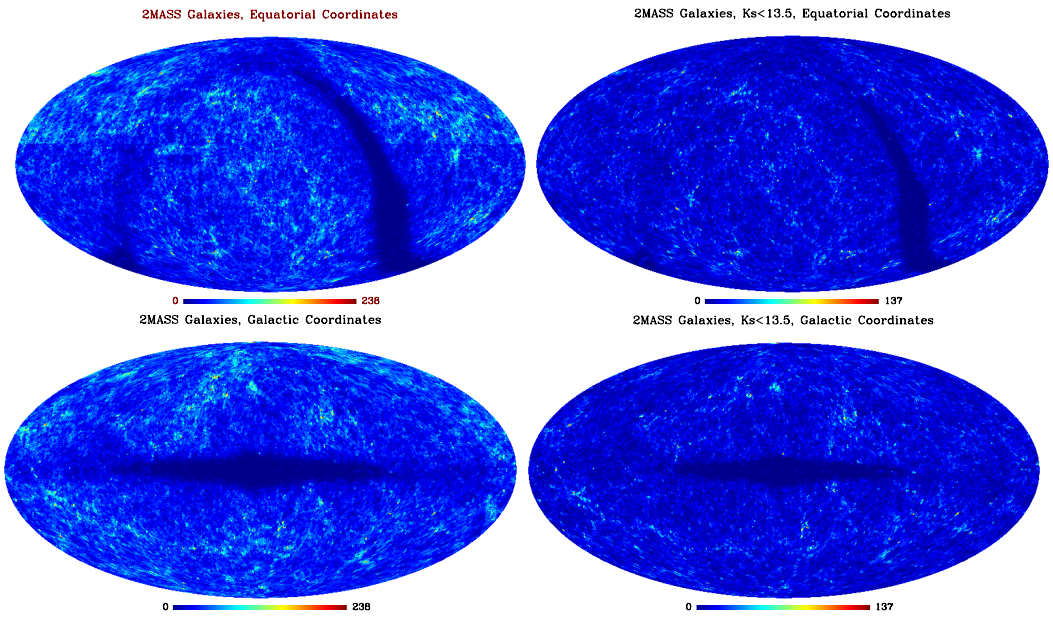

Figure 4.9: *Left side:* All 2MASS sources, in equatorial and Galactic coordinates. Note the very strong discontinuity in the selection function, visible in both images (especially in the top image, where it appears as a horizontal line), at declination around 20 degrees. *Right side:* 2MASS sources with K_s-band magnitude less than 13.5 (with limited dynamic range in the Galactic-coordinates plot to bring out structure more clearly). The survey has nearly uniform completeness when this criterion is imposed.

aggressive cut in order to ensure that star-galaxy confusion does not come into play. Maller et al. (2005), in a paper that computes the galaxy angular correlation function and three-dimensional power spectrum of 2MASS, as well as Skrutskie et al. (2006) in the main paper profiling 2MASS, note that the 2MASS XSC is highly reliable and complete for $|b| > 20°$ (more than 98 percent galaxies rather than stars at these latitudes), but that star-galaxy confusion is an increasingly large problem at lower latitudes: the XSC is 10 percent stars for $5° < |b| < 20°$; and within the Galactic plane, $|b| < 5°$, there is additional contamination by artifacts (10 to 20 percent) and Galactic extended sources (~ 40 percent) including globular clusters, open clusters, planetary nebulae, and giant molecular clouds (Jarrett et al. (2000b)). In particular, Maller et al. cross-correlate the 2MASS stellar density $n_{\rm star}$ with the XSC galaxy density as a function of the latitude of a symmetric (in Galactic coordinates) cut and

find that including XSC objects with $|b| < 15^\circ$ gives a galaxy-star cross-correlation that is higher in amplitude than the galaxy-galaxy autocorrelation, suggesting the presence of multiple-star systems mistakenly identified as extended sources. However, this excess signal goes away for a cut of $|b| < 20^\circ$. Cutting at $|b| < 20^\circ$ ensures less than 2 percent contamination from Galactic sources (Maller et al. (2005)). Frith et al. (2005a) likewise find that a cut of $|b| < 20^\circ$ is satisfactory.

Third, we use the XSC confusion flag (`cc_flg`) to eliminate known artifacts (diffraction spikes, meteor streaks, infrared airglow, etc.).

Fourth, again following Frith et al. (2005a), as well as Maller et al. (2005), we also cut out bright ($K_s < 12.0$) objects with $(J - K_s)$ colors that are outside the range $[0.7, 1.4]$. This is a conservative measure designed to get rid of a final set of objects which are in the 2MASS XSC but which are not extragalactic sources. This removes a few thousand sources.

Fifth, as explained later, we take the 2MASS sky coverage into account. The XSC does not have completely uniform sky coverage given the presence of bright stars and other foreground objects that make it more difficult for the telescopes to detect extended sources in particular directions, and so although this the pattern of sky coverage is highly parity-even (following the shape of the Galaxy) and unlikely to mimic a dipole in any way (part of why it made no difference to the 2MRS results), we still take this into account in the present analysis.

Sixth and finally, K-corrections (corrections to magnitudes in a given passband that are made necessary by the fact that light can redshift into or out of a given range of wavelengths) for the K_s band can make a non-negligible difference in the calculation of a flux-weighted dipole or other quantity that depends on specifics of photometry. However, in this case we do not need to take them into account, because

they are actually accounted for in our predictions: K-corrections are tied to the same (pseudo-)Doppler effect that helps to generate the kinematic dipole (see Chapter 2), and so accounting for them in observational results as well would amount to double-counting.

All photometric cuts are applied to 2MASS isophotal magnitudes – not total magnitudes, which are an extrapolated quantity and viewed as less reliable for the purposes of this kind of analysis. While many analyses which use 2MASS data actually use the extrapolated magnitudes (since, according to Jarrett et al. (2003), the isophotal magnitudes underestimate total luminosity by 10 percent for early-type and 20 percent for late-type galaxies), we stick here with the more conservative isophotal magnitudes, especially since the cut at $K_s < 13.5$ is much surer to accomplish its purpose if the more conservative magnitude estimates are used. It is worth noting that the 2MRS team used isophotal magnitudes in their sample selection (Huchra et al. (2011)).

With these photometric cuts applied, we are ready to proceed with the analysis. While no spectroscopic redshifts are available for the 2MASS XSC as a whole, and the photometric redshifts that do exist are not particularly reliable, considerable information is available about the overall radial distribution of 2MASS galaxies. In particular, Frith et al. (2005a) and others give the 2MASS radial selection function as

$$n(z) = \frac{3z^2}{2(\bar{z}/1.412)^3} \exp\left(-\left(\frac{1.412z}{\bar{z}}\right)^{3/2}\right) \tag{4.8}$$

with $\bar{z} = 0.074$ for $K_s < 13.5$ and $\bar{z} = 0.050$ for $K_s < 12.5$. With these values of $\bar{z}$, we can determine theoretical predictions for the local-structure dipole (which is still dominant by two orders of magnitude over other contributions to the dipole at these scales) for these two photometric cuts. Combined with the 2MRS sample,

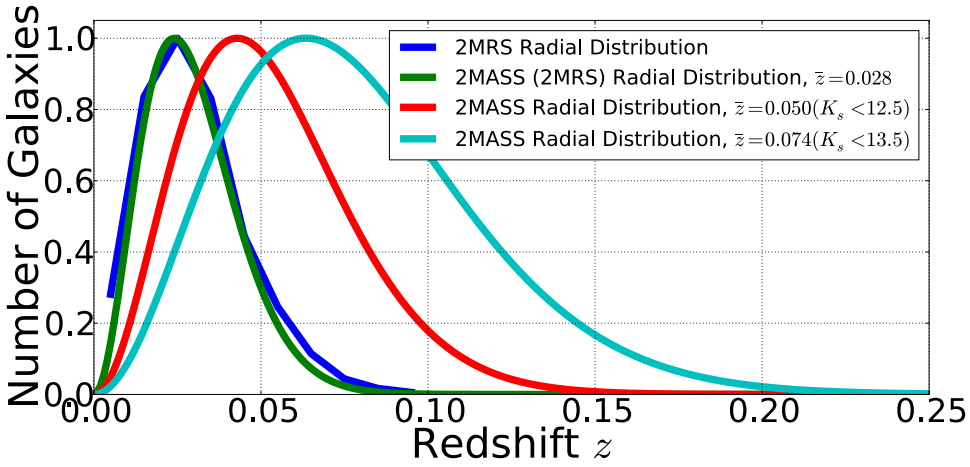

Figure 4.10: Plot of the radial distribution of 2MASS galaxies as a function of redshift. Three different mean redshifts are shown, one which corresponds to the 2MRS distribution (the actual 2MRS $n(z)$ is plotted in blue), and the other two of which correspond to photometric cuts in the full 2MASS survey of $K_s < 12.5$ and $K_s < 13.5$.

which follows this same form for the selection function quite closely (see Fig. 4.10) and corresponds to approximately $\bar{z} = 0.028$, we can perform a comparison of theory and observation for multiple subsamples of the entire 2MASS catalog.

The total number of galaxies in the 2MRS catalog for $z < 0.1$ is 43,506. For $K_s < 12.5$, there are 127,030 galaxies, or 89,980 if we cut $|b| < 20°$. For $K_s < 13.5$, there are 542,201 galaxies, or 381,586 for $|b| < 20°$.

It should be noted that some previous results concerning the 2MASS galaxy distribution stand in some tension with ΛCDM predictions. For example, Frith et al. (2005b) point out that the angular correlation function and angular power spectrum of 2MASS galaxies (under cuts reasonably similar to the ones we perform here) display fluctuations that are 3-5 sigma out of line with ΛCDM predictions. We focus attention here on the dipole alone, which of course sacrifices a certain amount of information with respect to what could be gained from analysis of the entire power spectrum, but also lends itself to much better and more detailed analysis of contributions to the signal at this one multipole.

4.3.1 Systematic Checks: Extinction and Sky Coverage

In 2MRS, extinction corrections were already applied to the magnitudes of the galaxies, but in 2MASS, the catalog values for the magnitudes are not corrected for extinction. This means that it becomes much more important in this case to make sure that we have adequately controlled for the effects of extinction. Of course, once we have a sample of objects to which to apply the dipole-detecting formalism, magnitudes do not matter, but magnitudes do matter in determining which objects get into the sample in the first place. We find that several thousand galaxies that do not make the $K_s < 13.5$ cut before extinction correction do make the cut when magnitudes are corrected for extinction. (Note that extinction corrections always bring magnitudes down, since sources appear dimmer due to extinction, and so are assigned higher brightness/lower magnitude when corrected for extinction.)

We have performed various extinction corrections, experimenting with slightly different extinction coefficients for the 2MASS K_s band (0.367 from Ho et al. (2008); 0.302 from the analogous UKIRT value in Schlafly and Finkbeiner (2010); cf. 0.35, which is used by Erdogdu et al. (2006), following Cardelli et al. (1989)). We find that the results when extinction corrections are applied directly are essentially identical to the results obtained when the SFD dust systematic template is applied as it was to the 2MRS maps, so we explicitly present only the SFD-template results here.

Table 4.3 compares the no-template vs. template cases for $K_s < 13.5$ and for $K_s < 12.5$. As should be clearly visible from a quick glance at the values in the table, very little changes when the SFD template is included, and there is substantial overlap even of the 68 percent confidence intervals for each of the no-template cases with each of the corresponding SFD-template cases. We conclude that although the results shift slightly, and therefore it is worth keeping the SFD template in our

Table 4.3: Comparison of dipole parameters with SFD template vs. without SFD template, for 2MASS, for two different limiting K-band magnitudes.

For objects with $K_s < 13.5$:								
$\|b\| \geq$	Template	NSIDE	N	$A_{\rm peak}$	l	b	68 percent CI	95 percent CI
20.0	none	128	386008	0.0890	303.4	7.3	0.086 - 0.0922	0.0828 - 0.0952
20.0	SFD	128	386008	0.0882	305.0	4.5	0.085 - 0.0912	0.082 - 0.0944
For objects with $K_s < 12.5$:								
$\|b\| \geq$	Template	NSIDE	N	$A_{\rm peak}$	l	b	68 percent CI	95 percent CI
20.0	none	128	91008	0.0848	275.0	28.2	0.0785 - 0.0908	0.0725 - 0.0968
20.0	SFD	128	91008	0.0812	276.3	25.9	0.0752 - 0.0875	0.0692 - 0.0935

analysis, extinction does not have a substantial impact on the dipole results. This is as expected based on considerations of how extinction affects 2MASS coverage, as outlined in Jarrett et al. (2000a) and Jarrett et al. (2000b).

Coverage Maps

Uniform completeness in an infrared survey like 2MASS is impossible due to the presence of foreground stars. In some directions, the presence of foreground stars makes observation of distant background galaxies impossible. Sky coverage, which ranges from 0 to 1 within a given pixel, tends to be well above 0.98 for the high-Galactic-latitude sky. Data products from 2MASS include coverage maps (see http://www.ipac.caltech.edu/2mass/releases/allsky/doc/sec2_6f.html) that indicate coverage as a function of direction.

We convert these maps into the same HEALPix pixelization scheme we use to pixelize all the surveys in this thesis, including 2MASS itself. Each HEALPix pixel contains at least 4, and up to 19, "subpixels" associated with the pixelization of the coverage maps on the 2MASS site, so resolution is not an issue. See Fig. 4.11.

There are several ways in which we could take these coverage maps into account in our analysis. First, we could mask out all HEALPix pixels that have an average

coverage less than some threshold (the threshold is usually chosen as 0.98 in the literature; see, e.g., Ho et al. (2008)). Second, we could mask out all pixels that have *any* subpixel with coverage less than some threshold. Third, we could use the entire coverage map as a systematic template. We have not found a case in which it makes anything even close to a statistically significant difference which of these strategies we choose, so we choose the option that is simplest and arguably best: we use the entire coverage map as a systematic template. This has the advantage of not privileging any particular threshold, but rather taking the variation in coverage over the entire sky into account evenhandedly. This accounts for the actual pattern of observations on the sky and weights them accordingly (cf. our treatment of the BATSE exposure function in Chapter 5). In any case, given that the coverage map closely follows the shape of the Galaxy (foreground stars are, after all, our primary concern), and the Galaxy is nearly parity-even, we do not expect coverage to contribute significantly to the (parity-odd) dipole anyway; results are very much in accord with these expectations.

The results in this section do not change appreciably when the coverage map is applied as a template.

4.3.2 Systematic Checks: Sky Cut and Supergalactic Plane

We perform the same cuts in Galactic latitude as we did for 2MRS, but with the expectation that the most reliable results will come for the $|b| < 20^\circ$ cut rather than $|b| < 8^\circ$ as in the case of 2MRS. See Tables A.3 and A.4. See Fig. 4.12 for a visual capture of the results in these tables, with cosmic variance on the theoretical prediction taken into account.

The basic conclusion here, as in the case of 2MRS, is that in no case are results very far outside of the limits expected given cosmic variance. It is somewhat interesting

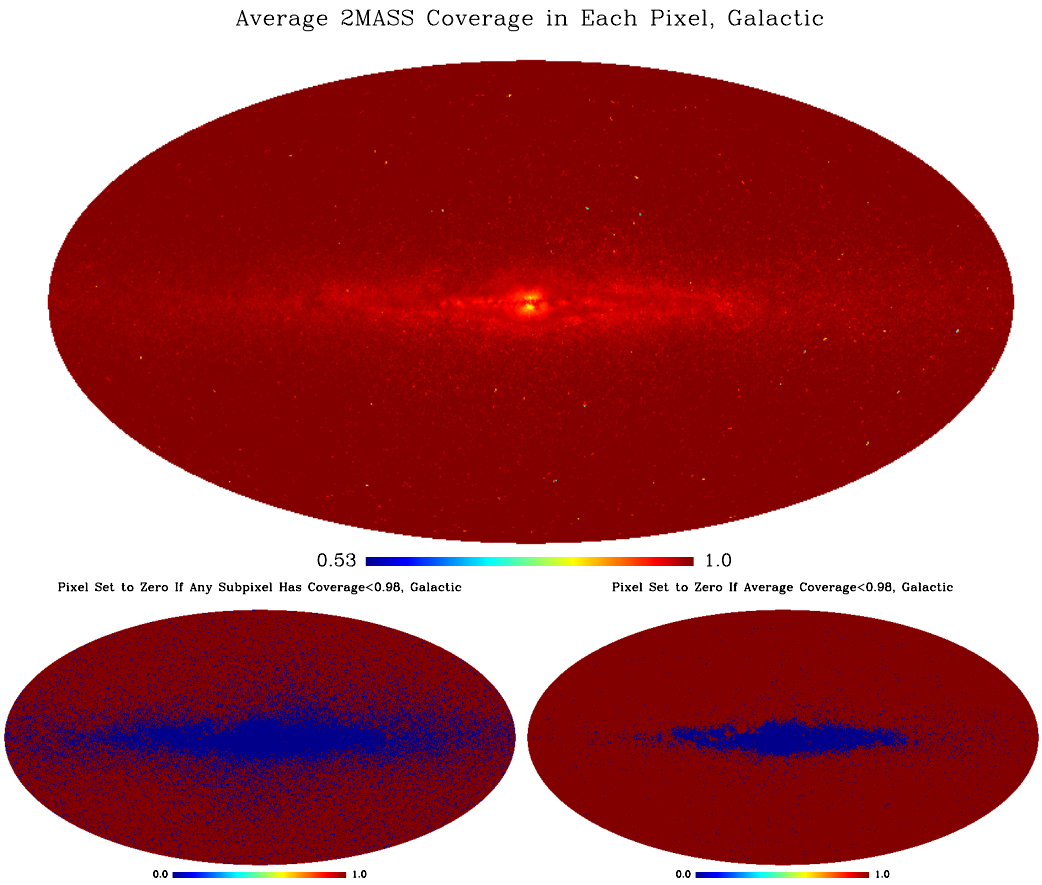

Figure 4.11: Maps of sky coverage in 2MASS. (1) Sky coverage as a function of direction for the entire sky, in HEALPix pixelization, NSIDE=128. We use this map as a systematic template in the dipole formalism. (2) In this map, pixels are set to zero when *any subpixel* has coverage less than 0.98 (pessimistic case). Pixels are set to one otherwise. (3) In this map, pixels are set to zero when the *average* coverage in the pixel is less than 0.98 (optimistic case). Pixels are set to one otherwise.

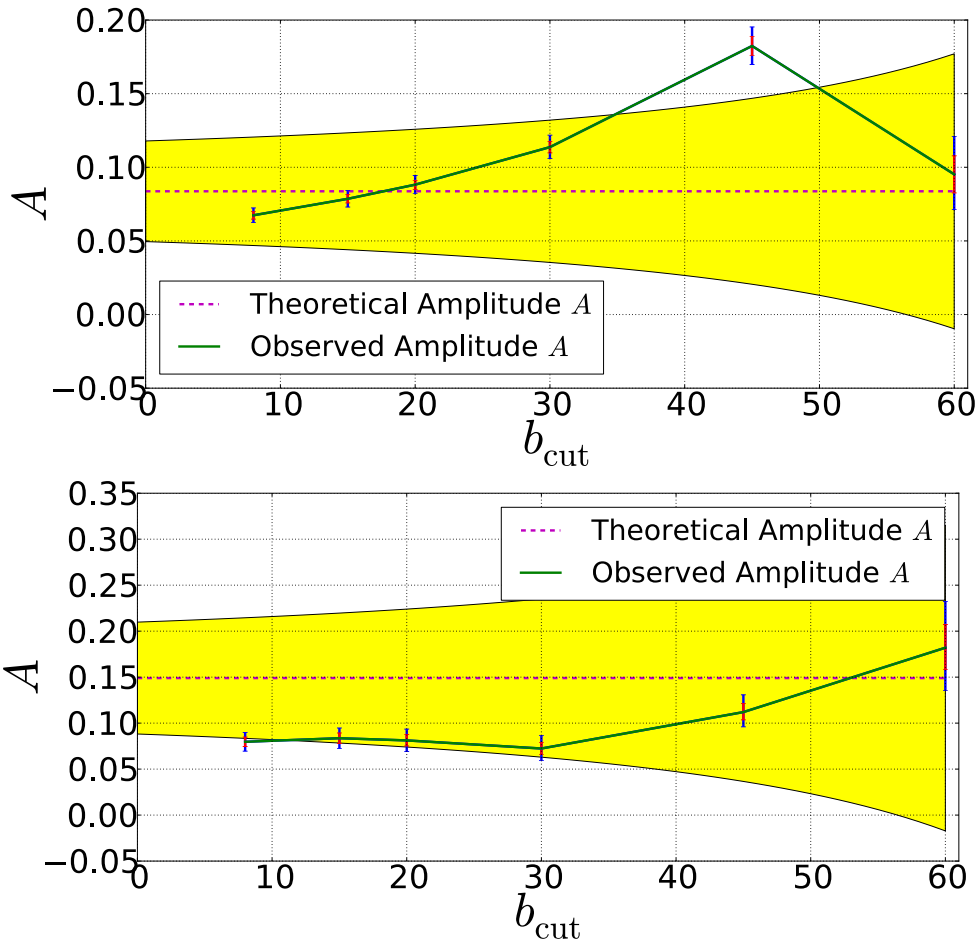

Figure 4.12: *Top:* 2MASS sources with $K_s < 13.5$, dipole amplitude as a function of $b_{\rm cut}$. *Bottom:* 2MASS sources with $K_s < 12.5$, dipole amplitude as a function of $b_{\rm cut}$. See Fig. 4.4 for a fuller discussion of the significance of this type of plot.

that the 2MASS $K_s < 13.5$ case, the largest and therefore (we would predict) best-constrained subset of the 2MASS survey to which we apply our dipole analysis, displays a pattern unlike that of the 2MRS and 2MASS $K_s < 12.5$ subsets, where instead of giving the largest value for the amplitude in the case of the most aggressive cut, the largest value of A comes with the $|b| < 45°$ cut. However, this is still not anomalous, and in fact cosmic variance is still sufficiently large at these scales that it would have been very surprising had there been a genuine anomaly. In any case, there is not a strong enough dependence on cut to indicate any serious contamination from star-galaxy confusion or other systematic effects that vary with Galactic latitude, so we follow Skrutskie et al. (2006), Frith et al. (2005a), and others in taking $|b| < 20°$ as our fiducial cut.

We also perform the same test as in the 2MRS case where we cut in supergalactic latitude SGB. For $K_s < 13.5$, the full results are presented in Table A.5. Meanwhile, for our much smaller sample of brighter 2MASS sources, $K_s < 12.5$, we end up with the results presented in Table A.6. We create summary tables giving the key patterns, as we did for 2MRS in Table 4.2. Results are presented for $K_s < 13.5$ and $K_s < 12.5$ in Table 4.4.

There are certain trends worth noting in these results:

- The observations that we made for 2MRS again (generally) hold here: in particular, $f_{\rm sources}/f_{\rm sky}$ decreases monotonically as more and more of the supergalactic plane is excised, and the ratio increases (almost) monotonically as more and more of the area around the supergalactic poles is excised.

- We will see in Sec. 4.3.4 that the direction of the dipole seems (at first glance) to be anomalous in the $K_s < 13.5$ fiducial case since there is a strong mismatch with the 2MRS and $K_s < 12.5$ cases, but note that the best-fit dipole direction

Table 4.4: Comparison of dipole parameters when performing various cuts in supergalactic coordinates, for 2MASS, for two different limiting K-band magnitudes.

For objects with $K_s < 13.5$:											
$\lvert SGB\rvert \geq$	$f_{\rm sky}$	N	$f_{\rm sources}$	$\frac{f_{\rm sources}}{f_{\rm sky}}$	$A_{\rm peak}$	$\lvert SGB\rvert <$	$f_{\rm sky}$	N	$f_{\rm sources}$	$\frac{f_{\rm sources}}{f_{\rm sky}}$	$A_{\rm peak}$
0.0	0.65	386008	1.00	1.53	0.09						
2.0	0.63	368077	0.95	1.52	0.08	74.82	0.65	385740	1.00	1.53	0.09
5.0	0.59	342390	0.89	1.51	0.07	65.90	0.64	378368	0.98	1.53	0.09
10.0	0.52	301028	0.78	1.50	0.06	55.73	0.60	355464	0.92	1.53	0.09
20.0	0.39	225502	0.58	1.49	0.05	41.15	0.49	295090	0.76	1.55	0.09
For objects with $K_s < 12.5$:											
$\lvert SGB\rvert \geq$	$f_{\rm sky}$	N	$f_{\rm sources}$	$\frac{f_{\rm sources}}{f_{\rm sky}}$	$A_{\rm peak}$	$\lvert SGB\rvert <$	$f_{\rm sky}$	N	$f_{\rm sources}$	$\frac{f_{\rm sources}}{f_{\rm sky}}$	$A_{\rm peak}$
0.0	0.65	91008	1.00	1.53	0.08						
2.0	0.63	86657	0.95	1.52	0.07	74.82	0.65	90951	1.00	1.53	0.08
5.0	0.59	80177	0.88	1.50	0.05	65.90	0.64	89203	0.98	1.53	0.08
10.0	0.52	70212	0.77	1.48	0.05	55.73	0.60	83805	0.92	1.53	0.08
20.0	0.39	52528	0.58	1.48	0.04	41.15	0.49	69923	0.77	1.55	0.08

monotonically decreases in l and increases in b as more and more of the supergalactic plane is cut, bringing the $K_s < 13.5$ result into greater alignment with the other results. This will be discussed further in Sec. 4.3.4.

4.3.3 Dipole Amplitude as a Function of Redshift/Photometric Cuts

Taking as most reliable the case with a cut for $|b| < 20°$, and keeping the SFD template in place, we proceed to compare theoretical predictions with observational results for the dipole amplitude for the two different magnitude cuts we have used, $K_s < 13.5$ and $K_s < 12.5$, which correspond to $\bar{z} = 0.074$ and 0.050, respectively. Again, the 2MRS sample corresponds to $\bar{z} = 0.028$, and we include this data point in our comparisons as well.

See Fig. 4.13 for results. Note that measurement errors are once again tiny in comparison with cosmic-variance errors.

The magnitude of the dipole in 2MASS has, of course, been calculated previously

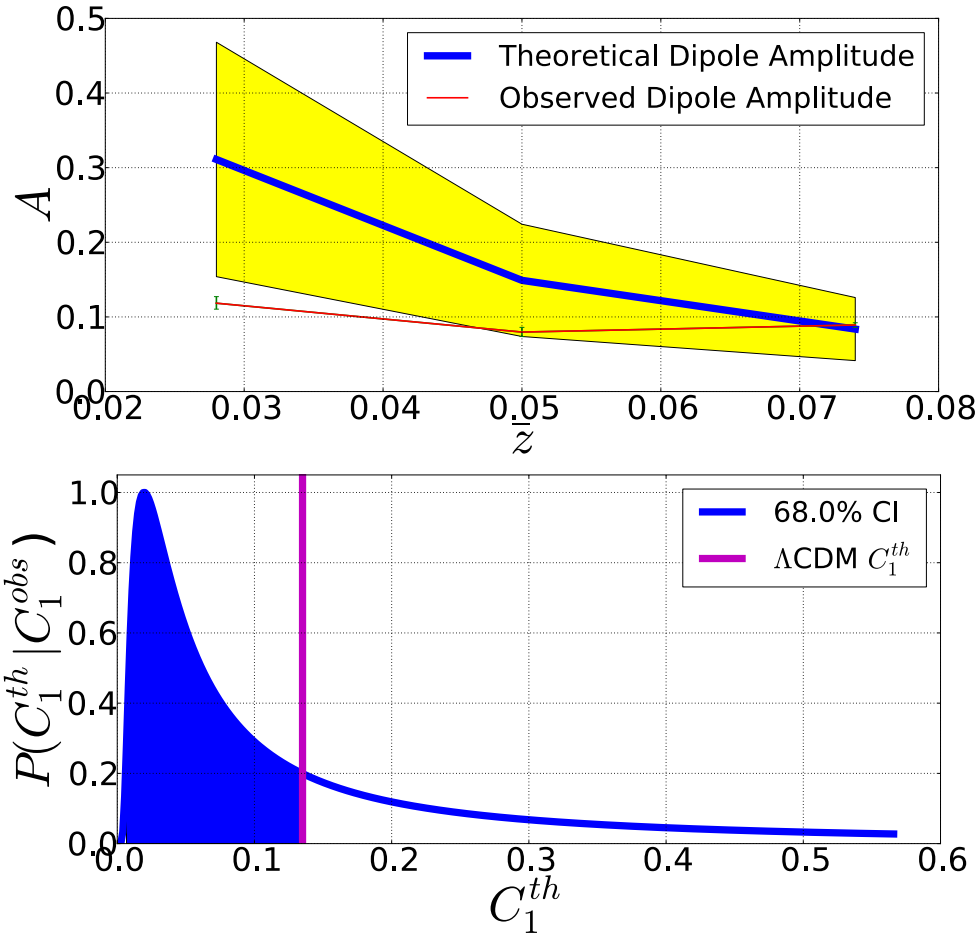

Figure 4.13: *Top:* Results for the dipole amplitude in the 2MASS survey, as a function of mean redshift $\bar{z}$ of the galaxy sample. The lowest-$\bar{z}$ sample corresponds to the 2MRS galaxies with $|b| < 8°$ cut out; the middle sample to $K_s < 12.5$ with $|b| < 20°$ cut out in the 2MASS XSC; the highest-$\bar{z}$ sample to $K_s < 13.5$ with $|b| < 20°$ again cut out in the 2MASS XSC. Cosmic variance is shown in the most pessimistic $|b| < 20°$ case for *all* of the samples. *Bottom:* We again compare the ΛCDM value for $C_1^{\rm th}$ with the expected distribution of $C_1^{\rm th}$ given the observed value, in this case for the $K_s < 12.5$ sample. Regardless of which way we compare measurements with theory, we have demonstrated sound agreement between theory and observation for all three subsamples of 2MASS.

as part of computations of the entire power spectrum. In particular, Frith et al. (2005a) give $C_1 \approx 0.004$ for both $K_s < 13.5$ and $K_s < 12.5$. This value converts to $A \approx 0.054$; cf. our values of $A = 0.088 \pm 0.003$ and $A = 0.081 \pm 0.006$ (68 percent confidence) for $K_s < 13.5$ and $K_s < 12.5$. While the Frith et al. value would be just as unremarkable as ours in comparisons with theory (both our value and Frith et al.'s are within the two-sigma cosmic-variance error bars), the discrepancy in observational results is noteworthy. The Frith, Outram, and Shanks result is based on a harmonic-space estimator applied to all ℓ. Given that our estimator for the dipole amplitude is in real space and provides a very natural way to account for both sky cut and systematic effects, we put considerable faith in the result given here.

4.3.4 Dipole Direction as a Function of Redshift/Photometric Cuts

In Fig. 4.14, we present the results for the dipole direction in both the $K_s < 13.5$ and more conservative $K_s < 12.5$ cases. Once again, dipole amplitudes are on the order 10^{-1} while the kinematic dipole is expected to be on the order 10^{-3}, so no particular agreement with the direction of the CMB dipole is expected. We do expect the $K_s < 12.5$ sample to give a direction relatively close to that of the 2MRS dipole, given the overlap in the samples, and $K_s < 13.5$ to give a result close to $K_s < 12.5$. In fact, we would regard it as anomalous if the results were not all consistent with one another, *if* the samples were genuinely sampling the same population – larger samples would simply have smaller error bars than smaller samples. However, the populations being sampled are different, given that the structure associated with $\bar{z} = 0.028, 0.050$, and 0.074 are quite distinct from one another. So even internal inconsistencies (between different values of $\bar{z}$) are tolerable, though still in need of some explanation.

We find in practice that the direction of the $K_s < 13.5$ dipole is actually quite

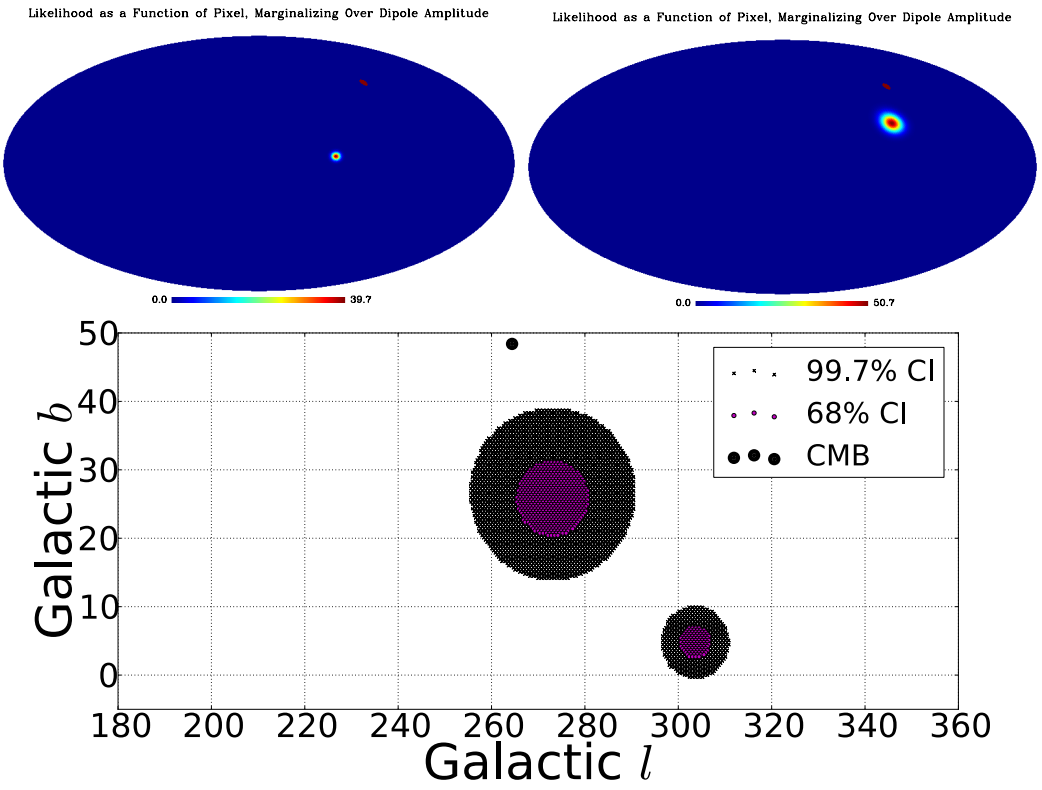

Figure 4.14: (1)Results for the dipole direction for the 2MASS XSC, $K_s < 13.5$, with a cut eliminating $|b| < 20°$, and applying the SFD map as a systematic template. (2) The same, but with $K_s < 12.5$. (3) Confidence intervals to go with (1) and (2), with the CMB kinematic dipole direction indicated.

substantially ($> 3\sigma$) inconsistent with the direction of the $K_s < 12.5$ dipole. One possible explanation involves extinction corrections: if we do not extinction-correct the magnitudes in the 2MASS XSC, we preferentially throw away galaxies near the Galactic plane, since those are the ones that would more easily make the cuts (because they are actually intrinsically brighter than they appear given the presence of dust) if we were to extinction-correct. However, we find, as discussed in Sec. 4.3.1, that explicitly extinction-correcting the magnitudes has the same effect as applying the SFD template to the uncorrected magnitudes: that is, it changes the direction very little, and in fact pulls both the $K_s < 13.5$ and $K_s < 12.5$ results slightly higher in l and slightly lower in b, though these changes are unimportant.

A better explanation is the straightforward conclusion that the $K_s < 13.5$ and $K_s < 12.5$ samples really are sampling substantially different populations, even though the latter is a (small; roughly 1/5 the size) subset of the former. This is confirmed in the patterns observed in the previous section where we progressively excise the supergalactic plane and poles. As more and more of the SGP is excised in the $K_s < 13.5$ sample, the best-fit l decreases and the best-fit b increases, moving closer to the $K_s < 12.5$ full-sample l and b. This is a good indication that $K_s < 13.5$ simply picks up more and different structure associated with the SGP than does the $K_s < 12.5$ sample.

4.4 Conclusions From Subsets of 2MASS

We draw the basic conclusion that there are no anomalous results in applying tests of dipole amplitude and direction to subsets of the 2MASS dataset and comparing these results with theoretical predictions.

CHAPTER V

Dipoles in BATSE/CGRO and NVSS

We now proceed to more critical tests using higher-redshift objects that might begin to probe the kinematic dipole, as these objects exist at scales on which the local-structure dipole should have become comparable to, or even smaller than, the kinematic dipole.

5.1 Introduction

We begin this chapter by considering surveys that detect very high-energy photons (X-ray and gamma-ray), and then address the opposite end of the spectrum (radio) in the second half of the chapter.

First, a brief note on X-ray data. Flux-weighted dipoles have been previously calculated using the soft X-ray band (< 2 keV) data from ROSAT and the hard X-ray (2-10 keV) background data as observed by HEAO1-A2. For example, Plionis and Georgantopoulos (1999) use the 1.5 keV (~ 0.8 nm) ROSAT All-Sky Survey (RASS) data to calculate a flux-weighted dipole, and Scharf et al. (2000) perform a similar analysis on HEAO1-A2. Contamination is a major issue for both analyses. At the time of publication of these studies, only roughly three-quarters of the unresolved X-ray flux in the soft and hard bands had been accounted for (by extrapolation of objects resolved in deep fields) (Scharf et al. (2000)), and theoretical modeling

of populations contributing to the unresolved flux (AGNs, starburst galaxies, hot IGM in rich clusters, etc.) remained difficult. In the case of hard X-rays, Scharf et al. argue that at least a third of the structure in the data may be Galactic in origin (associated especially with the bulge), and soft X-rays are even more strongly contaminated by Galactic emission. Treyer et al. (1998) point out that in the soft band, Galactic emission is present as a contaminant at all scales; the hard band is better, but Treyer et al. still rely on the Galactic hard-band emission model of Iwan et al. (1982) to predict that for Galactic latitude $> 20°$, the variations in flux due to Galactic emission are less than 3 percent.

All told, it is very difficult to remove the foreground in X-ray all-sky surveys successfully without some relatively uncertain modeling, without fairly serious suspicion of contamination, and without removing a good deal of the background too (especially in the soft band; Plionis and Georgantopoulos (1999) estimate that Virgo contributes as much as 20 percent to the dipole amplitude in RASS). Theoretical predictions would also be difficult to make without a well-understood redshift distribution, especially given that the populations contributing to the X-ray background are not especially well-modeled. Hence we stay away from attempting to perform X-ray analyses here.

Some authors have searched for a dipole in the XRB to the extent that it is possible to do so. The results that Scharf et al. find in hard X-rays for the flux-weighted dipole basically align with theoretical predictions of what they refer to as the Compton-Getting effect (another name for the kinematic dipole, following a paper by Compton and Getting (1935) on the effect on cosmic-ray intensity of Earth's motion through the Milky Way). More recently, Boughn et al. (2002) analyzed the same (HEAO1-A2) dataset and found a limit (95 percent confidence) on the ampli-

tude of any intrinsic dipole at 5×10^{-3}. However, given the difficulty of definitively separating extragalactic from foreground/Galactic emission in this dataset, and other problems already noted, significant uncertainty attends any analysis in X-rays, so we note all these results without making heavy use of them in the remainder of this thesis. Similarly, other populations of objects detected at the very high-energy end of the spectrum, including blazars and clusters of galaxies detected with gamma-ray satellites (see, e.g., Ando et al. (2007)), may be good targets for dipole searches in the long term, especially once their bias is better-understood and future surveys provide better statistics for the given target population; but we do not pursue those here.

For analysis of a 2D-projected dipole (i.e., not flux-weighted; see Chapter 2) in very high-energy surveys, we turn instead to gamma-ray bursts. GRBs are the most powerful explosions known in the universe, though their exact nature and progenitor objects remain under some debate, and their redshifts are difficult to measure since GRB observations are not well-localized (see Fig. 5.1) and redshifts can only be measured from their afterglows, which must be matched up with the position of the original GRB, a highly nontrivial task given the error bars on the position of a typical GRB. A review of previous research on the dipole in the GRB distribution, as well as presentation of results using the formalism outlined in Chapter 3 and applied to the BATSE catalog, is presented in Sec. 5.2.

In Sec. 5.3, we move to the low-frequency end of the spectrum and present results from the NRAO VLA Sky Survey (NVSS), a radio survey with nearly 1.8 million extragalactic sources (Condon et al. (1998)). This survey presents an excellent opportunity to actually test for the presence of the kinematic dipole and possibly the intrinsic dipole in large-scale structure. NVSS has more potentially non-negligible systematics to control for than the other surveys we use, but it also has higher

potential payoff because of its combination of depth and sky coverage.

5.2 Dipole in BATSE

5.2.1 Previous Work on the Isotropy of GRBs

Up through the mid-1990s, there was a long history of assessing the isotropy of GRBs in an attempt to infer whether they were cosmological or Galactic sources (or a combination thereof). For example, Maoz (1993) argued in 1993 that gamma-ray bursts could be shown to exist in an extended Galactic halo, some 130-270 kpc away from Earth, by detecting slight but well-defined deviations from spherical symmetry predicted for such a halo population. While his analysis did indeed suggest that GRBs were nearby intergalactic objects, he argued that comparison with more specific models would be necessary before considering the case closed.

In a similar spirit, Briggs et al. (1995) argued persuasively that the population of GRBs could not be Galactic, based on their observed isotropy. This study found that the Galactic dipole and quadrupole moments (calculated very straightforwardly as $\langle \cos\theta \rangle$ and $\left\langle \sin^2 b - 1/3 \right\rangle$) did not differ significantly from those predicted for an isotropic distribution. The majority of GRB models that assumed GRBs are a Galactic population were found to be in $> 2\sigma$ tension with the detected dipole and quadrupole moments, and hence the conclusion of this research was that GRBs are more isotropic than observed Galactic populations, suggesting either a nearby intergalactic or, more likely, cosmological source.

Scharf et al. (1995) compute a fluence-weighted dipole (where fluence is flux integrated over the timespan of the burst) in analogy to the flux-weighted dipoles discussed in previous chapters of this thesis. Combining fluence-weighted dipole information with straightforward 2D-projected dipole measurements (i.e., including photon count information) better distinguishes a velocity dipole (due, as usual, to the

Doppler effect and relativistic aberration) from other possible sources of anisotropy. This kind of test is supplementary to the tests we perform here.

The current consensus that GRBs are cosmological is based not only on the considerations discussed above and the absence of even a weak band corresponding to the Milky Way in the GRB distribution (Tegmark et al. (1995)), but also (and especially) on the observation of optical, X-ray, and radio counterparts to GRBs that are clearly extragalactic (e.g., Paciesas et al. (1999); van Paradijs et al. (1997); Fruchter et al. (1999); Metzger et al. (1997)). Given the extragalactic origins of GRBs, we can understand the dipole that should exist in GRBs as being due to the same effects that give rise to a dipole in other sources we have analyzed. As far back as the mid-1990s, Maoz (1994) predicted the dipole in the clustering of GRBs, combining the effects of relativistic aberration and the Doppler effect. These estimates are somewhat uncertain, but we too are unsure how precisely GRBs trace large-scale structure (e.g., if they can be described as a single population with a single bias, and so forth). Maoz finds that the amplitude of this (kinematic) dipole is of order $A \sim 10^{-2}$ (to within uncertainties of a factor of two), which is still an order of magnitude larger than the CMB dipole, but much closer than the sources we dealt with in the previous chapter. Maoz estimated that a large (of order 10^4) sample of GRBs would be necessary to detect the predicted dipole, and given that current catalogs offer only on the order of 10^3 bursts, we do not expect an unequivocal detection. That said, we nevertheless run our tests, given that useful constraints can be placed on the maximum possible dipole amplitude even if we cannot confidently detect a dipole in currently available GRB catalogs. We will discuss Maoz's estimates further when we discuss observational results in Sec. 5.2.

We perform our tests on GRBs in the BATSE catalog, data taken by the Compton

Gamma-Ray Observatory. The BATSE (Burst and Transient Source Experiment) instrument onboard CGRO detected gamma-ray bursts within the nominal range of 50 to 300 keV. Other GRB datasets are available, including those from SWIFT and Fermi (known previously as GLAST), but we use the BATSE catalog because it has the most sources for an all-sky survey.

The most recent published catalog of GRBs from BATSE is the 4B catalog, which has 1637 sources and includes all confirmed GRBs from the start of the mission through August 1996. There is also a "current" catalog with over 2700 sources, but this is unpublished and subject to change. In the 4B catalog, there are several complicating details that are worth noting in regard to what bursts make it into the catalog and which do not.

BATSE employed scintillators sensitive to gamma rays from $\sim$ 25 to 2000 keV. A burst triggered the instrument when gamma-ray count rates exceeded some minimum threshold relative to background in two or more of the eight detector modules, within some energy range (Paciesas et al. (1999)). Nominally, that energy range was 50-300 keV, but on the order of 30 percent of BATSE's observing time was spent with one of several trigger energy ranges different from this. In addition, while the minimum detection threshold in count rates relative to background was 5.5 sigma as a baseline, this value also changed many times over the course of the experiment, and was not always the same for different time intervals (BATSE tested count rates at 64, 256, and 1024 ms intervals).

A different trigger energy range essentially represents a distinct burst experiment, and a different detection threshold also changes the parameters of the experiment in an important way. However, we argue that the time variation in BATSE's ability to detect gamma-ray bursts is not sufficiently great to affect our results on the dipole,

especially given the lack of statistics for the BATSE sample of 1637 bursts. Kommers et al. (1997) performed a search for gamma-ray bursts and other gamma-ray transient phenomena with peak fluxes below (by a factor of ~ 2) the flux necessary to count as a detection, and also with energies outside the nominal 50-300 keV. They found that the direction and intensity distributions of 91 likely GRB candidates *not* included in the final BATSE catalog imply that biases associated with the trigger mechanism do not significantly affect the completeness of the catalog. In addition to this result, there is no reason to expect that changes in experimental parameters would have a particular effect on the dipole quantity we investigate here. We note especially that changing trigger criteria and energy ranges do not appreciably increase the chances that GRBs will be confused with Galactic sources (e.g., soft gamma repeaters (SGRs)), so contamination remains minimal; and any changes in trigger criteria apply uniformly over the entire sky, so there is no obvious reason why this would induce a dipole pattern. We therefore proceed to analyze the full catalog without accounting for these changes.

However, one other experimental parameter is important for our dipole analysis: sky exposure in BATSE varies as a function of declination (BATSE spent different amounts of time looking at different declinations). We create a template out of the exposure function (see Fig. 5.1) and use this template as one of the systematic templates t_i in the dipole formalism outlined in Chapter 3. This corresponds to weighting pixels according to how much time the satellite spent observing a given area of the sky: compare, for example, Scharf et al. (1995). The choices we make here, to ignore changes in trigger criteria but take the exposure function into account, corresponds to the choices made in the paper by Tegmark et al. (1995) calculating the angular power spectrum of the BATSE 3B catalog, which found no evidence of

deviations from isotropy on any angular scale. Our present tests can be regarded as updates (since we use the 4B catalog, which contains > 500 more bursts than the 3B) of Tegmark's, with focus on the dipole using a better estimator that more naturally incorporates sky cuts and systematic templates. (Note that Tegmark et al. also impose a weighted averaging scheme in harmonic space to account for the very large position errors associated with GRBs (on the order of degrees, orders of magnitude larger than typical position errors associated with galaxies). This is unnecessary in our case given that the dipole probes scales much larger than the uncertainties in GRB positions.)

The redshift selection function for GRBs is still only poorly understood, though better statistics are consistently being built up. GRBs come from even higher redshifts on average than NVSS sources (see Sec. 5.3) (e.g., Xiao and Schaefer (2009)), however, so we can confidently say that regardless of the precise distribution, the local-structure dipole will be subdominant in comparison with the kinematic dipole (given that it is already subdominant for NVSS sources), and so we consider only the kinematic dipole as a theoretical expectation below.

5.2.2 Systematic Checks and Dipole Amplitude

The positions of GRBs detected by BATSE are shown in Fig. 5.1. Again, they are not very well-localized; the positions typically have error bars on the order of degrees. The GRBs do not appear to cluster in any particular way by eye, but we apply our usual tests to see whether this holds up rigorously.

In considering what systematic templates to put in place, maps of Galactic foregrounds are unnecessary. In particular, inclusion of the SFD dust template is unnecessary since gamma rays are highly penetrating and not subject to appreciable dust extinction. We have explicitly verified that the difference between the results

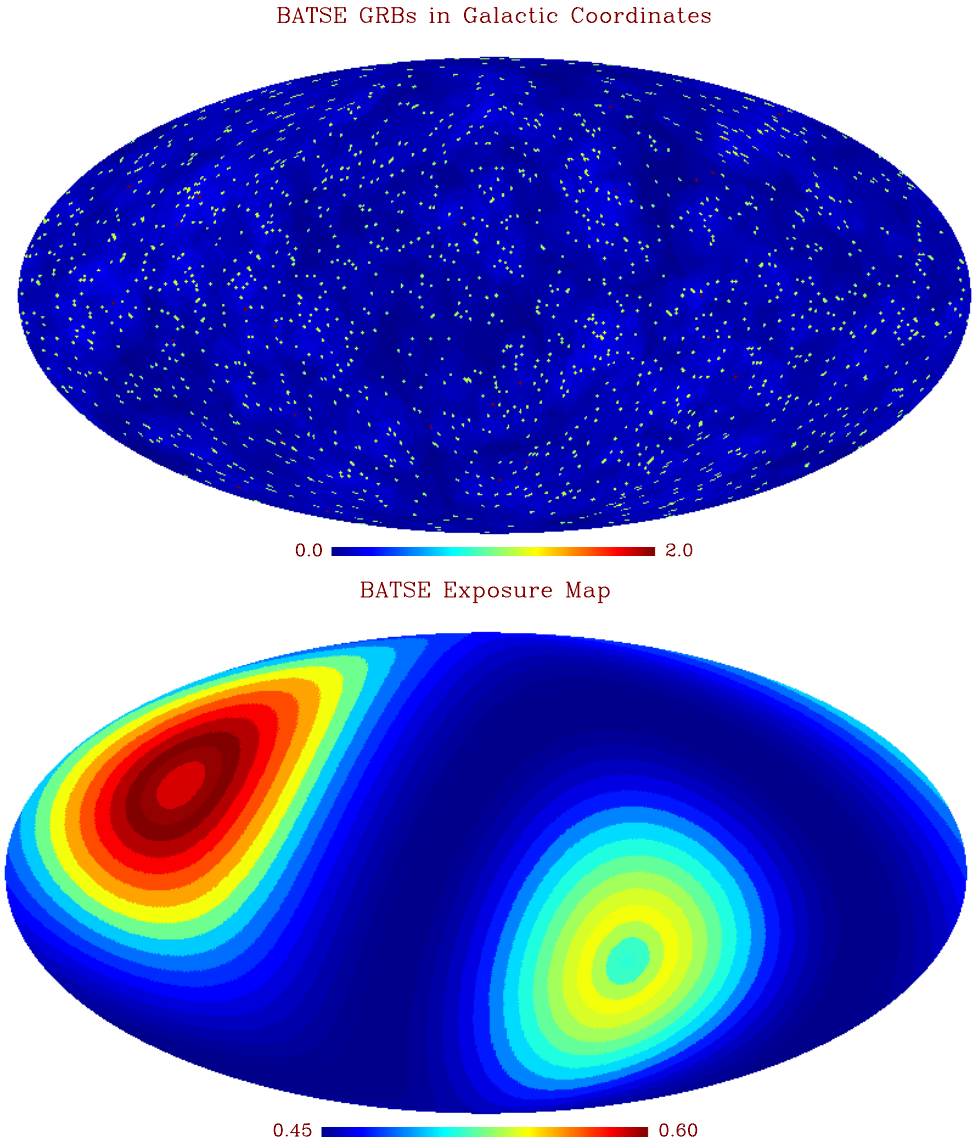

Figure 5.1: *Top:* GRB positions as recorded by BATSE, with error bars indicated as light circles/ovals around the GRBs; pixellized at HEALPix NSIDE=64 (dynamic range limited to 2 even though a few pixels have 3 counts in them). *Bottom:* The BATSE exposure function, which varies with declination, in Galactic coordinates.

including SFD template and not including SFD template is completely negligible. In principle, there is the possibility of confusion with soft gamma repeaters (SGRs) or other sources of gamma rays (pulsars, terrestrial gamma-ray flashes, black holes, etc.). This is highly unlikely given that GRBs are easy to distinguish from other gamma-ray sources based on spectral and time-domain data. However, any foreground objects that might contaminate a pure GRB sample are expected to vary with Galactic latitude, and since there is no reason not to do so, we run our usual test of progressively excising the Galactic plane. However, we expect no issues with astrophysical foregrounds given the relatively clean nature of GRBs as a source; in fact, no sky cut at all should be necessary.

In all tests below, the systematic template we do use, as alluded to above, is the BATSE exposure function, which varies significantly with declination, mimicking (partially) a dipole (see Fig. 5.1). This is a very important template to include, as some of the results presented below change both quantitatively and qualitatively (e.g., statements we would make about the supergalactic plane are different) if this template is not taken into account.

Given that cosmic variance should be much smaller on these scales than it was for 2MASS, we expect when we vary Galactic b that all results will be consistent with all other results within the *measurement* error bars, regardless of sky cut. Results for varying Galactic b are given in Table A.7. From the corresponding figure, Fig. 5.2, it is clear that all results are indeed consistent with all other results within the measurement error bars. As expected, there is no detectable signal that varies with Galactic latitude.

We now proceed to run the usual test cutting the supergalactic plane. It should be noted that for some cuts, a dipole is detected at marginal significance in this

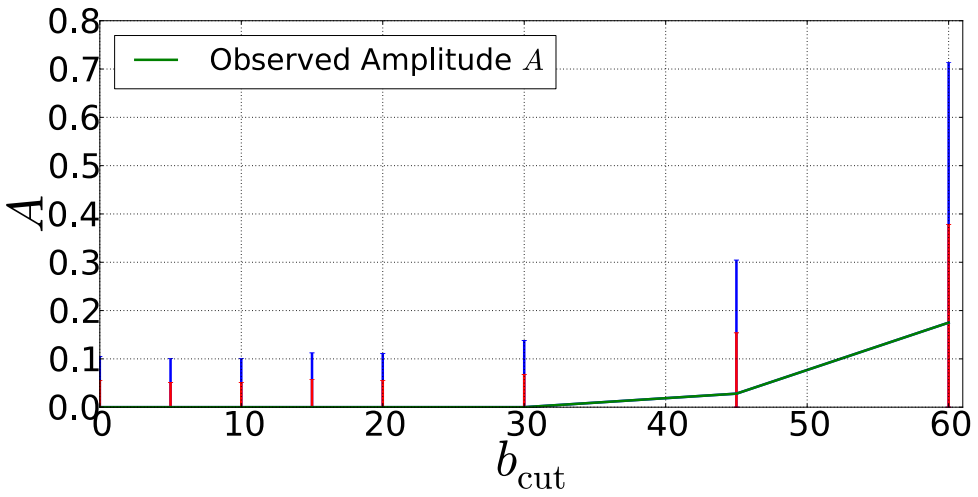

Figure 5.2: Dipole amplitude in BATSE as a function of $b_{\rm cut}$. Note that all measurements of the dipole amplitude for different Galactic cuts are mutually consistent, and are consistent with zero as well. Measurement errors in the form of 68 and 95 percent confidence intervals are shown; they tend to grow (naturally) with the aggressiveness of the cut.

series of tests *if the BATSE exposure function is not taken into account.* Any kind of detection of the supergalactic plane in gamma-ray bursts would be very surprising given the complete lack of any association between GRBs and the local structure represented by the SGP (which goes out to something on the order of $z \sim 0.02$ or 0.03, depending on estimates; see Lahav et al. (2000)), but the result turns null when we account for the exposure function. See Tables A.8 and especially 5.1 for the results of cutting in supergalactic latitude.

Table 5.1: Key patterns in cutting in supergalactic coordinates, for BATSE gamma-ray bursts.

$\lvert\text{SGB}\rvert \geq$	$f_{\rm sky}$	N	$f_{\rm sources}$	$\frac{f_{\rm sources}}{f_{\rm sky}}$	$A_{\rm peak}$	$\lvert\text{SGB}\rvert <$	$f_{\rm sky}$	N	$f_{\rm sources}$	$\frac{f_{\rm sources}}{f_{\rm sky}}$	$A_{\rm peak}$
0.0	1.00	1637	1.00	1.00	0.00						
2.0	0.97	1577	0.96	1.00	0.00	74.82	0.97	1582	0.97	1.00	0.00
5.0	0.91	1495	0.91	1.00	0.05	65.90	0.91	1504	0.92	1.01	0.00
10.0	0.83	1333	0.81	0.99	0.06	55.73	0.83	1362	0.83	1.01	0.00
20.0	0.66	1060	0.65	0.98	0.00	41.15	0.66	1122	0.69	1.04	0.00

We find another null result, which is good considering that detection of the supergalactic plane in GRB data would be a highly unusual find, and would almost

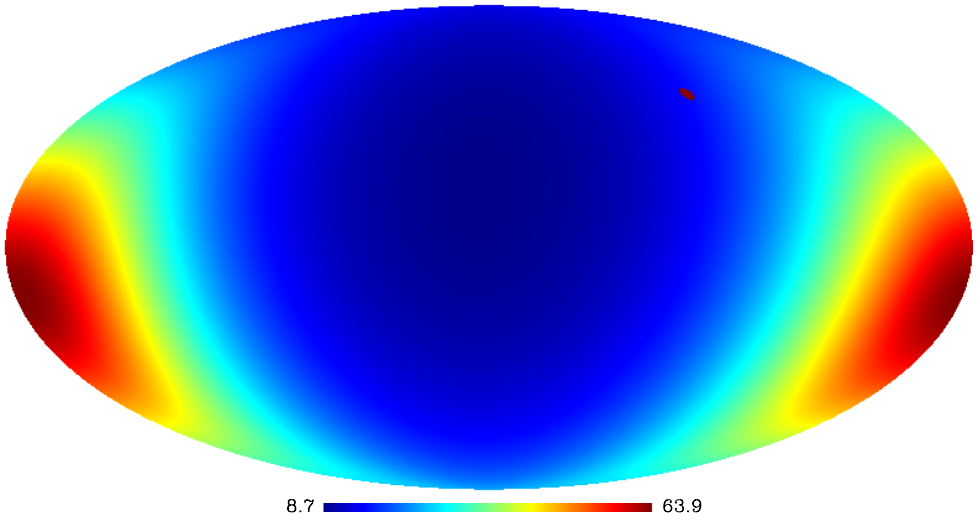

Figure 5.3: Likelihood function for dipole direction, marginalizing over amplitude A, for the entire BATSE catalogue of 1637 GRBs, no cut in Galactic b, with the BATSE exposure function used as a systematic template. There are essentially no constraints on the dipole direction in BATSE data.

certainly indicate something problematic about our analysis. Notice that the direction of the dipole jumps around a good deal as a function of where we place the cut, which is no surprise given the looseness of constraints on dipole direction from the BATSE data (see Sec. 5.2.3).

5.2.3 Dipole Direction and Conclusion

The still-relatively-small number of gamma-ray bursts (1637) in the BATSE catalog places only the loosest of constraints on the direction of the dipole. See Fig. 5.3. All but a very tiny patch of sky (centered around $(l, b) = (5°, 20°)$, and extending a little under 10 degrees in radius) is within the 3-sigma confidence interval for the direction of the dipole, and the CMB kinematic dipole direction (which is an appropriate direction of comparison in this case, since the kinematic dipole should dominate contributions to the dipole for GRBs) is only marginally outside the 1-sigma confidence interval.

In all, the BATSE data places useful constraints on the dipole amplitude, but

not direction, in GRB data. Our results, while they are not yet strong enough to allow for the detection of the expected kinematic dipole, do place constraints on our ability to distinguish BATSE GRBs as a tracer of large-scale structure, and also constrain any intrinsic dipole in the large-scale structure that would manifest itself in the distribution of GRBs on our sky: at 95 percent confidence, $A < 0.105$ for the intrinsic dipole. We have also, in effect, performed several sanity checks on the BATSE dataset, showing that the supergalactic plane is undetectable (as expected) using our analysis, that the Galaxy does not show up at all in the data (which is in line with previous studies of the GRB distribution), and that the BATSE exposure map must be taken into account in order for these tests not to turn up anomalous. We would of course still like to see constraints on the intrinsic dipole much better than those available from GRBs, those constraints being on the order of 10^{-1}. For this, we turn to the radio survey NVSS.

5.3 Dipole in NVSS

For a long time, it was assumed that the distribution of radio sources was, like that of GRBs, indistinguishable from isotropic and unclustered (e.g., Webster (1976)). In fact, even if the distribution of radio sources was not intrinsically isotropic, radio sources have a large range of intrinsic luminosities, and so structures would naturally wash out when sources were projected onto the sky and radial information was removed (Baleisis et al. (1998)). However, recent results, especially using the NRAO VLA Sky Survey (NVSS), have detected clustering in radio sources, and in particular, a dipole.

5.3.1 Previous Work

Several attempts at calculating the dipole in radio sources have been made in recent years.

Baleisis et al. (1998) present theoretical predictions and observational results for the dipole in the Green Bank 1987 and Parkes-MIT-NRAO (PMN) catalogs. The combination of these catalogs gives $\sim 40,000$ sources with flux > 50 mJy at 4.85 GHz. They find that the magnitude of the dipole is an order of magnitude larger than expected from the contributions of large-scale structure (analogous to our local-structure dipole) and the kinematic dipole. However, they are plagued by several systematic errors. First, they find that the two catalogs they used have a mismatch in flux. While they correct for this, it is hard to do so with high precision and confidence. They also note that the radio sources in their catalogs are likely drawn from multiple populations, though this is true of any analysis that uses radio sources, and is not a crippling problem if the redshift distribution is sufficiently well-understood.

Blake and Wall (2002) attempt to measure the kinematic dipole alone in NVSS (see also Blake et al. (2004) for analysis of the rest of the angular power spectrum in NVSS). They make efforts to remove the contribution of what they refer to as the "clustering dipole," the dipole that when flux-weighted gives a measure of the acceleration of the Local Group, and when unweighted matches up with our local-structure dipole. They claim that the clustering dipole should die away by $z < 0.03$ (based on results from the Rowan-Robinson et al. (2000) analysis of the IRAS PSCz dipole, though the results of Erdogdu et al. (2006) call this convergence into question) and contribute roughly $A \sim 2 \times 10^{-3}$ to the total amplitude of the total dipole, if it is not removed as they attempt to do. (Note that we have converted from their peak-to-trough "amplitude" δ to our peak-to-zero amplitude A).

Blake and Wall measure the remaining dipole – which would ideally be a kinematic dipole only, but which will in reality take contributions not only from local structure beyond what IRAS observed, but also from more distant large-scale structure, as we show below – by expanding the angular distribution of sources in spherical harmonics and measuring the harmonic coefficients $a_{\ell,m}$ for the dipole, quadrupole, and octopole, including all m values. Inclusion of higher harmonics is necessary because of the lack of full-sky coverage. They find that a dipole model (with the quadrupole and octopole that would be expected of an initially pure dipole on a sky that gets cut) is a good fit by χ^2, and find good agreement with the direction of the CMB velocity dipole (which they cite as $\theta = 97.2 \pm 0.1°, \phi = 168.0 \pm 0.1°$, which converts to $(l, b) = 264.3°, 48.1°$).

We take the Blake and Wall results as the most reliable previous result, and compare our results to theirs. However, we do have reason to expect that our estimate of the dipole will be more reliable than theirs; in particular, we do a great deal more to take systematic effects into account than they do in their analysis, using our real-space estimator. We also do not attempt to remove local sources as they do, since our objective is to compare our observational results to the full dipole signal expected from theory, which includes both a local-structure and a kinematic contribution. Since we are not flux-weighting, local sources do not contribute preferentially to the dipole, and so we can afford to leave them in the analysis.

Singal (2011) has performed the most recent analysis in this vein. He attempts to address only the kinematic dipole, creating maps of randomly distributed radio sources, then applying a correction to the random map in accord with the effects of relativistic aberration and the Doppler effect due to motion with respect to the rest frame of the radio sources (i.e., the frame in which the sources are distributed

isotropically), and doing a best-fit analysis comparing these maps with the actual distribution of NVSS sources. His results are suspicious, as he finds truly exorbitant speeds for the Local Group (on the order of 1700 km/s). This becomes more understandable given that the way in which he accounts for the sky cut, particularly the hole in NVSS at declination $< 40°$, is suspect (he simply cuts out dec $> 40°$ as well in order to counterbalance the hole at $< 40°$). Also, his method of detecting the dipole does not account for coupling between the dipole and other multipoles on the cut sky, and also neglects any contribution from the local-structure dipole to the results.

5.3.2 Theoretical Predictions

For NVSS, we must be careful to include in our theoretical predictions the contributions of not only the local-structure dipole, but also the kinematic dipole. It is no longer the case, as it was for 2MASS and 2MRS, that the kinematic dipole is swamped by two orders of magnitude by the local-structure dipole. Rather, the two are on the same order of magnitude, as also recognized by Baleisis et al. (1998) and Blake and Wall (2002).

The local-structure contribution is calculated in the same way as always. This part of the prediction will vary somewhat depending on what redshift distribution $n(z)$ we use. Dunlop and Peacock (1990) derived $n(z)$ for several different flux cutoffs, though the results for the dipole amplitude and the redshift distribution itself are somewhat robust to changes in the flux cutoff since radio galaxies display such a wide range of intrinsic luminosities (Baleisis et al. (1998); Blake et al. (2004) note specifically that for the NVSS frequency of 1.4 GHz, the clustering of radio galaxies is not strongly dependent on flux for fluxes between 3 mJy and 50 mJy). The redshift distribution developed by Ho et al. (2008) as a best model for NVSS avoids

several drawbacks of the Dunlop and Peacock distribution, especially the assumption that bias is redshift-independent and the heavy reliance on the functional form of the luminosity function rather than data in constraining the redshift distribution. However, without repeating Ho et al.'s rather sophisticated analysis, we are left unable to calculate the redshift distribution for flux cuts different than the 2.5 mJy cut that they use.

Still, remembering that the predictions are not strongly tied to the flux cutoff, we follow Ho et al. in modeling the NVSS redshift distribution as follows:

$$W(z) = \frac{\alpha^{\alpha+1}}{z_*^{\alpha+1}\Gamma(\alpha)} b_{\text{eff}} z^{\alpha} e^{-\alpha z/z_*} \tag{5.1}$$

where the function $W(z) = b(z)n(z)$, where $b(z)$ is the bias as a function of redshift and $n(z)$ ($\Pi(z)$ in Ho et al.) is the probability distribution for the galaxy redshift. Ho et al. give $b_{\text{eff}} = 1.98$, $z_* = 0.79$, and $\alpha = 1.18$ as best-fit parameters. Using all of this, we find that for this distribution, the contribution of the local-structure dipole to the total dipole in NVSS is $A = 9.8 \times 10^{-4} = 0.98 \times 10^{-3}$.

Meanwhile, the kinematic dipole may be calculated as follows. We recall from chapter 2 (see equations Eq. (2.17) ff.) that for a large-scale-structure survey, relativistic aberration and the Doppler effect modify the observed angular number density of galaxies $n(\theta)$ in the following way:

$$n(\theta) = \bar{n}\left[1 + 2\tilde{\beta}\cos\alpha\right] \tag{5.2}$$

where x, p, and $\tilde{\beta}$ are explained in chapter 2. Since we could also write

$$n(\theta) = \bar{n}\left[1 + A\cos\alpha\right] \tag{5.3}$$

where the amplitude of the dipole is A (cf. the first equation of chapter 3), we match up the equations and use expressions from chapter 2 to write

$$A = 2\tilde{\beta} = 2[1 + 1.25x(1-p)]\beta. \tag{5.4}$$

where the first term in brackets essentially represents the contribution of relativistic aberration and the second term represents the contribution of the Doppler effect. From the CMB, $\beta = v/c = 1.23 \times 10^{-3}$. Meanwhile, x and p (exponents in the power laws for the intrinsic number counts of galaxies as a function of limiting magnitude, and for the intrinsic flux density of a galaxy as a function of frequency, respectively; see Sec. 2.2.3) are not known precisely, but can be estimated.

This expression is equivalent to that used by Blake and Wall (2002) (converting from their δ to our $A = \delta/2$):

$$A = [2 + x(1 + \alpha)]\,\beta \tag{5.5}$$

with the substitution in Eq. (5.4) $x \to 2x/5$ and $p \to -\alpha$. (The latter substitution is a straightforward matter of notation; the first has to do with switching from magnitudes to fluxes.[1]) We follow Blake and Wall (for NVSS) and also Baleisis et al. (who were not working with NVSS, but who did work with radio catalogs) and take $x \approx 1$ and $\alpha \approx 0.75$, which yields finally

$$A \approx 4.6 \times 10^{-3}. \tag{5.6}$$

This is the contribution of the kinematic dipole to the total dipole. Adding this to the contribution from the local-structure dipole, we expect the total dipole to have amplitude $A = (4.6 + 1.0) \times 10^{-3} = 5.6 \times 10^{-3}$. If we find a result that is outside cosmic-variance errors from this value, and this is not a systematic effect, we might invoke the presence of an intrinsic dipole as an explanation.

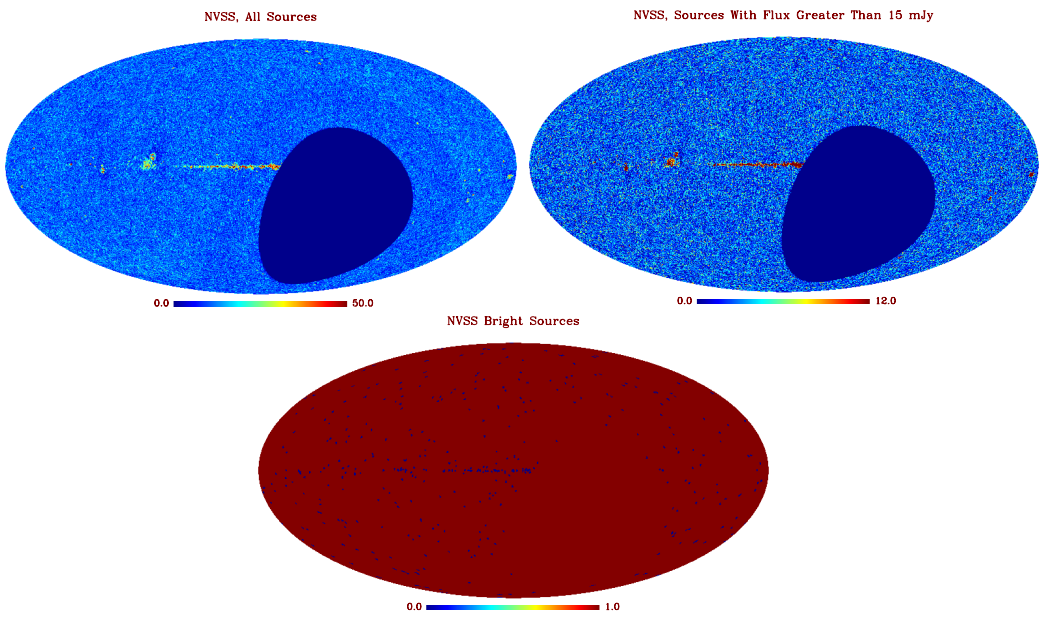

Figure 5.4: (1) All sources in NVSS, in Galactic coordinates. Note the "hole" in the data for declinations less than 40 degrees, and the declination-dependent striping (visible in this coordinate system as a series of "wavy" stripes going outward from the pattern set by the declination-dependent hole in the data). (2) Sources with flux greater than 15 mJy. The spurious power goes largely away with this flux cut, and can no longer be seen by eye. (3) The distribution of bright (> 2500 mJy) sources in NVSS. Pixels that are within 0.6 degrees of a bright source are set to zero in this map, while all other pixels have a value of 1.0. (Dynamic ranges are restricted in both of the first two maps so as to better show structure.)

5.3.3 Present Work

We turn first to examining the systematics that need to be accounted for in the NVSS data. See Fig. 5.4 for reference.

First, the survey did not observe below a declination of 40 degrees. For our purposes, the pixellization around this "hole" in declination is especially important to pay attention to, as we find that a sky cut for pixels with centers at dec $< 40°$ gives vastly different results for the dipole amplitude and direction than a cut at dec $< 37°$ at low-resolution pixellization (NSIDE=16). We work at much higher

[1]In our original notation, which follows Itoh et al. (2010), the number of galaxies detected by the survey is proportional to $10^{xm_{\rm lim}}$, where $m_{\rm lim}$ is the limiting magnitude of the survey. In Blake and Wall (2002), the number of galaxies is proportional to $S^{-x'}$, where S is flux, and we have added a prime to distinguish variables named x. Equating $S^{-x'}$ with $10^{xm_{\rm lim}}$ (up to a proportionality constant) and using the fact that $S \propto 10^{-2m_{\rm lim}/5}$, we have that $2m_{\rm lim}x'/5 = xm_{\rm lim}$, or $x = 2x'/5$. Blake and Wall give $x' \approx 1$.

resolution (NSIDE=128), where the effect is not as strong, but we still cut all pixels with dec $< 37^\circ$ just to be safe. We choose that particular number following Smith and Huterer (2010), and also because this appears to be a good conservative choice if we want to completely avoid problems associated with the hole in declination.

Second, faint sources very close to bright sources cannot be reliably detected. We therefore mask out a 0.6° radius around all sources brighter than 2500 mJy, following Ho et al. (2008). Blake and Wall do not perform this same masking, although they do remove known local sources.

Third, we use the Haslam map of 408 MHz Galactic emission as a systematic template, as discussed in Chapter 3.

Fourth, there is declination-dependent "striping" in the maps, which appears even by eye if no flux cut is imposed. This problem stems from the fact that the NVSS observations were made using two different configurations of the VLA, the D configuration for observations between declinations of -10° and $+78^\circ$, and the DnC configuration for declinations between -40° and -10°, and above $+78^\circ$. The striping is readily apparent by eye for the full catalog, but is invisible by eye and largely absent even in more rigorous tests for fluxes above ~ 15 mJy (see Blake and Wall (2002)). We therefore begin by examining the stability of our dipole results as a function of flux cut.

We find that neither the direction nor the amplitude of the dipole is stable for different flux cuts. This is as expected for fluxes less than 15 mJy, since the striping artifact gradually dies away as the lower flux threshold is increased from zero up to 15 mJy. But for fluxes above 15 mJy, the fact that the dipole remains unstable is a problem. Increases in the amplitude, such as those seen in Table A.9, might be due to the influence of the local-structure dipole, which could come into play more

strongly for these brighter (and therefore at least somewhat more local) sources. Fluctuations in the direction such as those in Table A.9 (the best-fit l ranges from 219.1 to 234.3, and the best-fit b ranges from 11.9 down to -0.2) could also be the result of the local-structure dipole, though this seems unlikely since the b coordinate in particular moves *away* from the direction of the local-structure dipole that we have seen in previous tests using 2MASS as we go to brighter and brighter sources (higher and higher flux thresholds) in NVSS.

Rather than trusting the results of Table A.9, we turn instead to a more aggressive cut in declination, which makes use of only one subset of the NVSS maps, corresponding to the D configuration of the VLA: that is, we remove all portions of the sky with declination less than -10° or greater than 78°. These results show a great deal more stability in the direction of the dipole for flux cuts above 5 mJy, and certainly above 15 mJy. See Table A.10 for complete results; visually, the results are plotted and compared to those of Blake and Wall in Fig. 5.5.

We verify in Table A.11 that the results are stable as a function of cut in Galactic b for the fixed case of a flux cut at 25 mJy. This provides our usual test for contamination that varies as a function of Galactic latitude, and helps justify our choice of $|b| < 15°$ for our cut. Again, though the observational results are not consistent with one another within measurement error bars, the very aggressive sky cuts used here mean small $f_{\rm sky}$ and thus large cosmic variance.

We regard the result with a flux cut at 15 mJy and $|b| < 15°$ as paradigmatic, since it provides the best compromise between a large number of sources (getting more sources requires getting into flux ranges where the results are less trustworthy) and having stable results for the dipole (instability in the dipole amplitude for more aggressive flux cuts likely being due to the presence of the local-structure dipole,

which would tend to be more strongly present for brighter sources). We therefore compute cuts around the supergalactic plane (see Table A.12; the results are extremely stable this time, with the ratio $f_{\rm sky}/f_{\rm sources}$ changing by less than 1 percent in all but one of the SGB cuts we study) with this result as the fiducial, and compute our likelihood distribution $P(C_1^{\rm th}|C_1^{\rm obs})$ based off this case. We also calculate the direction of the dipole for this same case, and compare with the CMB kinematic dipole. Results appear in Fig. 5.6. The final plot of this chapter is Fig. 5.7, which depicts the different cuts used in various portions of the analysis for NVSS.

We find that for an observed dipole amplitude of $A = 0.0272$, the theoretical value of $A = 0.0056$ is *not* consistent with observations, at well over 99 percent confidence. The reasonable implication is that the dipole we are measuring in the NVSS map is partially spurious. There are several possible sources of this spurious signal: the two most likely are that the declination-dependent striping may not be wholly taken care of in the maps we test, even with our aggressive flux cuts (observational error); or that local sources contribute more strongly to the local-structure dipole than our theoretical modeling allowed for, thus lifting the local-structure dipole's contribution to the order of 10^{-2} rather than 10^{-3} (theoretical error). The latter seems especially likely given that the theoretical prediction for the dipole amplitude was computed using a flux cut of 2.5 mJy, while the observational results were computed using a flux cut of 15.0 mJy. Although the theoretical predictions are ideally fairly robust to flux cuts, this is an order-of-magnitude difference in flux and therefore likely to change the theoretical predictions at least somewhat, adding back in the local-structure dipole that we expected to be subdominant. Unfortunately, our observational results are unreliable when we use the same flux cut as assumed in theoretical predictions, which is probably due to the peculiar nature of the NVSS maps, with their declination-

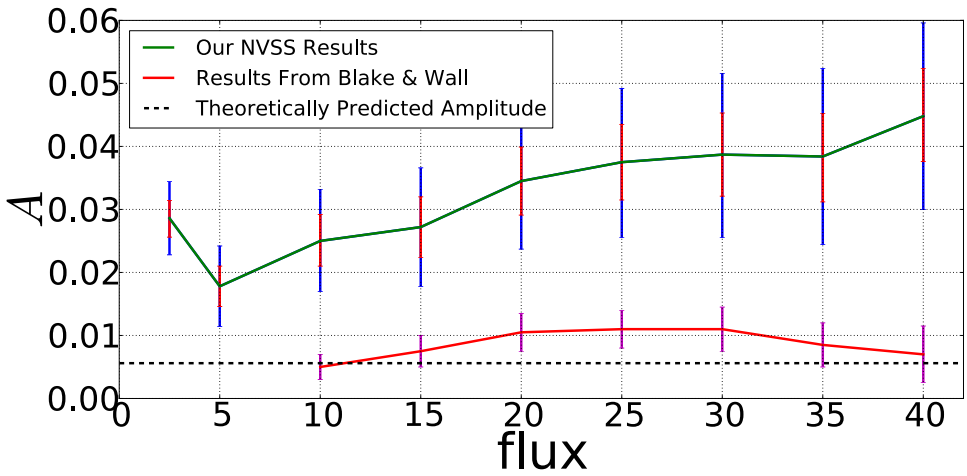

Figure 5.5: Amplitude as a function of flux cut, with error bars. We show both our results and those from Blake and Wall (2002). We include the Haslam et al. map of 408 MHz Galactic emission as a systematics template, and remove $|b| < 15°$ and dec greater than 78 degrees/less than -10 degrees. We suspect that the upward trend in the results is due to the presence of local structure in the NVSS map we test, since local structures preferentially have higher fluxes. Blake and Wall cut out this local structure in an effort to search for the kinematic dipole only, so it is expected that our results differ from theirs, and give a higher signal. Note also that our cut in declination is different than that of Blake and Wall; this is in an effort to remove all artifacts stemming from the declination-dependent striping of NVSS corresponding to two different configurations of the VLA in which NVSS data was acquired. The apparent agreement between theoretical predictions and the Blake and Wall results is partially misleading, in that the theoretical prediction includes contributions from both the kinematic dipole and the local-structure dipole, but Blake and Wall were attempting to measure only the kinematic dipole.

dependent striping.

All this said, it is clear that radio surveys of this sort are an excellent setting for the tests we perform, and we look forward to maps from, e.g., LOFAR and SKA to perform similar tests.

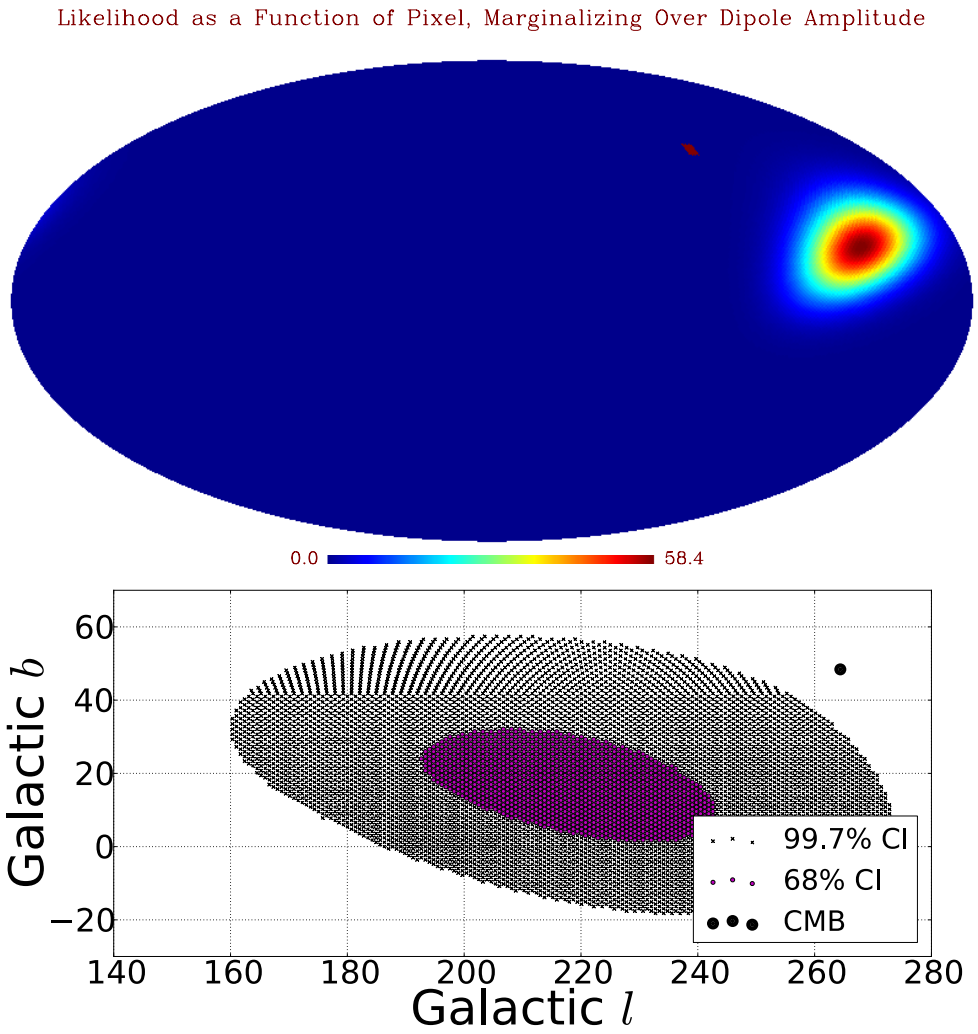

Figure 5.6: (1) Likelihood of dipole direction in NVSS, marginalizing over amplitude. (2) The CMB dipole direction is over 3 sigma away from the best-fit NVSS dipole direction. This is not a problem, however, since the NVSS dipole amplitude $A \sim 10^{-2}$ still, and we expect the CMB dipole to come into play only at the level of dipole amplitudes $A \sim 10^{-3}$. These plots all correspond to the case in which sources have flux greater than 15 mJy, only declinations between $-10°$ and $78°$ are kept, and $|b| < 15°$ is cut.

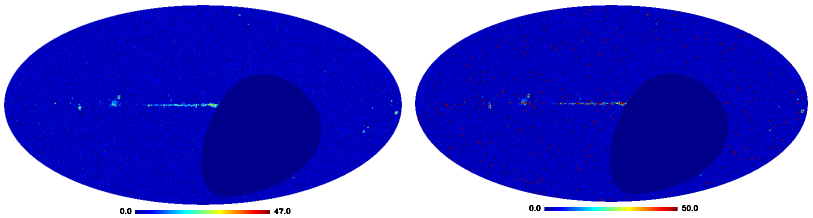

no cut; only bright sources cut

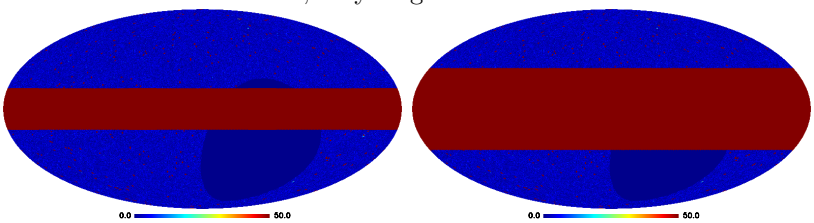

$|b| < 15°$; $|b| < 30°$

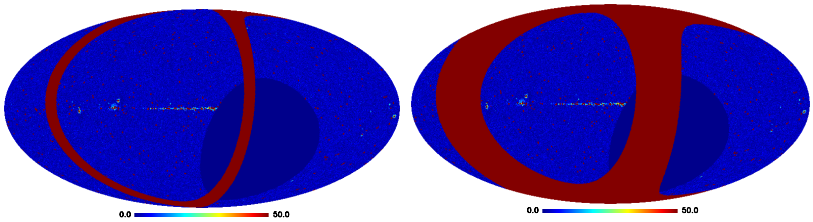

$|\mathrm{SGB}| < 5°$; $|\mathrm{SGB}| < 20°$

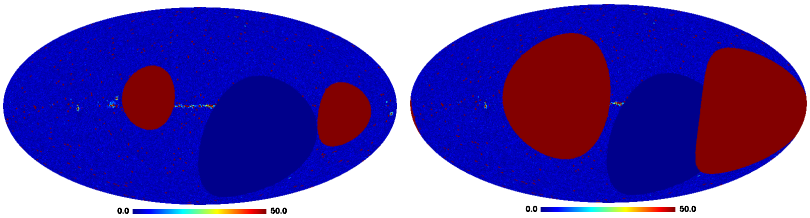

$|\mathrm{SGB}| > 65.90°$; $|\mathrm{SGB}| > 41.15°$

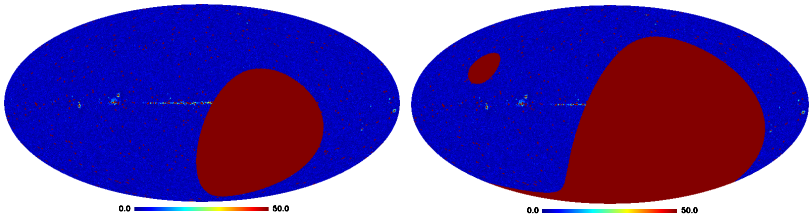

$\mathrm{dec} < -37°$; $\mathrm{dec} < -10°$ or $\mathrm{dec} > 78°$

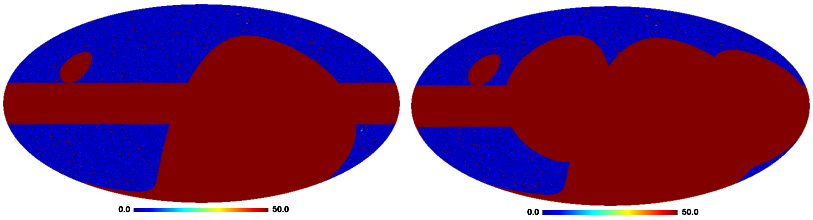

same as immediately above but with $|b| < 15°$ and $|\mathrm{SGB}| > 41.15°$ also cut

Figure 5.7: Various cuts employed in the analysis of the NVSS map. The background map is the NVSS map with all the sources that have flux greater than 15 mJy.

CHAPTER VI

Summary and conclusions

In this dissertation, I have focused on what might be called the most straightforward tests of statistical isotropy in large-scale structure – looking for dipole signals in existing surveys over a wide range of wavelengths. In turns out that, despite the relative straightforwardness of the tests themselves (Chapter 3), the results must be carefully interpreted, as dipole signals take contributions from several different sources, some of which are theoretically quite well-understood (local-structure and kinematic dipoles), and others of which may be much less well-understood (intrinsic dipole) (Chapter 2). Observational results in infrared (2MRS/2MASS; Chapter 4), gamma rays (CGRO/BATSE; Chapter 5), and radio (NVSS; Chapter 5) turn up no seriously unexpected results, in either dipole amplitude or dipole direction. As long as we are careful to take all sources of dipole signal into account in our theoretical modeling, the observational results are in line with theoretical predictions. Rigorous tests of this sort, while they ultimately turn up no unexpected results, are valuable tests of current cosmological models, as they add new wavebands in which rigorous tests of statistical isotropy have been conducted, and ensure that statistical isotropy is probed at different epochs, using different surveys with different systematics. Combined with similar tests using maps of the cosmic microwave

Table 6.1: Summary of most reliable single results from each survey. From left to right in the table appear the name of the survey, the redshift range probed by the survey, the fraction of the sky covered, the number of sources available in the most reliable subset of the dataset, the observed dipole amplitude with error bar, the theoretical dipole amplitude (with cosmic-variance error bar if applicable), the direction of the best-fit observed dipole in Galactic coordinates (l, b), and the most important systematic effect (in some cases, out of several candidates) that must be taken into account in attempting to detect a dipole in the dataset.

Survey	Redshift	$f_{\rm sky}$	N	$A_{\rm obs}$	$A_{\rm th}$	$(l,b)_{\rm obs}$
2MRS	$0 < z < 0.1$	0.86	41,834	0.118 ± 0.009	0.311 ± 0.122	$(222.3°, 38.3°)$
2MASS	$0 < z \lesssim 0.2$	0.65	386,008	0.088 ± 0.003	0.084 ± 0.033	$(305.0°, 4.5°)$
BATSE	$\bar{z} \gtrsim 2$	1.00	1637	< 0.056 (68% CL)	[unc. prediction]	[weak constraints]
NVSS	$\bar{z} \sim 1$	0.42	211,487	0.027 ± 0.005	0.0056	$(214.5°, 15.6°)$

background, these measurements impose interesting constraints on models of, and physical processes during, cosmological inflation. We provide a summary of the most basic results, which are elaborated upon heavily in the body of the thesis, in Table 6.1.

Other surveys may provide interesting candidates for these same kinds of tests in the future. Sloan luminous red galaxies (LRGs) are a sufficiently clean dataset that these tests may be applicable and workable there (see, e.g., Abate and Feldman (2012) for a related test). Also, survey results that have yet to be released may be useful. The Wide-field Infrared Survey Explorer (WISE), which produced a preliminary data release in April 2011 and has full-survey results forthcoming now, covers more than 99 percent of the sky (Wright et al. (2010)). Tests performed on WISE would be similar to tests performed on 2MASS, but would update 2MASS results with a more recent and *much* deeper survey. As the X-ray background becomes better-understood, this may also serve as an increasingly valuable test of statistical isotropy and setting in which to attempt to detect dipole signals. The Dark Energy Survey (DES) will be useful in probing the distribution of galaxies to high redshift, and will have sufficient sky coverage to make the tests presented here useful. In microwaves, dipole signals

might be detectable in maps of the gravitational lensing of the CMB, which provide a very good tracer of mass. Finally, new radio surveys such as LOFAR and SKA will probe orders of magnitude more sources down to far lower flux thresholds than NVSS (see, e.g., Crawford (2009)), and would provide very valuable updates to NVSS results on the dipole amplitude and direction. The kinematic dipole, both direction and amplitude, should be unambiguously detected in these surveys.

APPENDICES

APPENDIX A

Tables

The tables provided here give useful information for reference should detailed questions arise about exact cutoffs for confidence intervals, peak amplitudes, numbers of sources, best-fit dipole directions, etc.

Table A.1: Comparison of dipole parameters with different sky cuts, for 2MRS.

$\|b\| \geq$	Systematics	NSIDE	N	$A_{\rm peak}$	l	b	68 percent CI	95 percent CI
8.0	SFD	128	41834	0.1185	222.2	38.3	0.11 - 0.1265	0.102 - 0.135
15.0	SFD	128	36610	0.1220	238.9	38.0	0.113 - 0.131	0.1045 - 0.1405
20.0	SFD	128	32644	0.1180	252.2	40.5	0.1085 - 0.128	0.099 - 0.137
30.0	SFD	128	24844	0.1007	192.5	75.5	0.0925 - 0.1098	0.0842 - 0.1187
45.0	SFD	128	14079	0.1823	257.6	56.6	0.1673 - 0.1973	0.1545 - 0.2138
60.0	SFD	128	6735	0.2940	205.8	39.6	0.258 - 0.3315	0.228 - 0.372

Table A.2: Cutting in supergalactic coordinates, for 2MRS.

$\|SGB\| \geq$	$f_{\rm sky}$	Systematics	NSIDE	N	$A_{\rm peak}$	l	b	68 percent CI	95 percent CI
0.0	0.86	SFD	128	41834	0.1184	222.2	38.3	0.11 - 0.1268	0.102 - 0.1352
2.0	0.82	SFD	128	39964	0.1092	213.9	31.3	0.1004 - 0.1176	0.092 - 0.126
5.0	0.78	SFD	128	37124	0.1055	202.6	22.4	0.0965 - 0.1145	0.0875 - 0.123
10.0	0.70	SFD	128	32673	0.0965	201.9	11.9	0.0875 - 0.106	0.078 - 0.115
20.0	0.55	SFD	128	24799	0.0805	217.3	8.0	0.0705 - 0.09	0.061 - 0.0995
$\|SGB\| <$	$f_{\rm sky}$	Systematics	NSIDE	N	$A_{\rm peak}$	l	b	68 percent CI	95 percent CI
74.82	0.84	SFD	128	41234	0.1185	222.2	38.3	0.11 - 0.127	0.102 - 0.1355
65.90	0.81	SFD	128	39867	0.1175	219.5	41.4	0.109 - 0.126	0.1005 - 0.1345
55.73	0.74	SFD	128	36882	0.1160	224.9	47.5	0.107 - 0.125	0.0985 - 0.134
41.15	0.59	SFD	128	30321	0.1380	220.0	29.3	0.125 - 0.151	0.113 - 0.164

Table A.3: Results as a function of cut in Galactic b for 2MASS, $K_s < 13.5$.

$\|b\| \geq$	Systematics	NSIDE	N	$A_{\rm peak}$	l	b	68 percent CI	95 percent CI
8.0	SFD	128	496415	0.0674	289.8	10.3	0.0648 - 0.0698	0.0624 - 0.0724
15.0	SFD	128	433261	0.0786	296.3	6.8	0.0758 - 0.0814	0.073 - 0.0842
20.0	SFD	128	386008	0.0882	305.0	4.5	0.085 - 0.0912	0.082 - 0.0944
30.0	SFD	128	294795	0.1137	338.0	4.0	0.1098 - 0.1176	0.1059 - 0.1218
45.0	SFD	128	170985	0.1824	344.0	13.4	0.1761 - 0.189	0.1698 - 0.1953
60.0	SFD	128	78499	0.0952	6.1	25.9	0.0826 - 0.1078	0.0712 - 0.121

Table A.4: Results as a function of cut in Galactic b for 2MASS, $K_s < 12.5$.

$\|b\| \geq$	Systematics	NSIDE	N	$A_{\rm peak}$	l	b	68 percent CI	95 percent CI
8.0	SFD	128	116400	0.0797	245.3	26.8	0.0746 - 0.0848	0.0695 - 0.0899
15.0	SFD	128	101940	0.0836	259.5	25.2	0.0779 - 0.0893	0.0722 - 0.0947
20.0	SFD	128	91008	0.0812	276.3	25.9	0.0752 - 0.0875	0.0692 - 0.0935
30.0	SFD	128	69809	0.0724	350.0	43.4	0.0656 - 0.0792	0.0592 - 0.0864
45.0	SFD	128	39544	0.1120	339.4	57.1	0.1036 - 0.1212	0.0960 - 0.1308
60.0	SFD	128	18336	0.1820	156.9	32.3	0.1580 - 0.2072	0.1352 - 0.2324

Table A.5: Results as a function of cut in supergalactic latitude SGB for 2MASS, $K_s < 13.5$.

$\|$SGB$\| \geq$	$f_{\rm sky}$	Systematics	NSIDE	N	$A_{\rm peak}$	l	b	68 percent CI	95 percent CI
0.0	0.65	SFD	128	386008	0.0882	304.9	4.5	0.085 - 0.0912	0.082 - 0.0944
2.0	0.63	SFD	128	368077	0.0792	303.5	5.1	0.076 - 0.0824	0.0728 - 0.0856
5.0	0.59	SFD	128	342390	0.0700	302.0	7.4	0.0666 - 0.0734	0.0632 - 0.0766
10.0	0.52	SFD	128	301028	0.0550	295.7	12.5	0.0514 - 0.0586	0.0478 - 0.0622
20.0	0.39	SFD	128	225502	0.0538	293.4	12.6	0.0493 - 0.0583	0.045 - 0.0628
$\|$SGB$\| <$	$f_{\rm sky}$	Systematics	NSIDE	N	$A_{\rm peak}$	l	b	68 percent CI	95 percent CI
74.82	0.65	SFD	128	385740	0.0882	304.8	4.4	0.085 - 0.0912	0.082 - 0.0944
65.90	0.64	SFD	128	378368	0.0866	310.2	6.2	0.0836 - 0.0898	0.0804 - 0.0928
55.73	0.60	SFD	128	355464	0.0888	323.9	8.4	0.0858 - 0.092	0.0826 - 0.095
41.15	0.49	SFD	128	295090	0.0894	327.5	3.3	0.0862 - 0.0928	0.0828 - 0.096

Table A.6: Results as a function of cut in supergalactic latitude SGB for 2MASS, $K_s < 12.5$.

$\|$SGB$\| \geq$	$f_{\rm sky}$	Systematics	NSIDE	N	$A_{\rm peak}$	l	b	68 percent CI	95 percent CI
0.0	0.65	SFD	128	91008	0.0812	276.3	25.9	0.0752 - 0.0875	0.0692 - 0.0935
2.0	0.63	SFD	128	86657	0.0668	266.6	25.6	0.0605 - 0.0731	0.0542 - 0.0791
5.0	0.59	SFD	128	80177	0.0548	249.0	28.8	0.0484 - 0.0612	0.0424 - 0.0676
10.0	0.52	SFD	128	70212	0.0500	230.9	26.3	0.0436 - 0.0568	0.0372 - 0.0632
20.0	0.39	SFD	128	52528	0.0448	243.5	16.9	0.0376 - 0.0524	0.0304 - 0.0596
$\|$SGB$\| <$	$f_{\rm sky}$	Systematics	NSIDE	N	$A_{\rm peak}$	l	b	68 percent CI	95 percent CI
74.82	0.65	SFD	128	90951	0.0812	276.4	25.9	0.0752 - 0.0875	0.0692 - 0.0935
65.90	0.64	SFD	128	89203	0.0752	285.2	31.7	0.0692 - 0.0812	0.0632 - 0.0872
55.73	0.60	SFD	128	83805	0.0760	307.8	37.7	0.0704 - 0.082	0.0644 - 0.0876
41.15	0.49	SFD	128	69923	0.0760	283.8	26.9	0.0688 - 0.0832	0.062 - 0.0904

Table A.7: Results as a function of cut in Galactic b for BATSE.

$\|b\| \geq$	Systematics	NSIDE	N	$A_{\rm peak}$	l	b	68 percent CI	95 percent CI
0.0	Exposure	128	1637	0.0000	179.5	-15.8	0.0 - 0.0555	0.0 - 0.105
5.0	Exposure	128	1481	0.0000	175.3	-20.4	0.0 - 0.051	0.0 - 0.1005
10.0	Exposure	128	1331	0.0000	252.7	-17.3	0.0 - 0.051	0.0 - 0.1005
15.0	Exposure	128	1190	0.0000	315.3	-17.2	0.0 - 0.057	0.0 - 0.1125
20.0	Exposure	128	1073	0.0000	223.9	-44.4	0.0 - 0.0555	0.0 - 0.111
30.0	Exposure	128	802	0.0000	149.5	-14.1	0.0 - 0.0675	0.0 - 0.138
45.0	Exposure	128	475	0.0280	249.6	-19.1	0.0 - 0.154	0.0 - 0.3045
60.0	Exposure	128	215	0.1750	203.0	-14.8	0.0 - 0.378	0.0 - 0.714

Table A.8: Results as a function of cut in supergalactic latitude SGB for BATSE.

$\|$SGB$\| \geq$	$f_{\rm sky}$	Systematics	NSIDE	N	$A_{\rm peak}$	l	b	68 percent CI	95 percent CI
0.0	1.00	Exposure	128	1637	0.0000	179.5	-15.7	0.0 - 0.0555	0.0 - 0.105
2.0	0.97	Exposure	128	1577	0.0000	172.1	-10.9	0.0 - 0.0615	0.0 - 0.1155
5.0	0.91	Exposure	128	1495	0.0480	160.2	-24.3	0.0 - 0.084	0.0 - 0.1425
10.0	0.83	Exposure	128	1333	0.0600	159.3	-8.4	0.0 - 0.096	0.0 - 0.16
20.0	0.66	Exposure	128	1060	0.0000	177.4	-17.8	0.0 - 0.078	0.0 - 0.144
$\|$SGB$\| <$	$f_{\rm sky}$	Systematics	NSIDE	N	$A_{\rm peak}$	l	b	68 percent CI	95 percent CI
74.82	0.97	Exposure	128	1582	0.0000	167.9	-18.0	0.0 - 0.0525	0.0 - 0.102
65.90	0.91	Exposure	128	1504	0.0000	166.3	-21.2	0.0 - 0.0525	0.0 - 0.1035
55.73	0.83	Exposure	128	1362	0.0000	112.6	-17.8	0.0 - 0.054	0.0 - 0.108
41.15	0.66	Exposure	128	1122	0.0000	213.0	-18.6	0.0 - 0.07	0.0 - 0.148

Table A.9: Results in NVSS as a function of flux cut (fluxes given in the first column, in mJy). The Haslam systematics template is taken into account (H), the areas around bright sources are masked (B), and dec $< -37°$ is cut.

flux >	$b \geq$	Systematics	NSIDE	N	$A_{\rm peak}$	l	b	68 percent CI	95 percent CI
2.5	15.0	HB	128	1164141	0.0212	185.5	13.7	0.0192 - 0.0232	0.017 - 0.0252
5.0	15.0	HB	128	688024	0.0238	173.1	26.5	0.0212 - 0.0264	0.0186 - 0.029
10.0	15.0	HB	128	415841	0.0256	199.5	15.6	0.0222 - 0.029	0.0188 - 0.0324
15.0	15.0	HB	128	299438	0.0296	219.1	11.9	0.0256 - 0.0336	0.0218 - 0.0376
20.0	15.0	HB	128	233565	0.0366	224.6	8.9	0.0322 - 0.0412	0.0276 - 0.0456
25.0	15.0	HB	128	190476	0.0406	226.5	9.0	0.0355 - 0.0454	0.0307 - 0.0505
30.0	15.0	HB	128	160396	0.0415	225.1	9.0	0.0361 - 0.0469	0.0307 - 0.0523
35.0	15.0	HB	128	138109	0.0418	230.9	3.8	0.0361 - 0.0478	0.0301 - 0.0535
40.0	15.0	HB	128	120780	0.0475	234.3	-0.2	0.0412 - 0.0538	0.0349 - 0.0601

Table A.10: Results in NVSS as a function of flux cut (fluxes given in the first column, in mJy). The Haslam systematics template is taken into account (H), the areas around bright sources are masked (B), and areas outside $-10° <$ dec $< 78°$ are cut.

flux >	$b \geq$	Systematics	NSIDE	N	$A_{\rm peak}$	l	b	68 percent CI	95 percent CI
(no cut)	15.0	HB	128	921443	0.0482	273.1	-30.7	0.0452 - 0.051	0.0424 - 0.054
2.5	15.0	HB	128	830017	0.0286	258.2	-23.1	0.0256 - 0.0314	0.0228 - 0.0344
5.0	15.0	HB	128	489002	0.0178	205.0	17.1	0.0146 - 0.021	0.0114 - 0.0242
10.0	15.0	HB	128	294538	0.0250	210.1	13.8	0.021 - 0.0292	0.017 - 0.0332
15.0	15.0	HB	128	211487	0.0272	214.5	15.6	0.0224 - 0.032	0.0178 - 0.0366
20.0	15.0	HB	128	164658	0.0345	209.5	17.1	0.0291 - 0.0399	0.0237 - 0.0453
25.0	15.0	HB	128	134211	0.0375	210.5	16.2	0.0315 - 0.0435	0.0255 - 0.0492
30.0	15.0	HB	128	112985	0.0387	209.5	16.0	0.0321 - 0.0453	0.0255 - 0.0516
35.0	15.0	HB	128	97126	0.0384	214.0	14.8	0.0312 - 0.0452	0.0244 - 0.0524
40.0	15.0	HB	128	84851	0.0448	217.9	12.4	0.0376 - 0.0524	0.03 - 0.0596

Table A.11: Results in NVSS as a function of cut in Galactic b, for a flux cut of 25 mJy. The Haslam systematics template is taken into account (H), the areas around bright sources are masked (B), and areas outside $-10° <$ dec $< 78°$ are cut.

flux >	$b \geq$	Systematics	NSIDE	N	$A_{\rm peak}$	l	b	68 percent CI	95 percent CI
25.0	15.0	HB	128	134211	0.0375	210.5	16.2	0.0315 - 0.0435	0.0255 - 0.0492
25.0	30.0	HB	128	92709	0.0516	197.5	8.5	0.042 - 0.0612	0.0324 - 0.0704
25.0	45.0	HB	128	55978	0.0707	196.7	5.6	0.0539 - 0.0868	0.0371 - 0.1029
25.0	60.0	HB	128	24375	0.1440	163.1	10.7	0.105 - 0.1815	0.066 - 0.2175

Table A.12: Results in NVSS as a function of cut in supergalactic latitude SGB for a flux cut of 15 mJy. The Haslam systematics template is taken into account (H), the areas around bright sources are masked (B), and areas outside $-10° <$ dec $< 78°$ are cut.

$\lvert$SGB$\rvert \geq$	$f_{\rm sky}$	Systematics	NSIDE	N	$A_{\rm peak}$	l	b	68 percent CI	95 percent CI
0.0	0.42	HB	128	211487	0.0272	214.5	15.8	0.0224 - 0.032	0.0178 - 0.0366
2.0	0.41	HB	128	203357	0.0285	207.3	20.0	0.0237 - 0.0333	0.0189 - 0.0381
5.0	0.38	HB	128	191247	0.0273	212.7	16.3	0.0225 - 0.0321	0.0177 - 0.0369
10.0	0.34	HB	128	172079	0.0270	211.3	17.3	0.0219 - 0.0318	0.0171 - 0.0369
20.0	0.27	HB	128	135501	0.0237	211.7	18.6	0.0183 - 0.0291	0.0129 - 0.0348
$\lvert$SGB$\rvert <$	$f_{\rm sky}$	Systematics	NSIDE	N	$A_{\rm peak}$	l	b	68 percent CI	95 percent CI
74.82	0.42	HB	128	210135	0.0273	213.8	15.5	0.0225 - 0.0321	0.0177 - 0.0366
65.90	0.41	HB	128	204083	0.0297	216.1	15.5	0.0249 - 0.0345	0.0201 - 0.0393
55.73	0.37	HB	128	185801	0.0297	220.1	13.5	0.0243 - 0.0351	0.0189 - 0.0402
41.15	0.30	HB	128	147897	0.0156	246.7	13.4	0.0090 - 0.0231	0.0027 - 0.0306

APPENDIX B

Simple Tests of Dipole-Detecting Formalism

In this appendix, we report the results of various sanity checks performed using the dipole-detecting formalism outlined in Chapter 3. Several other tests have been performed, including similar tests on a map with dipole amplitude $A = 0$ (that is, a map that includes only a monopole with shot noise), and the formalism passes all these tests as well as it passes the sample tests presented here.

First, we examine the effects of introducing a template and then progressively excising the Galactic plane. This mimics tests we perform on all the actual datasets used in this thesis. In this case, we apply the formalism to a map with a pure dipole, shown in Fig. B.1.

The pure-dipole map has a dipole with amplitude $A = 0.1$, in the direction $(l, b) = (61.38°, 33.37°)$. The total number of "counts" in the map is 100,000, corresponding to 100,000 galaxies in a survey. From the first two rows of Table B.1, we note that applying a systematics template (in this case, the 408 MHz map of Haslam et al., corresponding to the systematics template we use when applying the dipole formalism to NVSS maps) may expand the error bars ever so slightly, but essentially has no effect – which is good, given that the map we are testing is an artificial one and should have no contribution that in any way mimics the pattern of 408 MHz emission in the Galaxy. The information in the rest of Table B.1 is more clearly visible in

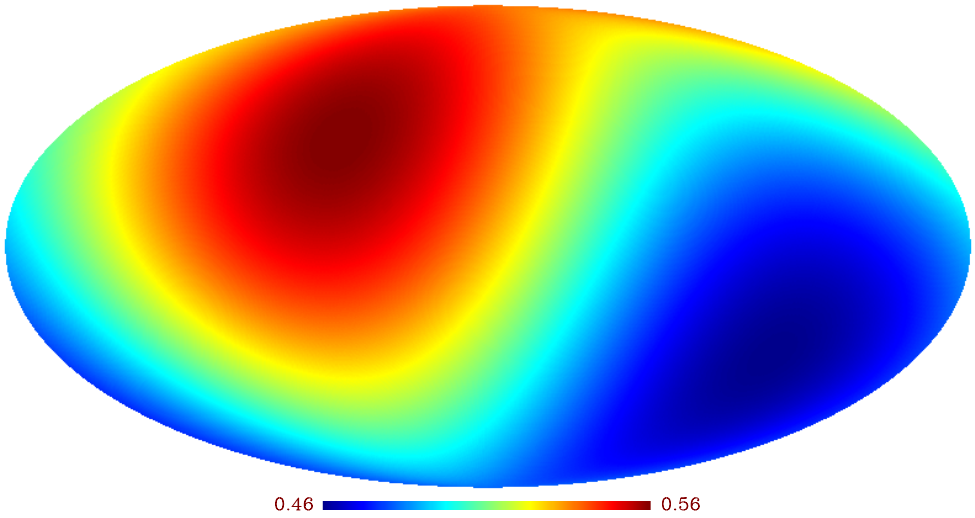

Figure B.1: We first apply this dipole-detecting formalism to a map with a pure dipole of amplitude 0.1, in the direction $(l, b) = (61.38°, 33.37°)$ (a randomly chosen direction). The pure-dipole map is shown here.

Fig. B.2, which shows that as we excise more and more of the Galactic plane, the results behave appropriately: the results are all consistent with the correct value of dipole amplitude $A = 0.1$ within measurement error bars, which themselves grow larger as a function of how much of the sky is cut.

Table B.1: Comparison of dipole parameters with different cuts in Galactic latitude, for a pure dipole of amplitude 0.1, in the direction $(l, b) = (61.38°, 33.37°)$.

$\|b\| \geq$	Systematics	NSIDE	N	$A_{\rm peak}$	l	b	68 percent CI	95 percent CI
0.0	none	128	100000	0.1000	61.4	33.4	0.095 - 0.105	0.089 - 0.11
0.0	Haslam	128	100000	0.100	61.4	33.4	0.094 - 0.105	0.089 - 0.111
10.0	Haslam	128	82031	0.099	61.4	33.4	0.093 - 0.106	0.086 - 0.113
20.0	Haslam	128	65364	0.099	61.4	33.3	0.09 - 0.107	0.083 - 0.116
30.0	Haslam	128	49218	0.098	61.4	33.4	0.088 - 0.109	0.078 - 0.12
45.0	Haslam	128	28568	0.095	61.4	33.4	0.079 - 0.112	0.065 - 0.129
60.0	Haslam	128	13183	0.081	61.5	33.4	0.059 - 0.112	0.045 - 0.148

We also perform tests to make sure that asymmetric sky cuts do not cause unexpected problems, and that explicit marginalization over the quadrupole and octopole is not necessary. In Table B.2, we present sample results from such tests. The results

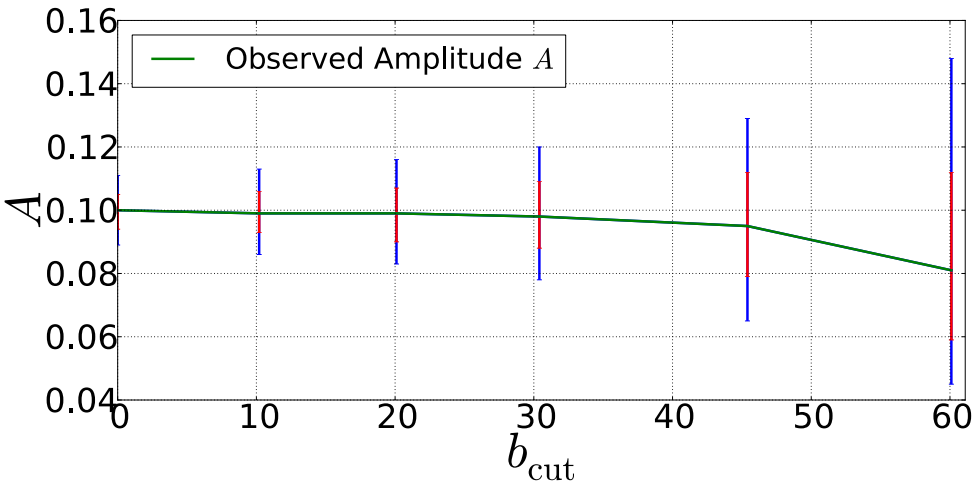

Figure B.2: Dipole amplitude as a function of how much of the Galactic plane is cut. The Haslam systematics template is taken into account. The map being tested has a pure dipole of amplitude 0.1, in the direction $(l, b) = (61.38°, 33.37°)$. Note that all results are consistent with the correct dipole amplitude, and that the error bars grow with increasingly aggressive sky cuts.

hold constant the fairly aggressive sky cut of Galactic $|b| < 30°$ and declination $< 37°$ and $> 78°$ (in imitation of NVSS-related sky cuts), and apply the Haslam systematic template as well as a quadrupole (a_{21}) and octopole (a_{30}) template. Adding the quadrupole and octopole templates changes the results by the order of 1-2 percent, which is reassuring since (a) the results should change slightly, given that the sky cut should couple modes at least somewhat, and (b) the results change so little that the effect is essentially negligible. We have also performed several other tests to make sure that higher multipoles do not contribute appreciably.

Table B.2: Comparison of dipole parameters with different systematics templates, given a sky cut excluding $|b| < 30°$ and declinations less than -37.0 degrees or greater than 78 degrees (as in our NVSS results), for a pure dipole of amplitude 0.1, in the direction $(l, b) = (61.38°, 33.37°)$.

$\|b\| \geq$	Systematics	NSIDE	N	$A_{\rm peak}$	l	b	68 percent CI	95 percent CI
30.0	none	128	41306	0.097	61.4	33.4	0.087 - 0.107	0.078 - 0.118
30.0	Haslam	128	41306	0.097	61.4	33.4	0.085 - 0.109	0.073 - 0.12
30.0	Haslam+$a_{21} + a_{30}$	128	41306	0.096	61.4	33.3	0.083 - 0.11	0.069 - 0.123

APPENDIX C

Coordinate-System Rotations in HEALPix

C.1 Rotating Coordinate Systems

This appendix serves as a very brief note regarding a certain artifact introduced by rotating pixels between equatorial and Galactic coordinates in HEALPix. The upper two plots in Fig. C.1 show the azimuthal coordinate l (left) and the coordinate b (right) of each pixel center in HEALPix, with resolution parameter NSIDE=128. Using either the HEALPix rotation routine `rotate_coord` or the IDL Astronomy Library routine `glactc`, it is straightforward to convert between equatorial and Galactic coordinates. In the figure, we display (in Galactic coordinates) the results of rotating from equatorial to Galactic coordinates: declination (left) and right ascension (right) of each HEALPix pixel center, in Galactic coordinates, are shown. The pixelization artifacts are not introduced by either rotation routine, but are rather a problem associated with trying to do a one-to-one match of pixel centers in different coordinate systems, regardless of the rotation routine used. The routines both successfully rotate a given set of *unpixelized* equatorial coordinates to their corresponding *unpixelized* Galactic coordinates, but when pixel centers are being rotated, it occasionally happens (and the pattern is a regular one, as can be seen clearly in the figure) that two pixel centers in equatorial coordinates map into a single pixel

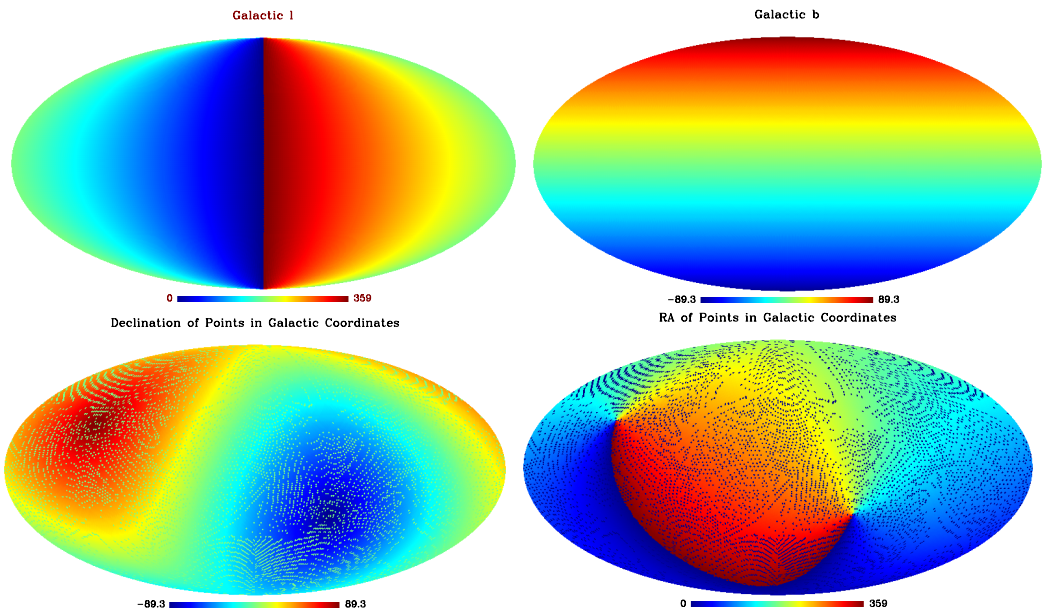

Figure C.1: Plotted are, respectively, the Galactic l, the Galactic b, the dec, and the ra of each point in Galactic coordinates. The "holes" in the bottom two plots, where pixels are incorrectly set equal to zero, represent pixels where the rotation from equatorial coordinates to Galactic coordinates fails to map anything into certain Galactic pixel centers.

in Galactic coordinates, or that nothing maps into a given pixel in Galactic coordinates. One must therefore rotate a set of equatorial coordinates (say, of galaxies on the sky) to Galactic coordinates before pixelizing in Galactic coordinates rather than pixelizing in equatorial coordinates and then rotating from equatorial to Galactic. In brief: rotate then pixelize; do not pixelize then rotate.

Bibliography

Abate, A. and Feldman, H. Detected fluctuations in sloan digital sky survey luminous red galaxy magnitudes: bulk flow signature or systematic? *Monthly Notices of the Royal Astronomical Society*, 2012.

Ando, S., Komatsu, E., Narumoto, T. and Totani, T. Angular power spectrum of gamma-ray sources for glast: blazars and clusters of galaxies. *Monthly Notices of the Royal Astronomical Society*, 376(4):1635–1647, 2007.

Aurich, R. and Lustig, S. Can one reconstruct masked CMB sky? *arXiv:1005.5069*, 2010.

Baleisis, A., Lahav, O., Loan, A. and Wall, J. Searching for large-scale structure in deep radio surveys. *Monthly Notices of the Royal Astronomical Society*, 297(2):545–558, 1998.

Bennett, C. L., Halpern, M., Hinshaw, G., Jarosik, N., Kogut, A., Limon, M., Meyer, S. S., Page, L., Spergel, D. N., Tucker, G. S., Wollack, E., Wright, E. L., Barnes, C., Greason, M. R., Hill, R. S., Komatsu, E., Nolta, M. R., Odegard, N., Peiris, H. V., Verde, L. and Weiland, J. L. First Year Wilkinson Microwave Anisotropy Probe (WMAP) Observations: Preliminary Maps and Basic Results. *ApJS*, 148:1–27, 2003.

Bennett, C. L. et al. Seven-Year Wilkinson Microwave Anisotropy Probe (WMAP) Observations: Are There Cosmic Microwave Background Anomalies? *Astrophys. J. Suppl.*, 192:17, 2011.

Bilicki, M., Chodorowski, M., Jarrett, T. and Mamon, G. Is the two micron all sky survey clustering dipole convergent? *The Astrophysical Journal*, 741:31, 2011.

Blake, C., Ferreira, P. and Borrill, J. The angular power spectrum of nvss radio galaxies. *Monthly Notices of the Royal Astronomical Society*, 351(3):923–934, 2004.

Blake, C. and Wall, J. Detection of the velocity dipole in the radio galaxies of the nrao vla sky survey. *Arxiv preprint astro-ph/0203385*, 2002.

Boughn, S., Crittenden, R. and Koehrsen, G. The large-scale structure of the x-ray background and its cosmological implications. *The Astrophysical Journal*, 580:672, 2002.

Briggs, M., Paciesas, W., Pendleton, G., Meegan, C., Fishman, G., Horack, J., Brock, M., Kouveliotou, C., Hartmann, D. and Hakkila, J. Batse observations of the large-scale isotropy of gamma-ray bursts. *Arxiv preprint astro-ph/9509078*, 1995.

Burles, S. and Rappaport, S. Detecting the aberration of the cosmic microwave background. *The Astrophysical Journal Letters*, 641:L1, 2006.

Cardelli, J., Clayton, G. and Mathis, J. The relationship between infrared, optical, and ultraviolet extinction. *The Astrophysical Journal*, 345:245–256, 1989.

Chu, M., Eriksen, H., Knox, L., Górski, K., Jewell, J., Larson, D., ODwyer, I. and Wandelt, B. Cosmological parameter constraints as derived from the wilkinson microwave anisotropy probe data via gibbs sampling and the blackwell-rao estimator. *Physical Review D*, 71(10):103002, 2005.

Compton, A. and Getting, I. An apparent effect of galactic rotation on the intensity of cosmic rays. *Physical Review*, 47(11):817, 1935.

Condon, J., Cotton, W., Greisen, E., Yin, Q., Perley, R., Taylor, G. and Broderick, J. The nrao vla sky survey. *The Astronomical Journal*, 115:1693, 1998.

Copi, C. J., Huterer, D., Schwarz, D. J. and Starkman, G. D. Uncorrelated universe: Statistical anisotropy and the vanishing angular correlation function in WMAP years 1-3. *Phys. Rev. D*, 75(2):023507, 2007.

Copi, C. J., Huterer, D., Schwarz, D. J. and Starkman, G. D. No large-angle correlations on the non-Galactic microwave sky. *MNRAS*, 399:295–303, 2009.

Courteau, S. and van den Bergh, S. The solar motion relative to the local group. *The Astronomical Journal*, 118:337, 1999.

Crawford, F. Detecting the cosmic dipole anisotropy in large-scale radio surveys. *The Astrophysical Journal*, 692:887, 2009.

Dunlop, J. and Peacock, J. The redshift cut-off in the luminosity function of radio galaxies and quasars. *Monthly Notices of the Royal Astronomical Society*, 247:19, 1990.

Efstathiou, G., Ma, Y. and Hanson, D. Large-angle correlations in the cosmic microwave background. *MNRAS*, 407:2530–2542, 2010.

Erdogdu, P., Huchra, J., Lahav, O., Colless, M., Cutri, R., Falco, E., George, T., Jarrett, T., Jones, D., Kochanek, C. et al. The dipole anisotropy of the 2mass redshift survey. *Arxiv preprint astro-ph/0605343*, 2006.

Erickcek, A., Carroll, S. and Kamionkowski, M. Superhorizon perturbations and the cosmic microwave background. *Physical Review D*, 78(8):083012, 2008a.

Erickcek, A. L., Hirata, C. M. and Kamionkowski, M. A Scale-Dependent Power Asymmetry from Isocurvature Perturbations. *Phys. Rev.*, D80:083507, 2009.

Erickcek, A. L., Kamionkowski, M. and Carroll, S. M. A Hemispherical Power Asymmetry from Inflation. *Phys. Rev.*, D78:123520, 2008b.

Frith, W., Outram, P. and Shanks, T. The 2-micron all-sky survey galaxy angular power spectrum: probing the galaxy distribution to gigaparsec scales. *Monthly Notices of the Royal Astronomical Society*, 364(2):593–600, 2005a.

Frith, W., Shanks, T. and Outram, P. 2mass constraints on the local large-scale structure: a challenge to λcdm? *Monthly Notices of the Royal Astronomical Society*, 361(2):701–709, 2005b.

Fruchter, A., Thorsett, S., Metzger, M., Sahu, K., Petro, L., Livio, M., Ferguson, H., Pian, E., Hogg, D., Galama, T. et al. Hubble space telescope and palomar imaging of grb 990123: implications for the nature of gamma-ray bursts and their hosts. *The Astrophysical Journal Letters*, 519:L13, 1999.

Gibelyou, C., Huterer, D. and Fang, W. Detectability of large-scale power suppression in the galaxy distribution. *Phys. Rev.*, D82:123009, 2010.

Gordon, C., Hu, W., Huterer, D. and Crawford, T. M. Spontaneous Isotropy Breaking: A Mechanism for CMB Multipole Alignments. *Phys. Rev.*, D72:103002, 2005.

Górski, K., Hivon, E., Banday, A., Wandelt, B., Hansen, F., Reinecke, M. and Bartelmann, M. Healpix: A framework for high-resolution discretization and fast analysis of data distributed on the sphere. *The Astrophysical Journal*, 622:759, 2005.

Grishchuk, L. and Zeldovich, I. Long-wavelength perturbations of a friedmann universe, and anisotropy of the microwave background radiation. *Soviet Astronomy*, 22:125–129, 1978.

Gunn, J. Deviations from pure hubble flow-a review. In *The Extragalactic Distance Scale*, volume 4, pages 344–359. 1988.

Hanson, D. and Lewis, A. Estimators for cmb statistical anisotropy. *Physical Review D*, 80(6):063004, 2009.

Haslam, C., Klein, U., Salter, C., Stoffel, H., Wilson, W., Cleary, M., Cooke, D. and Thomasson, P. A 408 mhz all-sky continuum survey. i-observations at southern declinations and for the north polar region. *Astronomy and Astrophysics*, 100:209–219, 1981.

Haslam, C., Salter, C., Stoffel, H. and Wilson, W. A 408 mhz all-sky continuum survey. ii-the atlas of contour maps. *Astronomy and Astrophysics Supplement Series*, 47:1, 1982.

Hearin, A. P., Gibelyou, C. and Zentner, A. R. Testing the origin of the CMB large-angle correlation deficit with a galaxy imaging survey. *Journal of Cosmology and Astroparticle Physics*, 10(012), 2011.

Hirata, C. M. Constraints on cosmic hemispherical power anomalies from quasars. *JCAP*, 0909:011, 2009.

Ho, S., Hirata, C., Padmanabhan, N., Seljak, U. and Bahcall, N. Correlation of cmb with large-scale structure. i. integrated sachs-wolfe tomography and cosmological implications. *Physical Review D*, 78(4):043519, 2008.

Hoftuft, J. et al. Increasing evidence for hemispherical power asymmetry in the five-year WMAP data. *Astrophys. J.*, 699:985–989, 2009.

Hu, W. and Jain, B. Joint galaxy-lensing observables and the dark energy. *Physical Review D*, 70(4):043009, 2004.

Huchra, J., Macri, L., Masters, K., Jarrett, T., Berlind, P., Calkins, M., Crook, A.,

Cutri, R., Erdogdu, P., Falco, E. et al. The 2mass redshift survey-description and data release. *Arxiv preprint arXiv:1108.0669*, 2011.

Itoh, Y., Yahata, K. and Takada, M. Dipole anisotropy of galaxy distribution: Does the cmb rest frame exist in the local universe? *Physical Review D*, 82(4):043530, 2010.

Iwan, D., Shafer, R., Marshall, F., Boldt, E., Mushotzky, R. and Stottlemyer, A. A large scale height galactic component of the diffuse 2-60 kev background. *The Astrophysical Journal*, 260:111–123, 1982.

Jarrett, T., Chester, T., Cutri, R., Schneider, S. and Huchra, J. The 2mass large galaxy atlas. *The Astronomical Journal*, 125:525, 2003.

Jarrett, T., Chester, T., Cutri, R., Schneider, S., Rosenberg, J., Huchra, J. and Mader, J. 2mass extended sources in the zone of avoidance. *The Astronomical Journal*, 120:298, 2000a.

Jarrett, T., Chester, T., Cutri, R., Schneider, S., Skrutskie, M. and Huchra, J. 2mass extended source catalog: overview and algorithms. *The Astronomical Journal*, 119:2498, 2000b.

Kashlinsky, A., Atrio-Barandela, F., Kocevski, D. and Ebeling, H. A measurement of large-scale peculiar velocities of clusters of galaxies: results and cosmological implications. *The Astrophysical Journal Letters*, 686:L49, 2008.

Keisler, R. The statistical significance of the. *The Astrophysical Journal Letters*, 707:L42, 2009.

Kogut, A., Lineweaver, C., Smoot, G., Bennett, C., Banday, A., Boggess, N., Cheng, E., De Amici, G., Fixsen, D., Hinshaw, G. et al. Dipole anisotropy in the cobe

differential microwave radiometers first-year sky maps. *The Astrophysical Journal*, 419:1, 1993.

Kommers, J., Lewin, W., Kouveliotou, C., van Paradijs, J., Pendleton, G., Meegan, C. and Fishman, G. A search for nontriggered gamma-ray bursts in the batse database. *The Astrophysical Journal*, 491:704, 1997.

Lahav, O., Lilje, P., Primack, J. and Rees, M. Dynamical effects of the cosmological constant. *Monthly Notices of the Royal Astronomical Society*, 251:128–136, 1991.

Lahav, O., Santiago, B., Webster, A., Strauss, M., Davis, M., Dressler, A. and Huchra, J. The supergalactic plane revisited with the optical redshift survey. *Monthly Notices of the Royal Astronomical Society*, 312(1):166–176, 2000.

Maller, A., McIntosh, D., Katz, N. and Weinberg, M. The clustering dipole of the local universe from the two micron all sky survey. *The Astrophysical Journal Letters*, 598:L1, 2003.

Maller, A., McIntosh, D., Katz, N. and Weinberg, M. The galaxy angular correlation functions and power spectrum from the two micron all sky survey. *The Astrophysical Journal*, 619:147, 2005.

Maoz, E. Indications for gamma-ray bursts originating within an extended galactic halo? *Arxiv preprint astro-ph/9304015*, 1993.

Maoz, E. The expected dipole in the distribution of cosmological gamma-ray bursts. *The Astrophysical Journal*, 428:454–457, 1994.

Metzger, M., Djorgovski, S., Kulkarni, S., Steidel, C., Adelberger, K., Frail, D., Costa, E. and Frontera, F. Spectral constraints on the redshift of the optical counterpart to the γ-ray burst of 8 may 1997. *Nature*, 387(6636):878–880, 1997.

Paciesas, W., Meegan, C., Pendleton, G., Briggs, M., Kouveliotou, C., Koshut, T., Lestrade, J., McCollough, M., Brainerd, J., Hakkila, J. et al. The fourth batse gamma-ray burst catalog (revised). *The Astrophysical Journal Supplement Series*, 122:465, 1999.

Plionis, M. and Georgantopoulos, I. The rosat x-ray background dipole. *Monthly Notices of the Royal Astronomical Society*, 306(1):112–116, 1999.

Pontzen, A. and Peiris, H. V. The cut-sky cosmic microwave background is not anomalous. *Phys. Rev.*, D81:103008, 2010.

Rowan-Robinson, M., Sharpe, J., Oliver, S., Keeble, O., Canavezes, A., Saunders, W., Taylor, A., Valentine, H., Frenk, C., Efstathiou, G. et al. The iras pscz dipole. *Monthly Notices of the Royal Astronomical Society*, 314(2):375–397, 2000.

Sarkar, D., Huterer, D., Copi, C. J., Starkman, G. D. and Schwarz, D. J. Missing Power vs low-l Alignments in the Cosmic Microwave Background: No Correlation in the Standard Cosmological Model. *Astropart. Phys.*, 34:591–594, 2011.

Scharf, C., Jahoda, K. and Boldt, E. On the measurement of a cosmological dipole in the photon number counts of gamma-ray bursts. *Arxiv preprint astro-ph/9506008*, 1995.

Scharf, C., Jahoda, K., Treyer, M., Lahav, O., Boldt, E. and Piran, T. The 2-10 kev x-ray background dipole and its cosmological implications. *The Astrophysical Journal*, 544:49, 2000.

Schlafly, E. and Finkbeiner, D. Measuring reddening with sdss stellar spectra and recalibrating sfd. *Arxiv preprint arXiv:1012.4804*, 2010.

Schlegel, D., Finkbeiner, D. and Davis, M. Maps of dust infrared emission for use in estimation of reddening and cosmic microwave background radiation foregrounds. *The Astrophysical Journal*, 500:525, 1998.

Singal, A. K. Large peculiar motion of the solar system from the dipole anisotropy in sky brightness due to distant radio sources. 2011.

Skrutskie, M., Cutri, R., Stiening, R., Weinberg, M., Schneider, S., Carpenter, J., Beichman, C., Capps, R., Chester, T., Elias, J. et al. The two micron all sky survey (2mass). *The Astronomical Journal*, 131:1163, 2006.

Smith, K. and Huterer, D. No evidence for the cold spot in the nvss radio survey. *Monthly Notices of the Royal Astronomical Society*, 403(1):2–8, 2010.

Tegmark, M., Hartmann, D., Briggs, M. and Meegan, C. The angular power spectrum of batse 3b gamma-ray burst. *Arxiv preprint astro-ph/9510129*, 1995.

Treyer, M., Scharf, C., Lahav, O., Jahoda, K., Boldt, E. and Piran, T. Large-scale fluctuations in the x-ray background. *The Astrophysical Journal*, 509:531, 1998.

Turner, M. Tilted universe and other remnants of the preinflationary universe. *Physical Review D*, 44(12):3737, 1991.

van Paradijs, J., Pettini, M., Tanvir, N., Bloom, J., Pedersen, H., Noerdgaard-Nielsen, H., Linden-Voernle, M., Melnick, J., van de Steene, G., Bremer, M. et al. Discovery of transient optical emission from the error box of the gamma-ray burst of february 28, 1997. *Nature*, 386:686–689, 1997.

Webster, A. The clustering of radio sources. i-the theory of power-spectrum analysis. ii-the 4c, gb and mc1 surveys. *Monthly Notices of the Royal Astronomical Society*, 175:61–83, 1976.

Wright, E., Eisenhardt, P., Mainzer, A., Ressler, M., Cutri, R., Jarrett, T., Kirkpatrick, J., Padgett, D., McMillan, R., Skrutskie, M. et al. The wide-field infrared survey explorer (wise): mission description and initial on-orbit performance. *The Astronomical Journal*, 140:1868, 2010.

Xiao, L. and Schaefer, B. Estimating redshifts for long gamma-ray bursts. *The Astrophysical Journal*, 707:387, 2009.